THE EFFECTS OF COMPOSITION AND MICROSTRUCTURE ON THE REACTION BEHAVIOR OF MCrAlY ALLOYS UNDER A VARIETY OF AGGRESSIVE ENVIRONMENTAL CONDITIONS

by

Michael Nathan Task

BS, University of Pittsburgh, 2007

Submitted to the Graduate Faculty of

The Swanson School of Engineering in partial fulfillment

of the requirements for the degree of

Master of Science

University of Pittsburgh

2009

UNIVERSITY OF PITTSBURGH

SWANSON SCHOOL OF ENGINEERING

This thesis was presented

by

Michael Nathan Task

It was defended on

November 19, 2009

and approved by

I. Nettleship, Associate Professor, Mechanical Engineering and Materials Science Department

J. C. Yang, Professor, Mechanical Engineering and Materials Science Department

Thesis Co-Advisor: F. S. Pettit, Professor Emeritus, Mechanical Engineering and Materials Science Department

Thesis Co-Advisor: B. Gleeson, Professor, Mechanical Engineering and Materials Science Department

Thesis Co-Advisor: G. H. Meier, Professor, Mechanical Engineering and Materials Science Department

THE EFFECTS OF COMPOSITION AND MICROSTRUCTURE ON THE REACTION BEHAVIOR OF MCrAlY ALLOYS UNDER A VARIETY OF AGGRESSIVE ENVIRONMENTAL CONDITIONS

Michael Nathan Task, MS

University of Pittsburgh, 2009

Cast alloys with compositions similar to those of MCrAlY overlay coatings, which are commonly deposited on Ni-base superalloys in the hot section of gas turbine engines, were exposed to a variety of aggressive conditions. The materials studied include (in wt%): Ni-31Cr-11.25Al-0.65Y, Co-23Cr-13Al-0.65Y, Ni-20Co-18Cr-12.5Al-0.6Y-0.4Hf-0.25Si, Ni-10Co-18Cr-12.5Al-0.6Y-0.4Hf-0.25Si, and Ni-10Co-27.1Cr-12.5Al-0.6Y-0.4Hf-0.25Si . The microstructures of the Ni-base alloys contained FCC γ-Ni (or γ′-Ni_3Al, depending on temperature and composition), primitive cubic β-NiAl , and a Ni-rich yttride. BCC α-Cr was also present in some cases. The CoCrAlY contained HCP α-Co, β-CoAl, and a Co-rich yttride. The experimental conditions were: Type I and Type II hot corrosion, cyclic oxidation, and intermittent hot corrosion. The effects of alloy composition and microstructure on the resistance to these modes of degradation were determined using scanning electron microscopy and kinetic data.

All alloys showed good resistance to Type I hot corrosion. Conversely, Type II hot corrosion was catastrophic in most cases; however, the coarse-grained NiCrAlY alloy demonstrated reasonably good resistance to Type II attack. When the microstructure was refined via injection casting, however, this alloy showed substantial degradation under Type II conditions. This was attributed partially to differences in the morphology and distribution of the α-Cr phase. The Type II hot corrosion resistance of a NiCoCrAlY alloy was improved by lowering the cobalt content and increasing the chromium content such that a coarse distribution of α-Cr was present in the microstructure.

All alloys formed protective Al_2O_3 scales during cyclic oxidation at 1100°C, with the exception of the NiCrAlY, which showed scale spallation after short exposures. The oxidation resistance of this alloy improved with decreasing temperature. This behavior was explained in part by a phase transformation which results in a volume contraction upon cooling and thus a

compressive stress in the oxide. This transformation, as well as other aspects of the phase equilibria in this NiCrAlY system, was examined experimentally, and the results were compared with thermodynamic predictions.

No difference in oxidation behavior was observed when cyclic oxidation of the MCrAlY alloys was preceded by a Type I hot corrosion exposure. Conversely, the cyclic oxidation resistance of uncoated René N5 was substantially reduced by such an initial exposure.

TABLE OF CONTENTS

LIST OF TABLES

LIST OF FIGURES

ACKNOWLEDGEMENTS

I would like to express my sincere gratitude to my research advisers, Professors Gerald H. Meier, Frederick S. Pettit, and Brian Gleeson, not only for the knowledge that they have imparted to me, but also for the truly pleasant work environment that they have created for myself and my colleagues. I also owe a debt of gratitude to these colleagues, namely Wes Jackson, Ed Magee, Michael Helminiak, Meltem Yanar, Nan Mu, Keeyoung Jung, and Wei Zhao, all of whom are exceedingly kind and helpful, inside of the laboratory and out. Additionally, my committee members, Professors Ian Nettleship and Judith Yang, have taught me a great deal in the classroom, and I am honored that they are willing to once again share with me their expertise.

Professor Zi-Kui Liu and his graduate student, DongEung Kim, were kind enough to perform the CALPHAD work which will be presented, and their efforts are much appreciated.

On a personal note, thanks are certainly due to my mother, Karen, for all that she has done for me over the years. Even an abbreviated list of all of the selfless things that she has done on my behalf would constitute a thesis in itself. Also, I would like to thank my brother, Keith, for all of his support and advice. Some may say that his occasional derision is a bit harsh, but that is, after all, what brothers are for, and I know that his heart is constantly in the right place. In addition Mark, my uncle, has always supported me in all that I have done, and has never hesitated to help me in any way possible.

Lastly, I am forever grateful to my girlfriend Jessica for her endless praise, her words of encouragement, and her smile which never fails to warm my heart and brighten my day. I know there are often times when it may seem as though my work is more important to me than spending time with her; it is my sincere hope that she realizes that this could never be the case.

This work was funded by the Office of Naval Research, under contract number N00014-07-1-0455.

1.0 INTRODUCTION

Materials used in industrial, marine, and aero gas turbine engines must be able to withstand a host of harsh conditions, including large cyclic stresses in the presence of a high-temperature oxidizing environment. The strength requirements are typically met by Ni-base superalloys, which form the structural base of turbine vanes and blades. At relatively low temperatures, these materials may also have sufficient oxidation-resistance and therefore require no further protection. Often, however, an aluminum-rich coating is applied to the surface of the superalloy in order to impart oxidation-resistance, which is achieved by the formation of a thermally-grown α-Al_2O_3 surface scale. A number of materials have been studied extensively and put into practice for this purpose, including MCrAlY (M= Ni and/or Co) overlay coatings and (Ni,Pt)Al diffusion coatings. For operation at the most extreme-temperatures, ceramic thermal barrier coatings (TBCs) are applied on the surface of the above-mentioned bond coatings in order to lower the temperature to which these metallic components are exposed.

A further complication commonly arises during the operation of gas turbines which involves the formation of fused salt deposits on the surface of the turbine hardware. The principal salt which tends to deposit is Na_2SO_4. It is commonly believed that this salt forms as a result of sulfur impurities in the fuel oxidizing and reacting at high temperatures with NaCl which has been ingested via the intake air or fuel contamination, although other mechanisms are also conceivable [1]. This is a considerable problem when engines operate in coastal regions where NaCl may be a significant source of contamination, particularly in marine and industrial applications where low-grade fuel oils with high S-contents are routinely burned. These salt deposits can result in highly accelerated oxidation at elevated temperatures. This severe and sometimes catastrophic degradation process has been termed “hot corrosion”.

Much effort has been put forth to study hot corrosion from a mechanistic standpoint; however, no overlay or diffusion coating has been developed which provides acceptable

resistance to all types of hot corrosion attack (these different types of hot corrosion are discussed in greater detail in section 2.2). Thus, one goal of the current research is to develop an overlay coating composition of the MCrAlY type which provides superior resistance to degradation under a variety of environmental conditions. These conditions include cyclic oxidation, Type I (high-temperature) hot corrosion, intermittent hot corrosion (cyclic oxidation with brief, intermittent periods of Type I hot corrosion), and Type II (low-temperature) hot corrosion.

In addition, little is currently known about the effect of microstructure on the hot corrosion resistance of Al_2O_3-forming materials. Therefore, the second goal of this work is to study the influence of phase constitution on the hot corrosion resistance of MCrAlY alloys. A fundamental understanding of the correlation between phase constitution and hot corrosion resistance will greatly facilitate the development of new coating materials with enhanced resistance to this type of degradation.

2.0 BACKGROUND

2.1 FORMATION OF SALT DEPOSITS ON GAS TURBINE HARDWARE

In gas turbine engines, particularly those used in coastal regions or for marine propulsion, Na_2SO_4-rich salt deposits commonly develop on turbine vanes and blades; these salts are very commonly rich in Na_2SO_4. When the environment is such that these salts are molten, conditions can develop for severe hot corrosion. In order to understand and combat hot corrosion in these systems, an appreciation of the origin of these corrosive salts is necessary.

The approximate composition of sea salt can be found in Table 1 [1] .

Table 1. Approximate sea salt composition

Ion	Concentration (wt%)	Concentration (mole%)
Na^+	30.3	42.04
K^+	0.52	0.35
Mg^+	3.69	4.85
Ca^{2+}	1.26	1.02
Cl^-	54.78	49.25
SO_4^{2-}	7.44	2.49

It is generally believed that the Na_2SO_4 found in the hot sections of a gas turbine can either be directly deposited due to impact of ingested sea salt particles, or condensed from the vapor phase [2]. In order for vapor phase condensation to occur, sulfur, which is commonly present as a fuel impurity, must be oxidized to SO_2 and/or SO_3 in the combustor section of the engine. These species and oxygen then react with oxygen and gaseous NaCl, which has been introduced via sea

salt impurities in either the intake air or the fuel. If the surface temperature of the turbine hardware is below the dew point of Na_2SO_4, which is determined by the concentration of ingested salt and the level of sulfur in the fuel, then a condensed sulfate deposit will be formed.

DeCrescente and Bornstein [3] studied this process using basic thermodynamic considerations, assuming 1 ppm NaCl(v) and 0.4 wt% sulfur in the fuel. The following two reactions were considered:

$$2NaCl + SO_2 + \frac{1}{2}O_2 + H_2O \rightarrow Na_2SO_4 + 2HCl \quad (1)$$

$$2NaCl + SO_3 + H_2O \rightarrow Na_2SO_4 + 2HCl \quad (2)$$

All species in Equations (1) and (2) are present in the vapor phase . It was found that the reaction between NaCl and SO_2, Equation (1), proceeded to 75% completion at 1000°C and 1 atm total pressure. Consideration of Le Chatelier's Principle reveals that an increase in total pressure would result in an increase in the degree of NaCl → Na_2SO_4 conversion. The investigators therefore concluded that the high pressure ratios present in a gas turbine engine should cause complete conversion to gaseous sulfate.

The gaseous phases present after combustion in a gas turbine engine were further studied by Hanby and Beer [4] who suggested that at significantly high temperatures, NaCl vapor may be converted to Na_2SO_4 with NaOH as an intermediate species according to the following series of reactions:

$$NaCl + H_2O \rightarrow NaOH + HCl \quad (3)$$

$$2NaOH + SO_2 + \frac{1}{2}O_2 \rightarrow Na_2SO_4 + H_2O \quad (4)$$

In addition, these investigators determined, using a controlled mixing history combustor, that the degree of gas phase sulfation of NaCl to Na_2SO_4 changes very little with sulfur concentration in the fuel (from 0.1 – 1 wt%) and NaCl concentration in the intake air (from 10 – 50 ppm). Noteworthy temperature dependence does exist, with the degree of sulfation increasing as the gas temperature is increased from 1190°C to 1350°C.

As mentioned above, direct impact of ingested sea salt particles with turbine hardware can also result in the formation of a Na_2SO_4 deposit. Bornstein and Allen [1] investigated the exact mechanism of salt deposition on turbine airfoils. Salts deposited on the compressor as well as the inner and outer surfaces of internally cooled vanes and blades from an industrial turbine were evaluated using Inductively Coupled Plasma, ion chromatography, and Electron Probe

Micro Analysis. Two key observations were made. Firstly, the salts taken from the first three turbine stages were equivalent in both amount and composition. In addition, the compositions of the salts sampled from the internal and external surfaces of the first and second stage airfoils were comparable. The surface temperature of the turbine hardware would be expected to decrease in the latter stages of the engine. Also, the temperature of the internal surfaces would clearly be lower than the external surfaces. If gas-phase condensation were the dominant salt deposition mechanism, these temperature differences would result in differences in the amount and composition of salt deposited in various regions. Such differences were not observed, and therefore it was concluded that impact deposition of salt particles on turbine airfoils is likely the central mechanism.

The results of earlier work by McCreath [2] support this conclusion under certain conditions. This research demonstrated that at a constant engine load, nearly 96 wt. % of the salt ingested into a naval gas turbine engine through the air intake was filtered out in the compressor section. During acceleration from idle conditions to full power, considerable salt shedding from the compressor was observed. Thus, sulfate deposits found downstream from the compressor can conceivably be the result of salt shedding from the compressor, but this was found to be significant only during transient engine conditions.

2.2 Na_2SO_4 – INDUCED HOT CORROSION

Regardless of the manner in which the Na_2SO_4 is deposited, it can be highly corrosive if present as a molten film. If the temperature of the environment is above the melting point of Na_2SO_4 (T_m=884°C [5]), the resulting degradation is typically termed Type I, or high temperature hot corrosion. As discussed in Section 2.2.3, a corrosive Na_2SO_4-based molten salt can also form below 884°C as a result of a chemical interaction with the combustion gas. This highly accelerated, self-sustaining form of corrosion has been termed Type II, or low temperature hot corrosion. These two forms of hot corrosion are quite distinct mechanistically and occur under significantly different environmental conditions. Together they constitute the primary modes of degradation considered in this study; therefore a comprehensive review of the available hot corrosion literature is presented below.

2.2.1 The Stages of Hot Corrosion

Hot corrosion can be considered to occur in two distinct stages, initiation and propagation [6]. These two stages can be seen in Figure 1, in which the weight change per unit area for a Ni-8Cr-6Al alloy exposed to Type I hot corrosion conditions is plotted as a function time. The specimen was coated with 2-3 mg cm^{-2} Na_2SO_4 every 20 hours and exposed at 900°C.

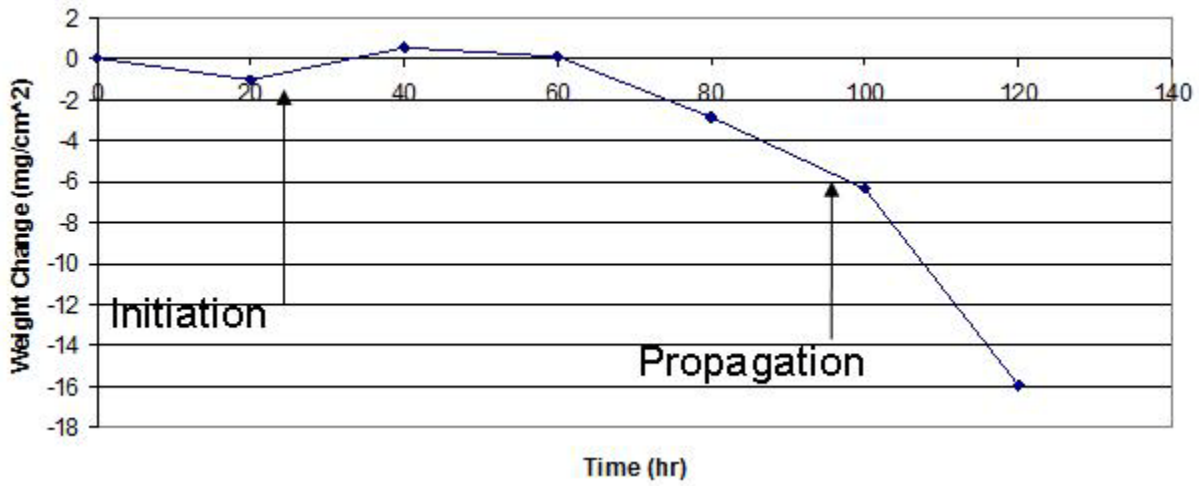

Figure 1. Weight change vs. time: Ni-8Cr-6Al, Type I hot corrosion

In Figure 1, the existence of two distinct stages is demonstrated. During the initiation stage, i.e. up to approximately 60 hours of exposure, weight changes are relatively small and no catastrophic degradation occurs. During the propagation stage, beginning at roughly 60 hours, severe degradation commences and large weight losses are observed as a result of rapid oxidation and scale spallation. It is important to note that Figure 1 shows the behavior of an alloy which is known to be quite susceptible to this type of hot corrosion; thus, the initiation stage is relatively short. The duration of the initiation stage can vary considerably for different alloys exposed under the same conditions. For example, CoCrAlY alloys can typically be exposed for

well over 1000 hours under the above conditions before the propagation stage commences. In fact, it has been established that the length of the initiation stage is highly dependent on a number of variables related to alloy composition and exposure conditions.

2.2.1.1 Initiation Stage

During the initiation stage of the hot corrosion of metals and alloys, the chemical processes which take place are quite similar to those that occur during simple oxidation. Specifically, metallic elements are oxidized and some other species, typically oxygen, is reduced to form an external scale [6]. The important difference between this process and simple oxidation is that during hot corrosion, the reducible species originates from the salt deposit. This alloy-salt interaction can ultimately result in the local development of extremely corrosive conditions due to a gradual shift to highly basic or acidic salt compositions. In time, the deposit becomes sufficiently corrosive to cause the breakdown of the protective scale, and the propagation stage commences.

In Figure 2, a schematic phase stability diagram for the Na-S-O system is shown. The large dot in the Na_2SO_4 phase field indicates the composition of the initially-deposited salt, as defined by the parameters p_{O_2} and $-\log a_{Na_2O}$ (see section 2.2.1.2 for a more thorough explanation of these compositional parameters and phase stability diagrams in general)

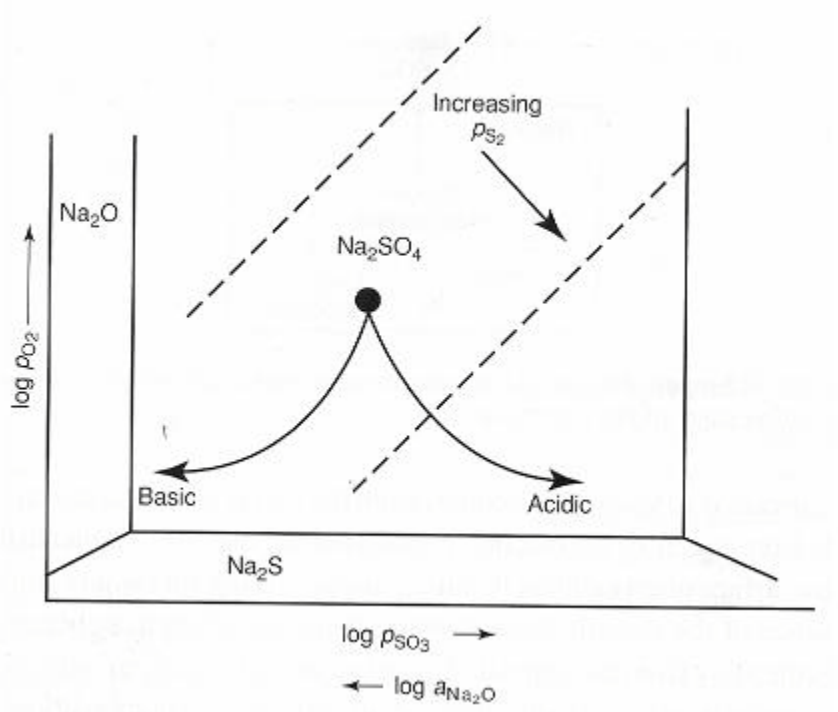

Figure 2. Schematic phase stability diagram for the Na-S-O system

This diagram illustrates roughly the compositional changes that can occur in the Na_2SO_4 deposit during the initiation stage. It is seen that locally the salt can become more basic (higher a_{Na_2O}) or more acidic (lower a_{Na_2O}) as a result of interaction with the underlying alloy. In certain situations, interaction with the gas can also be important.

Some of the most important factors influencing the processes which occur during the initiation stage as well as its duration, as outlined in detail in reference [7], are summarized below.

Alloy Composition: As noted above, Co-base materials generally exhibit extended initiation stages relative to Ni-base alloys during Type I hot corrosion; however, under Type II conditions, the behavior of the two alloys systems is reversed. Deodeshmukh and Gleeson [8] found that the addition of Co to β-(Ni,Pt)Al coatings greatly decreased the resistance of these materials to Type II hot corrosion attack. In Sections 2.2.2 and 2.2.3, the mechanisms of hot corrosion propagation, in addition to the effect of composition on these processes, will be discussed in more detail.

Alloy Condition: The condition of the material, i.e., as-cast vs. homogenized vs. vapor deposited, can have a large effect on hot corrosion resistance. For example, the first metal to solidify in an as-cast material would be expected to be solute-lean. The incubation period can be extremely short in these localized Cr- and Al- depleted regions resulting in an overall reduction in corrosion resistance.

Gas Composition: The composition of the gas has a large impact on the duration of the initiation stage, particularly at temperatures below the melting point of Na_2SO_4. At these relatively low temperatures, commonly those considered during Type II hot corrosion, the initiation stage may persist indefinitely when SO_2/SO_3 are not present in the atmosphere. These gaseous species have a pronounced effect on the physical and chemical state of the salt deposit, the exact nature of which will be described subsequently.

Amount of Salt Deposit: It has been generally accepted that the greater the amount of salt deposited on a specimen, the more severe the hot corrosion. However, it has been observed in reference [8] that in most cases this is only true up to some limiting deposit thickness. The Type I hot corrosion resistance of (Ni,Pt)Al diffusion coatings was decreased when the salt deposition rate increased from 1 to 8 mg/cm^2. When the sample was buried in salt, no discernable hot corrosion attack was observed. Similarly, minimal Type II hot corrosion attack was observed when a Ni-base superalloy was buried in salt, while severe attack occurred when deposits of 1 to 8 mg/cm^2 were applied.

Temperature: The exposure temperature has a marked effect on the observed hot corrosion processes. As previously mentioned, it is well accepted that a molten salt deposit is required to initiate severe hot corrosion. At temperatures above the melting temperature of Na_2SO_4, the salt will clearly be molten and conditions may develop which are conducive to Type I attack. Below this temperature, severe corrosion will typically not occur in the absence of SO_2/SO_3 gas mixtures or other salt deposits which may form eutectics with Na_2SO_4.

2.2.1.2 Propagation Stage

Three commonly encountered propagation modes have been mechanistically developed in the literature: basic fluxing, alloy-induced acidic fluxing, and gas phase-induced acidic fluxing. The first two occur at relatively high temperatures (~900°C - 1000°C) and thus fall into the category of high temperature (Type I) hot corrosion. Gas phase-induced acidic fluxing occurs at lower

temperatures (~650°C - 750°C) and is, therefore, termed low temperature (Type II) hot corrosion. Which of these propagation modes occurs is largely dependent on the way in which the alloy and salt are preconditioned during the initiation stage; all of the variables discussed in section 2.2.1.1 are therefore extremely influential.

Na_2SO_4 is an oxyanion salt which displays an acid-base character with SO_3(g) being the acidic component and oxide ions, present as Na_2O, the Lewis base [9]. With this convenient definition, one can describe the composition of a Na_2SO_4 melt by specifying an oxygen potential, p_{O_2}, and a basicity, $-\log a_{Na_2O}$. Equivalently, the salt chemistry can be expressed by considering the SO_3 potential in the melt, since this is linked to the Na_2O activity via the equilibrium represented in Equation (5) [6]:

$$Na_2SO_4(l) = SO_3(g) + \underline{Na_2O} \quad (5)$$

An underlined chemical formula indicates that the species is in solution.

Thermodynamic stability diagrams are very useful in describing the phases which are expected to be stable during hot corrosion. Figure 3 shows such a diagram for the Cr-S-O system superimposed onto the Na_2SO_4 portion of the Na-S-O stability diagram for T = 1200K [10]. In these isothermal diagrams, $\log p_{O_2}$ is plotted vs. $-\log a_{Na_2O}$, and the thermodynamically stable phase under a given set of conditions can be clearly ascertained.

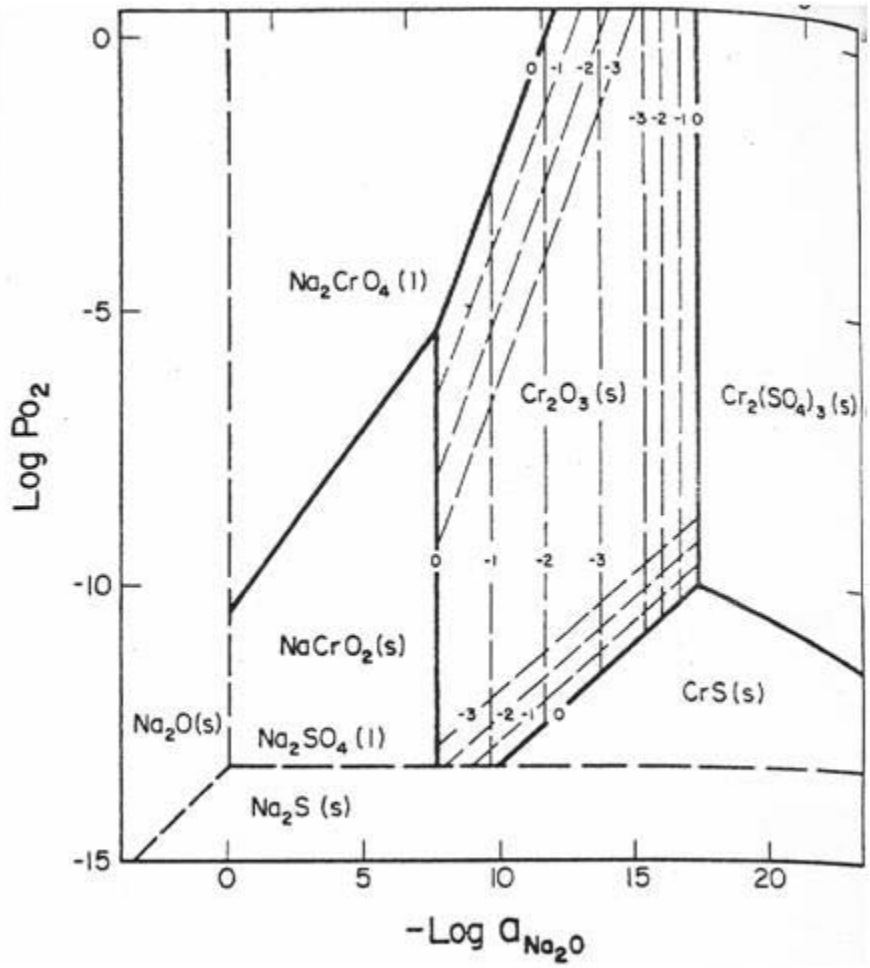

Figure 3. Phase stability diagram for the Cr-S-O system superimposed on the stability diagram for the Na-S-O system

Such compound phase stability diagrams are extremely useful when one is attempting to determine if a given protective oxide, Cr_2O_3 in this example, will dissolve in the presence of a molten salt, and if so, what solutes will be expected. According to Figure 3, Cr(s) is never stable in the presence of molten Na_2SO_4 at 1200K. Also, we see that at this temperature there are four possible solute species that can form, two basic solutes and two acidic solutes. Cr_2O_3 dissolves as one of the basic solutes, Na_2CrO_4 or $NaCrO_2$, in moderately basic salts. Conversely, if acidic conditions are developed in the salt, chromia can dissolve as either $Cr_2(SO_4)_3$ or CrS, depending on the oxygen potential. Similar diagrams for the other pertinent oxides have been developed in references [11-14].

It is of great engineering importance not only to know the identities of the stable phases as a function of salt composition, but also the degree to which a given oxide will dissolve in the melt. Using high temperature reference electrodes, the solubilities of NiO, Co_3O_4, and Al_2O_3 in Na_2SO_4 melts have been measured as a function of melt basicity at p_{O_2} = 1 atm and T = 1200°K [11-14]. A compilation of the results, combined with similar curves for Fe_2O_3 and Cr_2O_3, is presented in Figure 4 [10]:

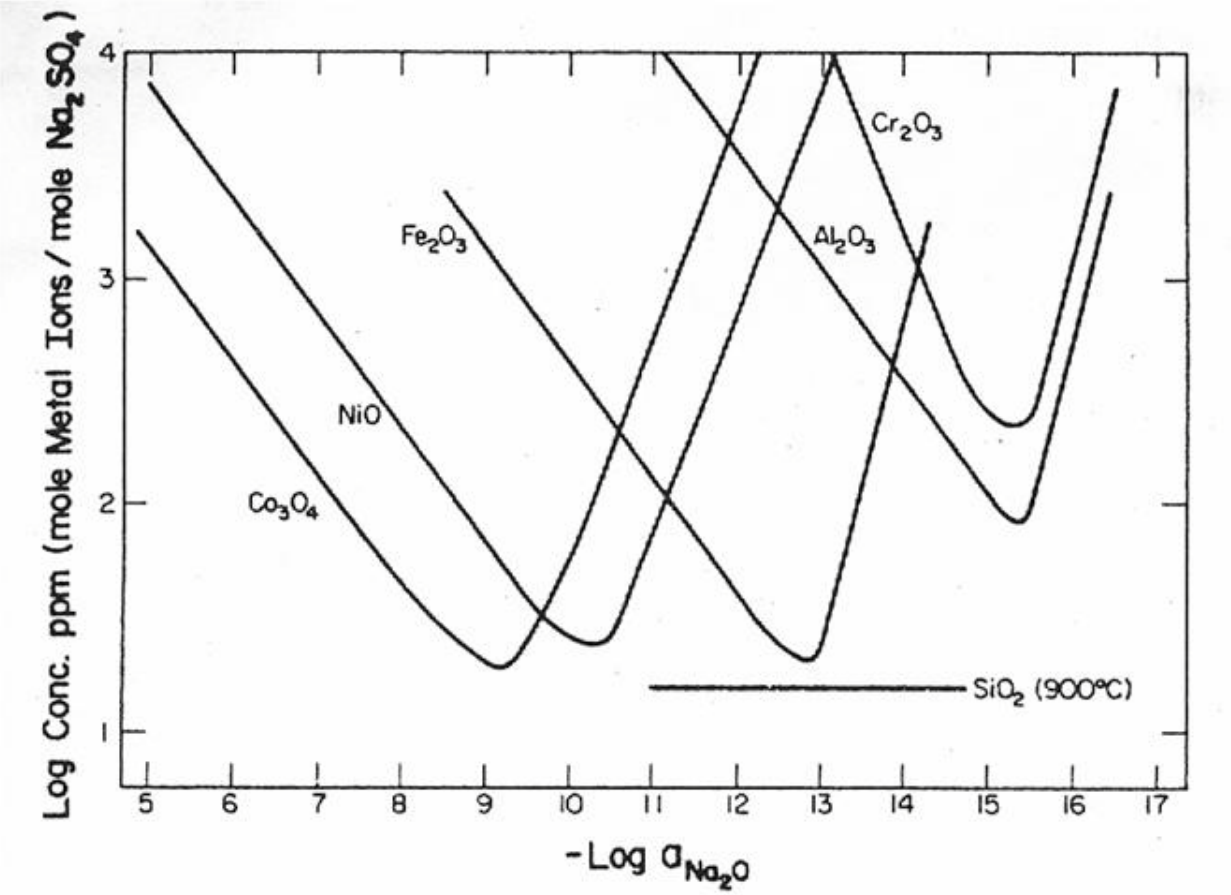

Figure 4. Solubilities of various oxides in Na_2SO_4 as a function of melt basicity

It is observed that the solubility minima for these oxides occur over a range of approximately 6 orders of magnitude with respect to salt basicity, which clearly demonstrates the importance of local salt chemistry on the hot corrosion process.

It is also worthwhile to note that the above solubility plots are constructed at a constant p_{O_2}. In general, these oxide solubilities will be a function of oxygen potential. Consider the basic dissolution of Cr_2O_3 and Al_2O_3 in Na_2SO_4 [6]:

$$Cr_2O_3 + 2Na_2O + \frac{3}{2}O_2 = 2Na_2CrO_4 \quad (6)$$

$$Al_2O_3 + Na_2O = 2NaAlO_2 \quad (7)$$

According to Equations (6) and (7), the Cr ion is oxidized from Cr^{3+} to Cr^{6+} during basic dissolution, while no such change in valence occurs for the Al^{3+} ion. As a result, the solubility of Cr_2O_3 in Na_2SO_4 is expected to increase with p_{O_2}, while the solubility of Al_2O_3 should exhibit no such dependence. These p_{O_2} dependencies have been measured for Cr_2O_3 [15], Fe_2O_3 [16], and Fe_3O_4 [16], for which very good agreement has been observed.

The shapes of these solubility curves can be predicted with remarkably good accuracy by simple thermodynamic calculations. Nickel oxide will be considered as an example. The reactions for the basic and acidic dissolution of NiO are shown in Equations (8) and (9), respectively:

$$2NiO + Na_2O + \frac{1}{2}O_2 = 2NaNiO_2 \quad (8)$$

$$NiO + Na_2SO_4 = NiSO_4 + Na_2O \quad (9)$$

Assuming unit NiO activity, the equilibrium constant for the basic dissolution of NiO can be expressed as

$$K = \frac{a^2_{NaNi\,O_2}}{a_{Na_2O}p^{1/2}_{O_2}} \quad (10)$$

Taking the logarithm of both sides, solving for a_{NaNiO_2}, and differentiating with respect to $-loga_{Na_2O}$, one finds

$$\left[\frac{\partial log\, a_{NaNi\,O_2}}{\partial(-log\, a_{Na_2O})}\right] = -\frac{1}{2} \quad (11)$$

This is the slope of the leftmost portion of the NiO dissolution curve in Figure 4, i.e., the portion representing the basic dissolution of NiO. Similarly for the acidic dissolution reaction, Equation (9):

$$K = a_{NiSO_4} a_{Na_2O} \quad (12)$$

$$\left[\frac{\partial log\, a_{NiSO_4}}{\partial(-log\, a_{Na_2O})}\right] = 1 \quad (13)$$

Equation (13) gives the slope of the rightmost portion of the NiO dissolution curve in Figure 4, i.e. the portion representing the acidic dissolution of NiO.

Rapp and Goto [17] proposed a general criterion which must be fulfilled in order for self-sustained hot corrosion attack to occur. This useful criterion can be most simply expressed as

$$\left[\frac{d[oxide\ \ solubility\ ]}{dx}\right]_{x=0} < 0 \quad (14)$$

where x is the distance into the molten salt film from the oxide/salt interface. According to this proposed model, a negative gradient in the oxide solubility at the oxide/salt interface will result in the dissolution of the protective oxide at this interface and reprecipitation of the oxide as discrete, nonprotective particles in regions of the salt where the solubility is lower.

The oxide solubility which is addressed in Equation (14) is a function of melt basicity (Figure 4) and in some cases p_{O_2}. Therefore, at a constant p_{O_2}, a basicity gradient must develop in the salt such that the oxide solubility gradient is negative at the oxide/salt interface. The sign of this basicity gradient will depend on whether the oxide is dissolving as an acidic or basic solute. Figure 5 schematically shows conditions in the salt which would satisfy the Rapp-Goto criterion and allow the hot corrosion of a material with a hypothetical surface oxide to occur [17]:

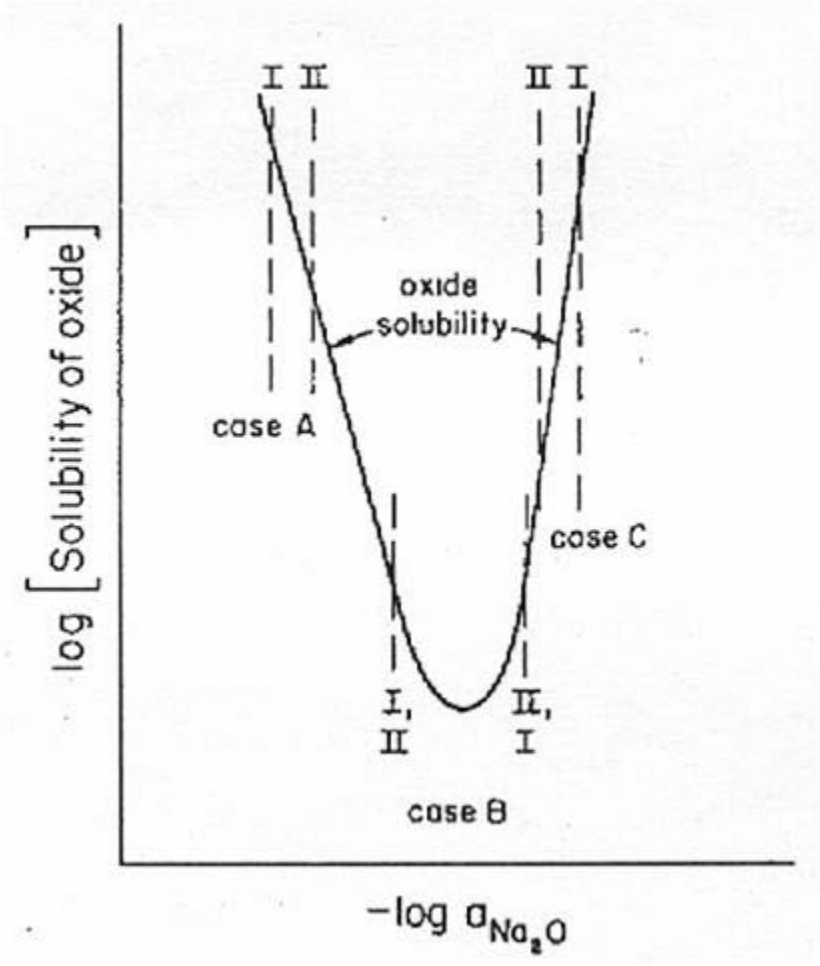

Figure 5. Schematic demonstration of Rapp-Goto criterion

In Figure 5, which is plotted for a constant $\boldsymbol{p_{O_2}}$, three situations (case A, case B, and case C) are shown in which basicity gradients, and thus oxide solubility gradients, in the salt are established such that continuing hot corrosion will occur. Dashed vertical lines labeled as I represent the locations of the oxide/salt interface in each of these cases, and the lines labeled as II represent the locations of the salt/gas interface. It is clearly observed that whether the dissolution is basic or acidic, the oxide solubility must be higher at interface I than it is at interface II (cases A and C). In case B, it is demonstrated that continued oxide dissolution can occur if the locations of the two relevant interfaces lie on either side of the solubility minimum for the oxide.

The discussion has thus far been concerned with hot corrosion in general and the thermodynamic tools which can be used to predict how it will proceed under various environmental conditions. In the following two sections, the exact processes which occur during hot corrosion induced by a thin film of fused Na_2SO_4 will be described in detail.

2.2.2 High Temperature (Type I) Hot Corrosion

Type I hot corrosion is known to occur at relatively high temperatures, approximately 900°C - 1000°C. There are generally two forms of this high temperature attack which can occur. One involves the dissolution of the protective oxide scale due to the formation of a highly basic melt (high a_{Na_2O}) and the other results from the development of a highly acidic melt (high p_{SO_3}). In spite of the obvious differences that exist between these two modes of corrosion, they have in common (as do all hot corrosion processes) the characteristic that the local corrosive conditions in the salt arise from the interaction between the salt and the underlying material. It will be seen that differences in the alloying elements in various materials will in large part determine which form of hot corrosion predominates. Dissolution of oxides into a basic melt, henceforth referred to as basic fluxing, was the first hot corrosion mechanism to be studied and characterized mechanistically.

2.2.2.1 Basic Fluxing

In the early stages of hot corrosion research, it was quickly recognized that a salt deposit composed principally of Na_2SO_4 was responsible for the observed accelerated oxidation, however there were a number of schools of thought concerning the operative degradation mechanism. The first of these was primarily focused on the oxidation of sulfide phases which were commonly observed in hot corrosion (a.k.a. "sulfidation") microstructures. Simons et al [18] were among the first to suggest that sulfidation attack was the result of rapid oxidation of sulfide phases which form when a reducing agent in the alloy reacts with the salt deposit. Quets and Dresher [19] were also advocates of the sulfidation/oxidation mechanism. They suggested, however, that the formation of alkali compounds such as $NaAlO_2$ and Na_2CrO_4 were necessary to achieve sulfur potentials which were sufficient to form sulfides within the alloy.

An alternative stance was that taken by Danek [20] and Seybolt [21]. These investigators concluded that the decreased oxidation resistance observed in the presence of Na_2SO_4 films was attributable to Cr-depletion in the substrate alloy. Seybolt [21] studied ternary Ni-Cr-X alloys as well as various commercial Ni-base superalloys and determined that the decrease in oxidation resistance in the presence of the salt is the result of Cr-depletion which results from the precipitation of Cr_xS_y particles within the alloy. This hypothesis was tested by oxidizing a Udimet 500 specimen which was modified such that the Cr content was reduced to levels found in the regions adjacent to chromium sulfides in previously hot corroded specimens. This modified superalloy did indeed demonstrate reduced oxidation resistance. The author also concluded that the oxidation of chromium sulfides perpetuates the reaction by releasing sulfur according to the following reaction:

$$2CrS + 3O = Cr_2O_3 + 2S \qquad (15)$$

This sulfur can then diffuse into the alloy resulting in further chromium sulfide formation. When the oxidation front reaches these new sulfides, they will be oxidized, releasing sulfur, and the process will continue.

The first step towards the currently-accepted basic fluxing mechanism was taken by Bornstein and DeCrescente [22]. These investigators studied the oxidation of three superalloys, B-1900, U-700 (both Al_2O_3-formers), and Waspaloy (Cr_2O_3-former) at 900°C with and without deposits of Na_2SO_4 and $NaNO_3$. A sulfur impregnation was also performed prior to oxidation both with and without a $NaNO_3$ deposit. The experiments were carefully designed mainly to test

the importance of sulfur in the hot corrosion process. The results showed that both salts resulted in the same amount of degradation, which was greatly accelerated in the case of the alumina-formers and not in the case of Waspaloy. The only microstructural difference was the formation of sulfides when Na_2SO_4 deposits were applied; sulfides were clearly absent when $NaNO_3$ was deposited. All salt-induced corrosion produced microstructures consisting of a porous external oxide and an alloy-depleted zone beneath the scale. Importantly, sulfur impregnation did not accelerate the oxidation of any specimen with or without a $NaNO_3$ deposit. The authors concluded that the formation and/or oxidation of sulfides does not directly cause the observed accelerated oxidation during hot corrosion. Rather, it is an interaction between oxide ions in the salt and the substrate which renders the scale non-protective and results in accelerated rates of degradation. When Na_2SO_4 is applied, the removal of sulfur from the salt via chromium-rich sulfide formation in the substrate produces oxide ions in the melt. These accrued oxide ions (present as Na_2O) somehow interact with the substrate resulting in accelerated oxidation.

Goebel and Pettit [23] conducted a series of experiments with pure Ni in order to test and further develop this theory. It was first determined that a condensed salt is necessary for hot corrosion attack of pure Ni to occur; gaseous Na_2SO_4 did not result in the accelerated oxidation which is observed when the sulfate is condensed. The condensed salt has the same composition as the vapor from which it condensed. Therefore, a concentration gradient must develop across the molten salt which is unable to form in the gaseous phase due to rapid transport rates.

Specimens of Ni oxidized at 1000°C in the presence of a molten Na_2SO_4 deposit generally displayed accelerated oxidation kinetics during the early stages of exposure which slowed to normal parabolic growth kinetics after approximately 6 minutes [23]. The microstructure consisted of an internal layer of NiS below a dense layer of NiO, above which a porous, nonprotective NiO layer was present. These observations led the authors to the following mechanism for the hot corrosion of Ni at 1000°C which is still accepted today.

By constructing a phase stability diagram for the Na-Ni-S-O system, it was determined that in the presence of laboratory grade Na_2SO_4 at 1000°C, NiO should be stable on the surface of Ni [23]. The oxygen required for NiO formation must be supplied either by gaseous oxygen dissolved in the molten salt or by the decomposition of sulfate ions, Equation 16:

$$SO_4^{2-} = S^{2-} + 2O_2 \quad (16)$$

As oxygen is consumed at the NiO/salt interface, a p_{O_2} gradient will develop across the salt if molecular oxygen is unable to diffuse to the interface from the atmosphere. It has been shown that the solubility of oxygen in Na_2SO_4 is in fact quite low, and the oxidant with significant solubility in the salt is SO_3 (as $S_2O_7^{2-}$) [24-27]. Therefore, a positive oxygen gradient will develop at the NiO/Na_2SO_4 interface, resulting in a locally high sulfur potential according to:

$$\frac{1}{2}S_2 + \frac{3}{2}O_2 = SO_3 \quad (17)$$

In the presence of two oxidants, S_2 and O_2 in this case, both at sufficient activities to form their respective phases (sulfide and oxide) in the absence of the other oxidant, phase stability at the metal surface will be determined by the ratio $\frac{p_{O_2}}{p_{S_2}}$ according to Equation 18:

$$NiO + \frac{1}{2}S_2 = NiS + \frac{1}{2}O_2 \quad (18)$$

Therefore, at the surface of the NiO, NiS will likely be unstable unless very significant amounts of oxygen are removed from the salt. However, if sulfur can diffuse through the oxide to the region of low p_{O_2} at its base, it has been demonstrated that a subscale of NiS can form beneath the NiO[28], which was indeed observed. As sulfur is removed from the Na_2SO_4 adjacent to the substrate by diffusing through the NiO scale to form internal NiS, oxide ions are produced in this region according to Equation 19:

$$SO_4^{2-} = O^{2-} + \frac{1}{2}S_2 + \frac{3}{2}O_2 \quad (19)$$

Thus, the net effect of sulfur removal is an increase in the oxide ion activity at the salt/scale interface, described by the following overall reaction:

$$Na_2SO_4 + 3Ni = 3NiO + Na_2O + \frac{1}{2}S_2 \quad (20)$$

When the oxide ion activity in the melt adjacent to the NiO scale reaches sufficiently high values, the following reaction can occur:

$$NiO + Na_2O = Na_2NiO_2 \quad (21)$$

i.e. NiO reacts with oxide ions in the melt to form nickelate ions, NiO_2^{2-}, which are soluble in molten Na_2SO_4. The high oxide ion activity which is achieved is localized at the salt/scale interface, and therefore as the nickelate ions diffuse out into the salt, they encounter regions of lower oxide ion activity and precipitate out as discontinuous, nonprotective oxide particles

according to the reverse of Equation 21. This, the researchers proposed, is the source of the porous NiO scale observed on hot corroded pure Ni.

As mentioned above, the accelerated oxidation of Ni seems to come to a halt after approximately 6 hours at 1000°C [23]. To explain this, it is noted that eventually very high oxide ion activities will result in very low sulfur potentials, NiS will cease to be formed and the oxide ion concentration will stabilize at some higher level. When this occurs, a continuous, protective layer of NiO will form below the porous outer scale and the accelerated oxidation will stop.

It is instructive to evaluate this mechanism in terms of the Rapp-Goto criterion, which is concisely stated in Equation 14 [17]. During the accelerated period of oxidation, the oxide ion activity is higher at the NiO/salt interface than it is in regions of the salt further from this interface. According to Equation 21, this is equivalent to stating that the NiO solubility is greater at the NiO/salt interface that it is further out in the salt, i.e. there is a negative gradient in the oxide solubility at this interface (see Figure 5, Case A). According to Equation 14, accelerated oxidation should occur, as observed. When NiS formation ceases and the oxide ion activity stabilizes throughout the salt, the NiO solubility gradient flattens and accelerated oxidation stops, in accord with Eq. 14.

Further tests were conducted by Goebel and Pettit to determine the effect of sulfur on the hot corrosion of Ni-base alloys [29]. Pure Cr, Ni-Cr, Ni-Al, and various chromia- and alumina-forming superalloys were oxidized in pure O_2 at 1000°C after a presulfidizing treatment in an H_2/H_2S environment in order to observe the effect of sulfur on the subsequent oxidation behavior of these materials. In the case of pure Cr, the presulfidation treatment had no effect on the oxidation behavior; a protective layer of Cr_2O_3 formed over the preformed layer of CrS. During the oxidation of the Ni-Cr alloys, it was observed that presulfidation increased the rate of oxidation only if NiS was formed, which is liquid at 1000°C. If this occurs, the external Cr_2O_3 layer is permeated with NiS, which provides rapid diffusion paths for oxygen, and oxidation is accelerated. Al_2O_3-forming Ni-Al alloys oxidized at an accelerated rate only if the Al activity in the alloy was high enough to form Al_2S_3. The subsequent oxidation of these sulfides resulted in a release of SO_2 per Equation 22

$$Al_2S_3 + \frac{9}{2}O_2 = Al_2O_3 + 3SO_2 \qquad (22)$$

which prevented the formation of a protective Al_2O_3 layer. If the Al activity was insufficient to form Al_2S_3, only NiS was formed, and during oxidation Al was selectively oxidized to form a

protective external Al_2O_3 scale. The chromia forming superalloys behaved similarly to the Ni-Cr alloys during oxidation, while the alumina forming superalloys behaved similarly to the Ni-Al alloys which did not form Al_2S_3. These results showed that hot corrosion mechanisms which depend on oxidation of sulfides at temperatures ~1000°C are only feasible for non-Al_2O_3-forming superalloys and high activity Ni-Al alloys, and are therefore generally inaccurate.

Bornstein and DeCrescente [30] oxidized samples of B-1900, Waspaloy, and various binary Ni-Cr and Ni-Al alloys at 800°C - 1000°C with deposits of Na_2SO_4 and Na_2CO_3 to further understand the effect of deposit composition on the hot corrosion process. It was observed that the oxidation of the Al_2O_3-forming B-1900 alloy was accelerated equally by both salts. The kinetics of the oxidation in the presence of each salt could be described by a modified parabolic relationship, suggesting that diffusion through the scale was the rate limiting process. However, removal of the scale during the test resulted in no change in the oxidation rate. Arrhenius plots were used to determine that the activation energies for both processes were approximately equal. Oxidation of the Cr_2O_3 - forming Waspaloy was not accelerated by either salt and displayed parabolic scale-growth kinetics. Ni-5Cr, Ni-8Cr, Ni-13Cr, and Ni-17Cr alloys did not oxidize in an accelerated manor at 900°C or 1000°C, but the two higher-Cr alloys showed steady weight losses after approximately 100 minutes at 1000°C in the presence of both deposits. Soluble chromium was found in the wash water after exposure of the binary Ni-Cr alloys. Finally, Na_2CO_3 deposits did not cause accelerated degradation of pure Ni, however Ni-1Al was oxidized at a rate similar to that observed for B-1900 with this same deposit. It had previously been shown that the oxidation of pure Ni is greatly enhanced by Na_2SO_4 [23].

A number of conclusions were drawn from this work [30]. Firstly, the lack of degradation of the Ni-Cr alloys suggests that Cr is beneficial for hot corrosion resistance due to the formation and dissolution of Cr_2O_3, which lowers oxide ion levels at the oxide/salt interface according to the following reaction:

$$Cr_2O_3 + 2Na_2O + \frac{3}{2}O_2 = 2Na_2CrO_4 \qquad (23)$$

This was substantiated by chemical analysis of the wash water from these specimens, which revealed the presence of Cr. The authors also concluded that the weight losses observed in the case of the Ni-13Cr and Ni-17Cr at 1000°C were due to the evaporation of Na_2CrO_4.

It has been observed that the equilibrium oxide ion content of Na_2CO_3 is at least as high as that of Na_2SO_4 at 1000°C [20]. Therefore, to explain the observation that Na_2CO_3 did not

result in rapid oxidation of pure Ni, while Na_2SO_4 did result in such attack, it was mentioned that while NiS formation results in an increase in oxide ion activity in the presence of a sulfate deposit, there is no analogous reaction for a carbonate deposit [23]. It was asserted that the oxidation of Ni-1Al is accelerated by Na_2CO_3 because the formation of $NaAlO_2$ promotes the formation of oxide ions. The proposed reaction was not, however, explained in detail.

Goebel et al [31] performed a number of oxidation experiments on various commercial and model alloys containing elements such as Cr, Al, Mo, W, and V in order to clearly determine the effect of alloy composition on Na_2SO_4-induced hot corrosion. It was concluded that there are generally two types of high temperature hot corrosion: Na_2SO_4-induced accelerated oxidation and Na_2SO_4-induced catastrophic oxidation. The latter has since been termed "alloy-induced acidic fluxing" and will be discussed in more detail in Section 2.2.2.2. The former, Na_2SO_4-induced accelerated oxidation, is a basic fluxing mechanism which was found to occur when the alloy contained no molybdenum (catastrophic oxidation, as will be seen, occurs when elements typified by Mo are present in the alloy). Ni-1Al and Ni-31Al alloys showed slightly accelerated oxidation in the presence of 0.5 mg/cm^2 Na_2SO_4, and in the presence of thicker deposits a very rapid, breakaway oxidation was observed for the Ni-31Al. Sulfur entered the alloy from the beginning of the exposure, and water soluble $NaAlO_2$ was formed via reaction between Na_2SO_4 and Al_2O_3. Ni-5Cr and Ni-30Cr alloys formed protective external NiO and Cr_2O_3 scales, respectively, and the Na_2SO_4 turned yellow during exposure because of the dissolution of chromate ions, which were detected in the wash water. SO_2 was detected in the effluent gas, indicating that the following reaction was taking place:

$$Cr_2O_3 + \frac{1}{2}O_2 + 2Na_2SO_4 = 2Na_2CrO_4 + 2SO_2 \qquad (24)$$

Finally, Ni-30Cr-6Al and Ni-11Cr-22Al each gained less weight than in simple oxidation, while Ni-8Cr-6Al (a marginal Al_2O_3-former) was severely degraded. It seems that the first two Ni-Cr-Al alloys are able to form a protective Al_2O_3 scale as transient Cr_2O_3 lowers the oxide ion content of the salt via Equation 24, while the Cr-depletion resulting from this reaction is enough to prevent protective Al_2O_3 scale formation on Ni-8Cr-6Al (the presence of Cr in Ni-Cr-Al alloys produces a third element effect, i.e., it allows the selective oxidation of Al to occur at lower Al activities than in binary Ni-Al alloys [32]).

A mechanism for the hot corrosion of Ni-31Al was developed from these experimental results [31]. It can be discussed with reference to the 1000°C Al-S-O phase stability diagram, presented in Figure 6.

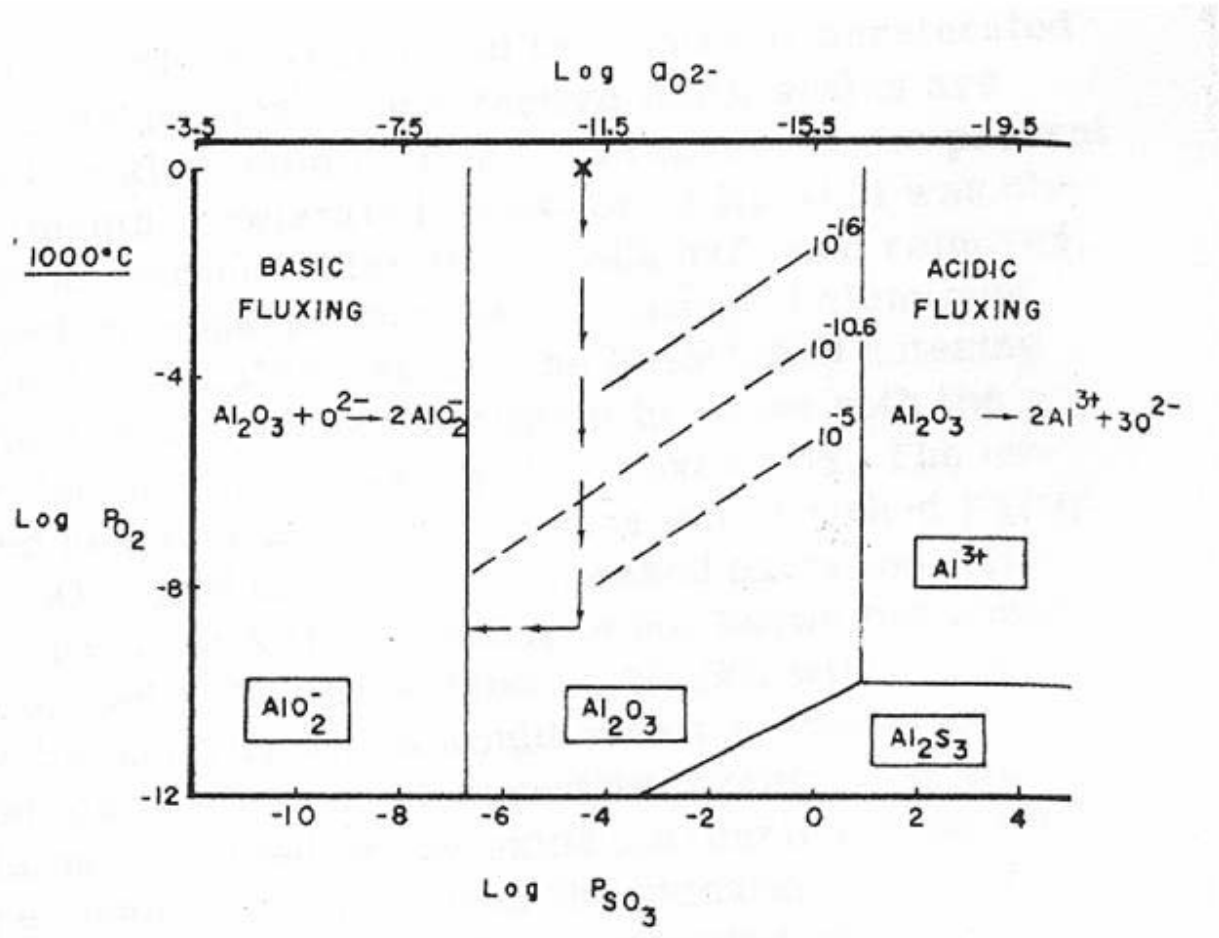

Figure 6. Phase stability diagram for the Al-S-O system showing a schematic of the Type I hot corrosion of Ni-Al alloys

In Figure 6, the composition of the as-deposited Na_2SO_4 is indicated by an x. At this composition, Al_2O_3 is stable, and therefore an alumina scale initially forms at the surface of the alloy. As oxygen from the salt is consumed, the p_{O_2} drops at the oxide/salt interface with a concomitant increase in the p_{S_2} in this region (indicated by the downward-pointing arrow in Figure 6). At a sufficiently high activity, sulfur diffuses through the Al_2O_3 scale and forms aluminum sulfides in the alloy. This results in a net increase in the oxide ion activity in the Na_2SO_4 at the oxide/salt interface according to the overall reaction:

$$\frac{2}{3}Al + Na_2SO_4 = Na_2O + \frac{1}{3}Al_2S_3 + \frac{3}{2}O_2 \qquad (25)$$

When sufficient oxide ion activities are achieved, the protective Al_2O_3 dissolves in accordance with Equation 7. This entire process is shown in Figure 6, where the broken diagonal lines represent sulfur isobars. In this schematic, the composition of the sulfate begins to move left to more basic compositions when the p_{S_2} reaches approximately 10^{-5} atm, which is presumably high enough to form Al_2S_3 at the scale/alloy interface. When the composition crosses the AlO_2^-/Al_2O_3 boundary, Al_2O_3 is no longer stable and will react rapidly with oxide ions, degrading by a so called basic fluxing mechanism.

The Ni-5Cr and Ni-30Cr specimens did not degrade at an accelerated rate because, as suggested by Bornstein and DeCrescente [30], chromia, present either as a continuous scale or a transient oxide, dissolves in the salt according to Equation 23 and prevents the development of high oxide ion activities [31]. The Ni-5Cr was actually observed to oxidize at a slower rate with a Na_2SO_4 deposit compared with simple oxidation, and this was attributed to a possible doping effect. Doping NiO with Na would result in a decrease in the cation vacancy concentration and thus a slower outward migration of Ni^{2+}, i.e. a slower scale growth rate.

Like Cr_2O_3, Al_2O_3 reacts with oxide ions to form a soluble species, AlO_2^-, however the beneficial effects of Cr_2O_3 are not observed with Al_2O_3. This was investigated by heating pure Al_2O_3 and pure Cr_2O_3 with reagent grade Na_2SO_4; a reaction between Cr_2O_3 and the salt was evident while there was no such reaction with Al_2O_3. Therefore, Cr_2O_3 has a stronger affinity for oxide ions than Al_2O_3 and consequently it is a better hot corrosion inhibitor.

Rapp and Goto [17] point out that while the removal of sulfur from the Na_2SO_4 to form sulfides does in fact increase the local melt basicity, the electrochemical reduction reaction will

have the same result. For example, they propose that, in a highly basic melt, the reduction of peroxide ions:

$$O_2^{2-} + 2e^- = 2O^{2-} \quad (26)$$

at the oxide/salt interface will result in an increase in basicity. Therefore, while sulfide formation may contribute to the establishment of basic fluxing conditions in the salt film, it is not the only factor to be considered.

2.2.2.2 Alloy-Induced Acidic Fluxing

It has been shown in section 2.2.2.1 that scale fluxing conditions can be established as a result of locally basic conditions at the salt/scale interface. This results in accelerated rates of degradation in many engineering alloys, however the attack is not self-sustaining. The oxide solubility plots of Figure 4 demonstrate that acidic melts (those with a low a_{Na_2O}) can also effectively dissolve protective oxide scales. Acidic conditions can generally be established in a Na_2SO_4 melt either by SO_3 in the gas or by the dissolution of acidic transient of W, Mo, or V, which are added to superalloys as solid-solution strengtheners [33]. The first process will be discussed in section 2.2.3; the latter, referred to as alloy-induced acidic fluxing, is the topic of this section.

Bornstein, DeCrescente, and Roth [34] studied the effects of various elements on the Na_2SO_4-induced accelerated oxidation of Ni-base alloys at temperatures of 800-1000°C. The hot corrosion rates of Al_2O_3-forming alloys were greatly enhanced when Mo or V were present in the alloys, or when Na_2SO_4 was co-deposited with MoO_3 or V_2O_5. The first possible explanation for this is that these acidic oxides react with oxide ions, liberating SO_2 according to, for example, Equation 27:

$$V_2O_5 + Na_2SO_4 = 2NaVO_3 + SO_2 + \frac{1}{2}O_2 \quad (27)$$

The SO_2 released from this reaction can then dissolve the Al_2O_3 scale, forming soluble sulfate:

$$Al_2O_3 + 3SO_2 + \frac{3}{2}O_2 = Al_2(SO_4)_3 \quad (28)$$

The authors assert, however, that in order for sufficiently high SO_2 potentials to be developed for reaction 28 to be feasible, the activity of SO_4^{2-} would have to deviate significantly from unity. In other words, the reaction between V_2O_5 and Na_2SO_4 (Equation 27) would have to be very rapid, which was not observed when the two substances were liquefied in a quartz tube.

Bornstein et al [34] therefore concluded that the accelerated attack is a result of the fact that MoO_3 and V_2O_5 are molten at the test temperatures. These molten, corrosive oxides flux the Al_2O_3 scale, resulting in rapid degradation of the Al_2O_3-forming alloys. No such degradation was observed in the presence of W because WO_3 is solid at the temperatures considered.

Goebel et al oxidized a number of Ni-Al and Ni-Cr-Al alloys containing W, Mo, and V in air with thin Na_2SO_4 deposits [31]. All alloys degraded catastrophically. It was observed that the refractory elements were enriched in the scale adjacent to the alloy/scale interface and that the attack initiated at refractory-element rich phases, e.g. α-Mo or Mo-carbide. In addition, oxides of W, Mo, V, and Cr were mixed with Na_2SO_4 and heated in an alumina crucible to 1000°C. In the cases of WO_3, MoO_3, and V_2O_5, the crucible lost weight and Al was detected in the salt after the test; no such effect was seen with Cr_2O_3. It was concluded that the first three aforementioned oxides lower the oxide ion content sufficiently for reaction 28 to occur; Cr_2O_3 reacts with oxide ions (Equation 24), however not to as great of an extent. Based on these observations, the following mechanism for alloy-induced acidic fluxing of Ni-Al-Mo alloys was developed. The analysis is applicable to any refractory element-containing alloy.

During the transient oxidation period, the oxides Al_2O_3, NiO, and MoO_3 form at the alloy surface. MoO_3 reacts with oxide ions in the salt according to Equation 29

$$MoO_3 + O^{2-} = MoO_4^{2-} \quad (29)$$

which prevents basic fluxing from occurring. The activity of oxide ions in the melt adjacent to the scale can be lowered by this reaction until reaction 28 becomes possible, i.e. the Al_2O_3 scale dissolves as an acidic solute. This attack is found to initiate near Mo-rich particles because the activity of MoO_3 is highest in the salt adjacent to these regions. Al^{3+} and MoO_4^{2-} ions diffuse out through the salt, where Al_2O_3 precipitates out as a porous, nonprotective scale and MoO_3 evaporates. Unlike basic fluxing, this attack is self sustaining due to the continued formation of MoO_3 at the alloy/salt interface and its evaporation at the salt/gas interface. In terms of the Rapp-Goto criterion [17], a negative solubility gradient is maintained in the salt at the salt/alloy interface.

2.2.3 Low Temperature (Type II) Hot Corrosion

An interesting characteristic of hot corrosion is that it tends to occur in perhaps its most severe form when the temperature is fairly low, approximately 650°C - 750°C. Na_2SO_4 is solid in this temperature regime, and thus one would expect negligible corrosion. Conde and Wareham [35], who demonstrated pitting corrosion of a Nimonic 105 blade after operating in a marine environment at a turbine inlet temperature of approximately 750°C, were among the first to prove the occurrence of hot corrosion at these low temperatures. From that point, numerous examples of this so called Type II hot corrosion were shown and a number of mechanistic studies were performed. Mechanisms have been developed which seem to be consistent with commonly encountered hot corrosion microstructures, however none of the mechanisms have achieved ubiquitous acceptance. It is generally agreed upon that accelerated degradation at these low temperatures is made possible by the formation of a Na_2SO_4/MSO_4 eutectic which has a melting point well below that of pure Na_2SO_4 [36]. It has been shown that a p_{SO_3} of approximately 10^{-5} atm is required to stabilize this eutectic melt [37]; these SO_3 pressures are not uncommon in the gas stream of an industrial or marine gas turbine. As first observed by Wortman et al [38], CoCrAlY coatings tend to be very susceptible to this form of hot corrosion, and thus the bulk of the work on Type II hot corrosion has centered on Co-base materials.

2.2.3.1 Gas Phase-Induced Acidic Fluxing

Numerous publications have documented the typical Type II corrosion morphologies, particularly in Co-base materials [37, 39-41]. Generally, Co-Cr-Al alloys exhibit severe localized attack in the form of deep pits containing mixtures of porous, nonprotective Cr_2O_3, Al_2O_3, $CoCr_2O_4$, and $CoAl_2O_4$ with a band at the base of the pit enriched in Al and S. Near the corrosion product/gas interface, a layer of Co_3O_4 and/or $CoSO_4$ is commonly observed, depending on p_{SO_3}. At high p_{SO_3}, $CoSO_4$ will tend to be the stable phase at the sample surface, while Co_3O_4 is stable at lower SO_3 potentials [39].

Binary Co-Cr alloys tend to have similar Type II corrosion morphologies, with the obvious exception that only Cr- and Co- rich corrosion products are present. Binary Co-Al alloys commonly experience a more frontal attack, however the elemental distributions are quite similar

to Co-Cr and Co-Cr-Al alloys [39]. Again, there is the trivial exception that only Al- and Co-rich corrosion products are present in these alloys.

It has been well established that a liquid Na_2SO_4 film is required for hot corrosion to occur, regardless of the temperature or active corrosion mechanism. In the case of low temperature hot corrosion, liquid deposits form at temperatures well below the melting point of pure Na_2SO_4 (T_m = 884°C). The $CoSO_4$-Na_2SO_4 phase diagram is shown in Figure 7 [42]:

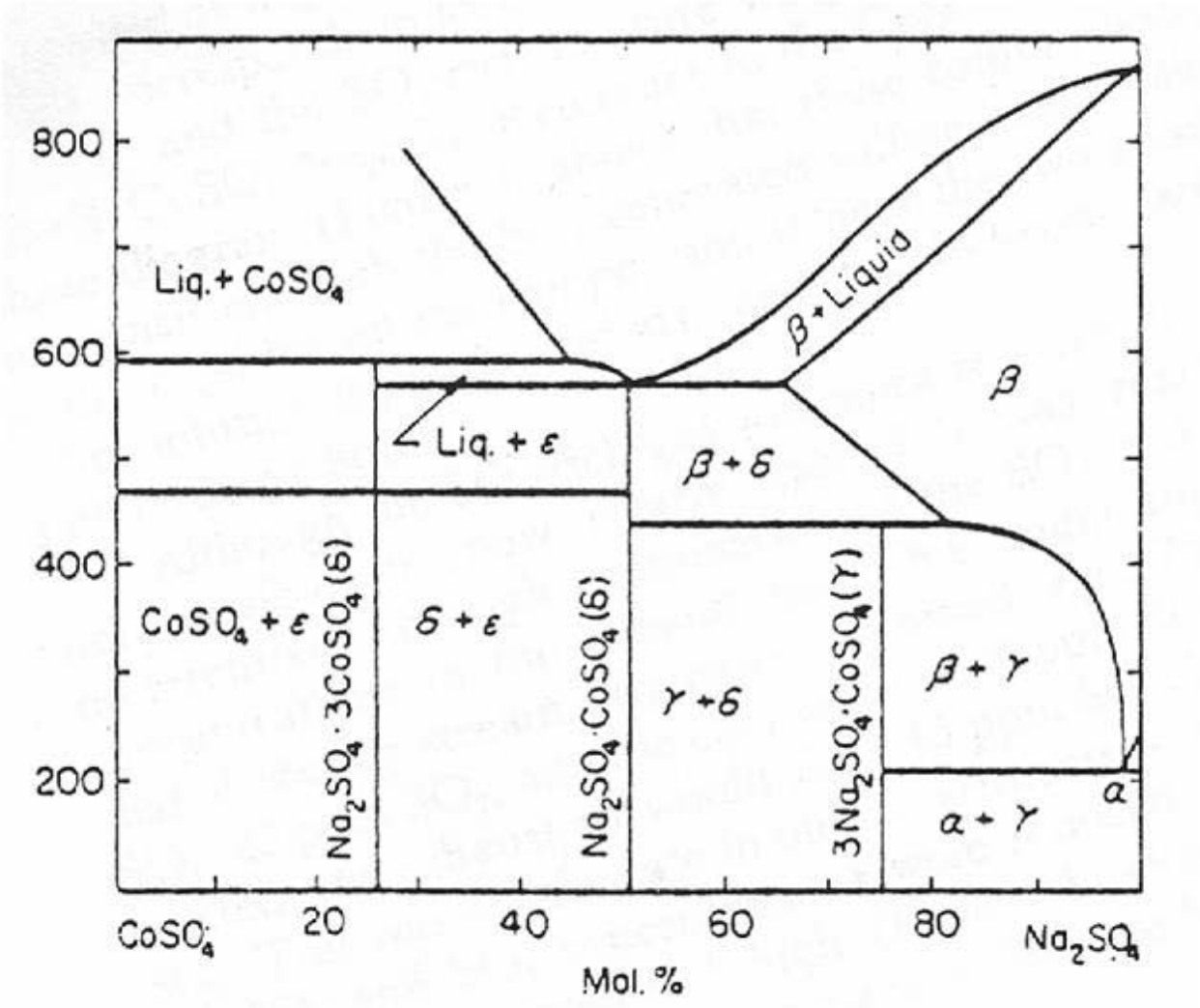

Figure 7. $CoSO_4$-Na_2SO_4 phase diagram

A eutectic is observed in this binary system at approximately 50 mol% Na_2SO_4 and 560°C. Therefore, if a sufficient activity of $CoSO_4$ can be established in the Na_2SO_4 film, liquid formation is expected at temperatures in the 650°C - 750°C range.

When an engineering alloy such as CoCrAlY is exposed to elevated temperatures in an oxidizing environment, it is commonly protected from this environment by a slow-growing external scale of α-Al_2O_3 during steady state oxidation. However, during the initial stages of exposure, oxides of all other elements in the alloy will form at the surface, provided that the free energy changes for their formations are negative under the given conditions. This process is known as transient oxidation [6]. Therefore, when a CoCrAlY alloy is covered with a solid Na_2SO_4 deposit and exposed at elevated temperatures, regions of relatively fast-growing Co_3O_4 and/or CoO (depending on temperature and p_{O_2}) are expected to nucleate. These transient oxides can be sulfidized according to Reactions 30 and 31:

$$\frac{1}{3}Co_3O_4 + SO_3 = \underline{CoSO_4} + \frac{1}{6}O_2 \quad (30)$$

$$CoO + SO_3 = \underline{CoSO_4} \quad (31)$$

In these reactions, $CoSO_4$ is underlined, meaning that it is dissolved in Na_2SO_4 at less than unit activity. If a high enough SO_3 potential is present in the combustion gas, the activity of $CoSO_4$ in the salt can reach levels sufficient for eutectic formation.

Based on available thermodynamic data, Luthra and Shores [43] generated a plot showing the SO_3 potential required to form solid $CoSO_4$ and a liquid eutectic mixture from pure Co_3O_4 at p_{O_2} = 1atm, shown in Figure 8:

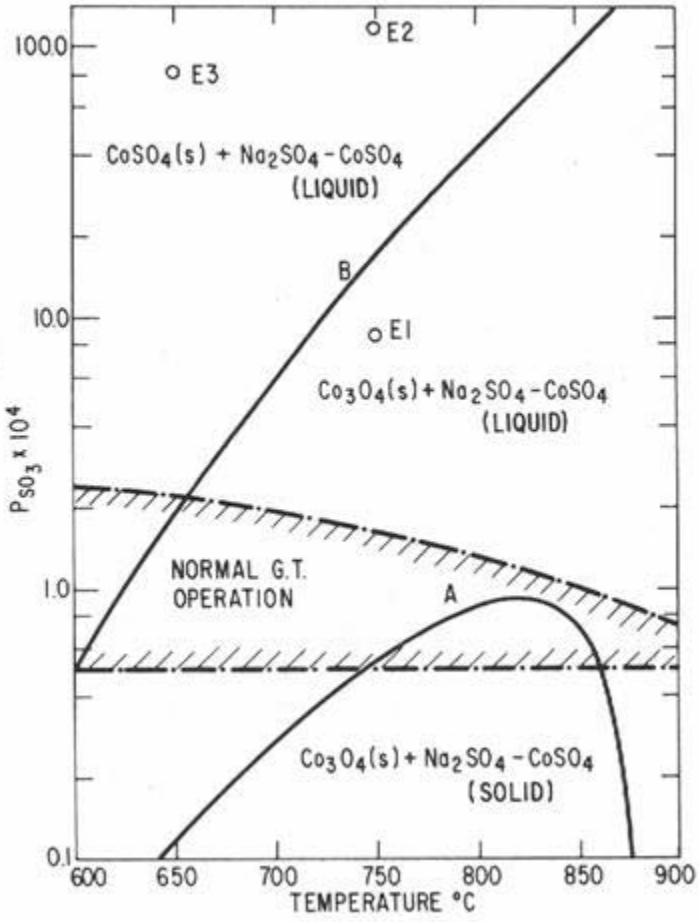

Figure 8. P_{SO_3} required to form various species

A Na_2SO_4-$CoSO_4$ liquid is stable above line A. It can be seen that the eutectic is stable over a wide range of SO_3 potentials which can typically be achieved in a gas turbine engine (common gas turbine operating conditions are contained within the dashed lines). The authors note that this plot is generated only for p_{O_2} = 1atm, and that the location of the curves will change with p_{O_2} per Reaction 30. Assume that a turbine is operating at a total pressure of 10 atm, corresponding to a p_{O_2} of approximately 1.6 atm. The result of this increase in oxygen potential would be a 7% increase in the p_{SO_3} levels required for eutectic formation (curve A). This fairly small change does not render the given plot ineffective for application to real gas turbine systems.

Jones [42] further elucidated the nature of the interaction between Co_3O_4 and SO_2/SO_3 mixtures. Mixtures of Co_3O_4 and Na_2SO_4 were exposed to gas mixtures rich in SO_2 and/or SO_3 and monitored via weight gain measurements, observation of the physical state of the mixture, measurement of the amount of SO_2 consumed from the incident gas stream, and measurement of SO_3/SO_2 ratios in the exiting gas. It was determined that indeed SO_3 and not SO_2 is the important species in converting cobalt oxide to sulfate. However, it was found that Co_3O_4 is a catalyst for the typically sluggish reaction

$$SO_2 + \frac{1}{2}O_2 = SO_3 \qquad (32)$$

Therefore, even if the inlet and exit gases consist solely of SO_2, significant eutectic formation can occur due to locally high SO_3.

Luthra [44] proposed an interesting mechanism for low temperature hot corrosion attack of Co- base alloys. He pointed out that at the SO_3 potentials required for this type of attack, alumina and chromia will dissolve as sulfates, i.e. basic fluxing cannot occur. Further, the p_{SO_3} will be higher at the salt/gas interface than at the salt/alloy interface, and thus a positive acidic solubility gradient will exist in the salt. In addition, over the range of experimental conditions (p_{SO_3} and p_{O_2}) examined in his study, Al_2O_3 and Cr_2O_3 should be stable and form a protective

layer, which was not observed. Therefore, the concept of scale fluxing as it was developed for Type I hot corrosion does not seem to be applicable for Type II degradation.

Transport rates of SO_2 and SO_3 through molten Na_2SO_4 in ionic and molecular form were calculated and it was found that only SO_3, present as dissolved $S_2O_7^{2-}$ ions, was capable of providing a large enough flux of oxidant to the salt/alloy interface to account for the observed weight gains during corrosion [44]. At the salt gas interface, the reaction

$$Na_2SO_4 + SO_3 = Na_2S_2O_7 \quad (33)$$

incorporates SO_3 into the salt. It is then transported towards the salt/alloy interface by the $SO_4^{2-}/S_2O_7^{2-}$ exchange reaction shown schematically in Reaction 34:

$$S_2O_7^{2-} + SO_4^{2-} + SO_4^{2-} = SO_4^{2-} + S_2O_7^{2-} + SO_4^{2-} \quad (34)$$

At the salt/alloy interface, SO_3 is the primary oxidant. Very low p_{O_2} levels will develop at this interface, resulting in a high p_{SO_2} if $O_2/SO_2/SO_3$ equilibrium is assumed. Thus, SO_2 will likely migrate out through the salt.

Cobalt is very commonly observed in the outer regions of the corrosion product as Co_3O_4, meaning that it must somehow migrate out through the salt. Co is a transition metal which can exist in the 2+ or 3+ valence states. In order for Co migration to occur, there must be some coupled ionic migration as a result of electrical neutrality requirements. Luthra determined three possibilities for such migration [44]. The first involves the outward migration of Co^{2+} and SO_4^{2-}, which would require that the activity of $CoSO_4$ is greatest at the scale/alloy interface. At high SO_3 pressures, $CoSO_4$ is observed at unit activity at the surface of the corrosion product formed on CoCrAlY specimens, and so this cannot be the mechanism. The second possibility is a coupled outward migration of Co^{2+} and SO_3^{2-}. There should be a negative gradient in the activity of SO_3^{2-} at the scale/alloy interface, where the p_{O_2} is low, per Reaction 35:

$$Na_2SO_3 + \frac{1}{2}O_2 = Na_2SO_4 \quad (35)$$

However, Fick's 1st Law considerations showed that the flux of Co provided by this mechanism is much less that that observed experimentally, and so this is also unlikely. The final mechanism for Co transport, that which is proposed to be operative during Type II hot corrosion, involves a $3Co^{2+}/2Co^{3+}$ exchange reaction.

According to Reaction 36, the Co^{3+}/Co^{2+} ratio will be higher at the salt/gas interface than it is at the salt/alloy interface:

$$2\underline{CoSO_4} + SO_3 + \frac{1}{2}O_2 = \underline{Co_2(SO_4)_3} \quad (36)$$

This results in a net outward transport of Co due to an inward migration of Co^{3+}, which is reduced at the salt/alloy interface, and an outward transport of Co^{2+}, which forms Co_3O_4 and/or $CoSO_4$ toward the salt/gas interface.

Thus, a reaction sequence was developed for the Type II hot corrosion of Co- base alloys which is based on the acidic fluxing of Co and its oxides [44]. Binary Co-Cr alloys will be used as an example. Initially, during transient oxidation, oxides of Co and Cr form on the alloy surface. Co_3O_4 reacts with SO_3 to form $CoSO_4$, which dissolves in the solid Na_2SO_4. If sufficient SO_3 is present, a liquid Na_2SO_4-$CoSO_4$ eutectic forms, and porous, nonprotective Cr_2O_3 is left behind. The reaction is perpetuated by the inward migration of SO_3 (as $S_2O_7^{2-}$) and the outward migration of Co^{2+}. SO_3 oxidizes Cr at the salt/alloy interface, releasing SO_2 which can penetrate the alloy and form sulfides. This accounts for the S-rich band commonly observed at the base of the corrosion pit. These sulfides can be oxidized as the corrosion front progresses, releasing sulfur, which can form sulfides deeper in the alloy. Therefore, the boundary between the alloy and the sulfur-rich band, as well as that between the sulfur-rich band and the rest of the pit, advance further into the sample. Eventually, the maximum $CoSO_4$ activity is reached at the salt/gas interface, and solid Co_3O_4 precipitates in this region.

This reaction is unlikely for Ni-base alloy systems because there are no known compounds of Ni^{3+}. Also, $NiSO_4$ is much less stable than $CoSO_4$.

Chiang et al [41] studied the low temperature hot corrosion of binary and ternary Ni- and Co- base alloys at 700°C and 750°C. All binary (Ni,Co)-Cr and ternary (Ni,Co)-Cr-Al alloys exhibited the degradation microstructure typical for Co-Cr-Al, as described at the beginning of this section, however some additional observations were made. Sulfides of Cr were prevalent beneath the corrosion pits in the Ni-base alloys, and NiS was present within the corrosion product. Also, higher SO_3 pressures were required to produce significant degradation in the Ni-base systems relative to the Co-base systems. Preferential attack of Co-18Cr-6Al occurred along the β-CoAl phase.

The following reaction mechanism for Type II hot corrosion was proposed [41]. Initially, a molten eutectic phase is formed at the alloy surface as a result of the sulfation of transient NiO or Co_3O_4. High SO_2 and S_2 potentials are achieved at the scale/salt interface due to the low

oxygen potential in this region. For the Co-Cr-Al alloys, the following acidic fluxing reaction occurs at the scale/salt interface:

$$Al_2O_3 + 3SO_2 = Al_2(SO_3)_3 \quad (37)$$

The aluminum sulfite diffuses out into the salt and reprecipitates as nonprotective Al_2O_3 at regions of higher p_{O_2}. Cr either experiences an analogous reaction or oxidizes *in situ*. The base metal dissolves in the acidic salt, diffuses out to the salt gas interface, and precipitates as Co_3O_4. Note that this mechanism is consistent with the preferential attack of the Al-rich β phase. For Ni-Cr-Al alloys, the important reaction at the salt/alloy interface is the sulfidation of Al and Cr, and the subsequent oxidation of these sulfides, as evidenced by the presence of numerous internal sulfides in these alloys. The S_2 released from the oxidation of these phases is apparently enough to form NiS, which can dissolve in the salt, allowing Ni to diffuse to the surface and form NiO.

The work of Barkalow and Goward [40] is significant in that it is among the first and only studies which aim to carefully document the Type II hot corrosion morphology of NiCoCrAlY alloys. It was found that a NiCoCrAlY (23Co-18Cr-12Al) experienced a more general surface consumption as opposed to the pitting typically observed in NiCrAlY and CoCrAlY alloys. A large Al-depletion layer existed over much of the surface, and sulfidation was much more severe in this alloy than in NiCrAlY, in which some internal sulfide formation was observed. In regions where there was no depletion layer, a mixture of metal and metal sulfide remained in the corrosion product.

3.0 RESEARCH OBJECTIVES

Various coating materials have been developed which are quite resistant to certain forms of attack, e.g. simple oxidation, Type I hot corrosion, etc., but are highly susceptible to others. It would be of obvious practical value to develop a single coating which can adequately resist a number of different conditions commonly encountered in gas turbine engines. The first goal of this research was to work towards the development of a coating with substantial resistance to several different types of degradation, namely cyclic oxidation, Type I hot corrosion, combined cyclic oxidation and Type I hot corrosion, and Type II hot corrosion. This was accomplished by first evaluating the performance of a number of different materials under these conditions in order to ascertain the important compositional factors. Based on these results, an appropriate candidate material was chosen for further study. Finally, the composition of this material was adjusted in order to optimize its oxidation and corrosion resistance.

Many studies have been conducted over the past four decades in an attempt to understand the mechanisms of hot corrosion and the factors that influence the corrosion process. However, no comprehensive study has been done to date to elucidate the microstructural and compositional factors which most strongly affect the hot corrosion of state of the art coating materials. In particular, very little emphasis has been placed on the effect of phase constitution on degradation behavior. Therefore, the second goal of the current research was to establish clear relationships between the microstructure and composition of various overlay coatings and their hot corrosion behavior.

4.0 EXPERIMENTAL PROCEDURE

4.1 MATERIAL PREPARATION

The nominal compositions of the alloys used in this study can be found in Table 2.

Table 2. Nominal alloy compositions

	Ni	Co	Cr	Al	Y	Hf	Si
NiCrAlY	Balance	-	31.00	11.25	0.65	-	-
CoCrAlY	-	Balance	23.00	13.00	0.65	-	-
NiCoCrAlY	Balance	20.00	18.00	12.50	0.60	0.40	0.25
NiCoCrAlY-2	Balance	10.00	18.00	12.50	0.60	0.40	0.25
NiCoCrAlY-3	Balance	10.00	27.10	12.50	0.60	0.40	0.25

All alloys were prepared by the Materials Preparation Center at Ames Laboratory, Ames, IA. They were received as drop-cast bars which were homogenized at 1000°C for 24 hours in Ar, and were tested in this condition unless otherwise noted. The bars were cut into coupon specimens approximately 3mm thick and 18mm in diameter, polished to a 3µm diamond finish, cleaned in soap and water, degreased in acetone, weighed, and dried immediately prior to testing. 3mm diameter injection cast pins of the NiCrAlY composition were also tested under selected conditions. The surface preparation was the same as that mentioned above for the injection cast materials.

A 2-3mg/cm^2 deposit of Na_2SO_4 was applied to the surface of the hot corrosion specimens by heating with a heat gun in an alumina tray to approximately 200°C and spraying with a saturated solution of laboratory grade anhydrous Na_2SO_4 in distilled water. Samples were weighed periodically to ensure that the proper amount of salt was deposited.

4.2 HIGH TEMPERATURE EXPOSURES

4.2.1 Cyclic Oxidation

Cyclic oxidation exposures were carried out in a CM bottom-loading furnace, shown schematically in Figure 9:

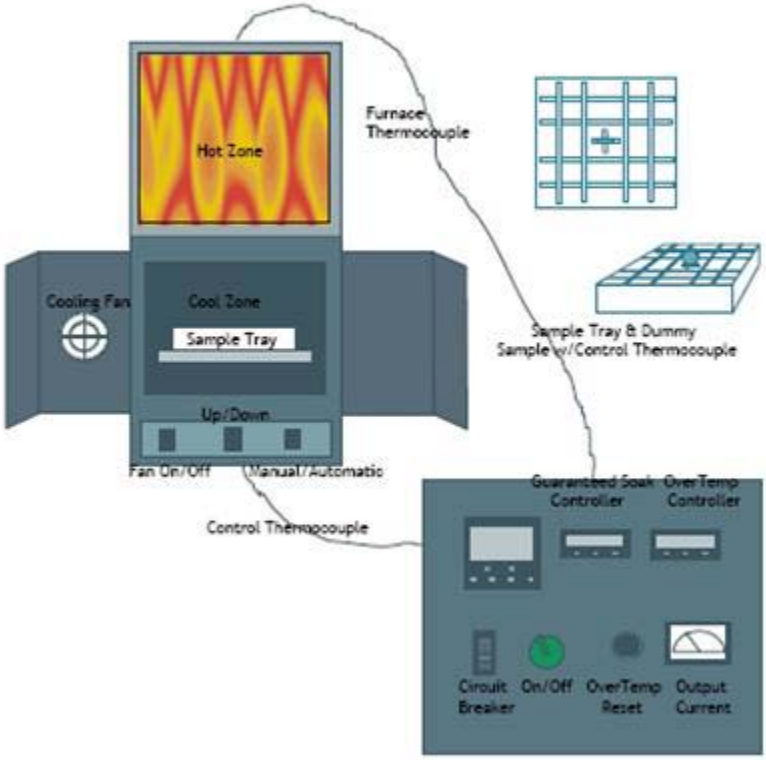

Figure 9. Schematic representation of bottom-loading furnace

Each cycle consisted of a 10 minute heating to 1100°C followed by a 45 minute hold. After the isothermal hold, the specimens were lowered into the cool zone where they were blown with laboratory air for 10 minutes, cooling them to approximately 150°C. This cycle was typically repeated 20 times in between weight change measurements and sample observation. Weight changes were measured using a Mettler Toledo AG135 analytical balance with a precision of 10 μg.

4.2.2 Type I Hot Corrosion

Immediately following salt deposition, Type I hot corrosion exposures were carried out at 900°C in a vertical resistance-heated tube furnace, shown schematically in Figure 10:

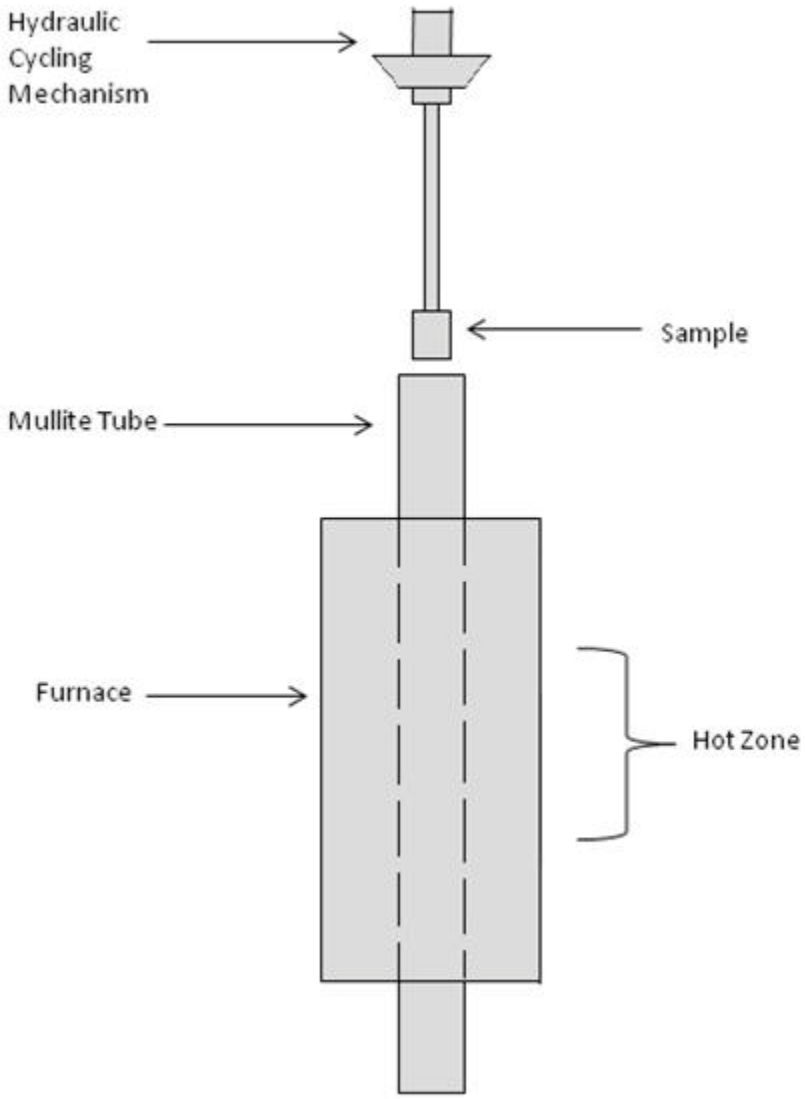

Figure 10. Schematic representation of Type I hot corrosion furnace

The specimen sits in an alumina crucible which is suspended from a rod connected to a hydraulic cycling mechanism. This mechanism basically consists of a cylinder and piston powered by compressed air. A ChronTrol XT table top timer was programmed such that the specimens were cycled into the hot zone of the furnace, which was maintained at 900°C ± 3°C, held there for 20 hours, and then automatically moved into the cool zone of the furnace which was maintained at ~100°C. After cooling every 20 hours, the specimens were washed ultrasonically in soap and water, weighed, and deposited with 2-3 mg/cm^2 of Na_2SO_4 prior to another 20 hours of hot time.

4.2.3 Type II Hot Corrosion

Immediately following salt deposition, Type II hot corrosion exposures were carried out at 700°C in a horizontal resistance-heated tube furnace, shown schematically in Figure 11:

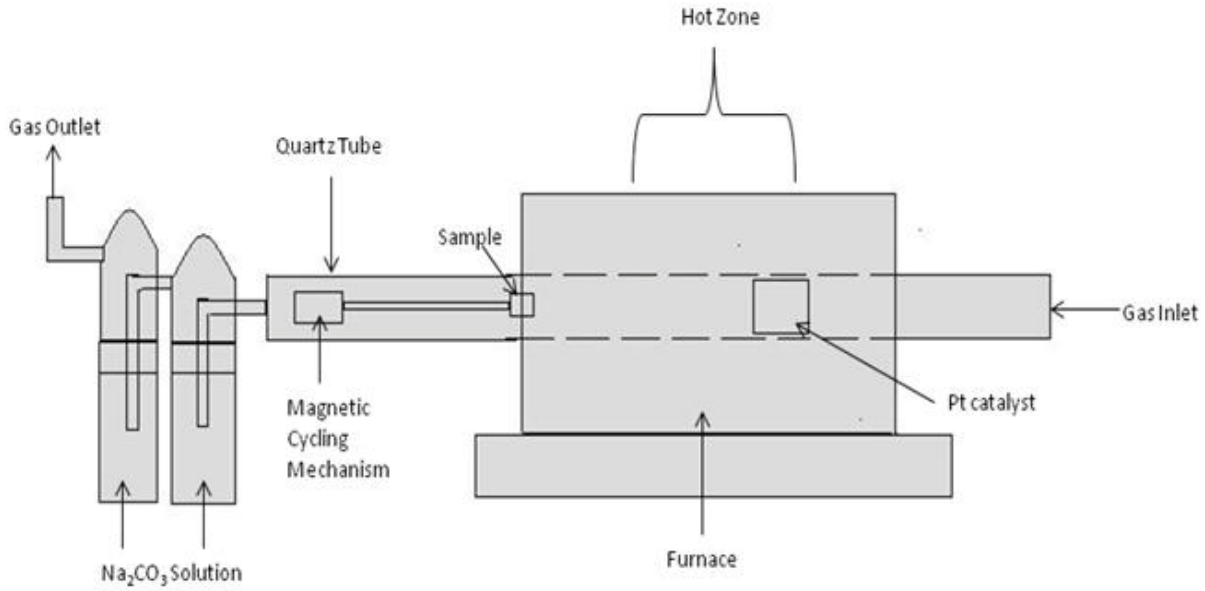

Figure 11. Schematic representation of Type II hot corrosion furnace

This furnace is cycled manually by using a magnet to push the rod from which the specimen hangs into the furnace until the specimen is in the hot zone, which was maintained at 700°C ± 3°C. A gas containing O_2 + 1000ppm SO_2 flowed into the tube at a constant flow rate. This gas mixture was passed over a platinum honeycomb catalyst which was placed in the hot zone in order to establish an equilibrium p_{SO_3} in the atmosphere according to Reaction 32. Assuming thermodynamic equilibrium, the p_{SO_3} under these conditions is 4 x 10^{-4} atm. The specimens were cycled into the hot zone where they were exposed isothermally for 10 hours, after which they were removed from the furnace and allowed to cool to ~100°C in the cool zone. After exposure, specimens were metallographically prepared in the absence of water and water-based solutions in order to preserve the soluble corrosion products which form during Type II hot corrosion.

Upon exiting the furnace, the gases were bubbled through a solution of Na_2CO_3 in water prior to being released into a fume hood. The purpose of this step was to remove SO_3 from the gas according to Reaction 38:

$$SO_3 + Na_2CO_3 = Na_2SO_4 + CO_2 \quad (38)$$

Sodium sulfate is precipitated out in the bubblers and the majority species exiting the apparatus are O_2 and CO_2.

4.2.4 Intermittent Hot Corrosion / Cyclic Oxidation

Intermittent hot corrosion exposures involved a combination of the procedures described in sections 4.2.1 and 4.2.2. For these experiments, samples were exposed to 20 hours of Type I hot corrosion conditions, cleaned ultrasonically in soap and water, weighed, and then cyclically oxidized for 100 cycles following the previously-described procedure.

4.3 ANALYTICAL

Analysis of as-received and exposed specimens was achieved primarily by the use of kinetic plots (weight change vs. time), scanning electron microscopy (SEM), and in some cases X-ray diffraction (XRD). The SEM used in this work was a Philips XL-30 Field Emission Gun microscope. This microscope is equipped with secondary electron (SE), backscatter electron (BSE), and X-ray detectors and is thus capable of performing image acquisition and energy dispersive spectroscopic analysis (EDS). A Philips X'Pert diffractometer was used for XRD analysis.

5.0 RESULTS AND DISCUSSION

5.1 AS-RECEIVED MICROSTRUCTURES

5.1.1 NiCrAlY

5.1.1.1 Drop Cast

Representative BSE micrographs showing the microstructure of the drop cast (DC) NiCrAlY alloy following casting and homogenization are shown in Figure 12:

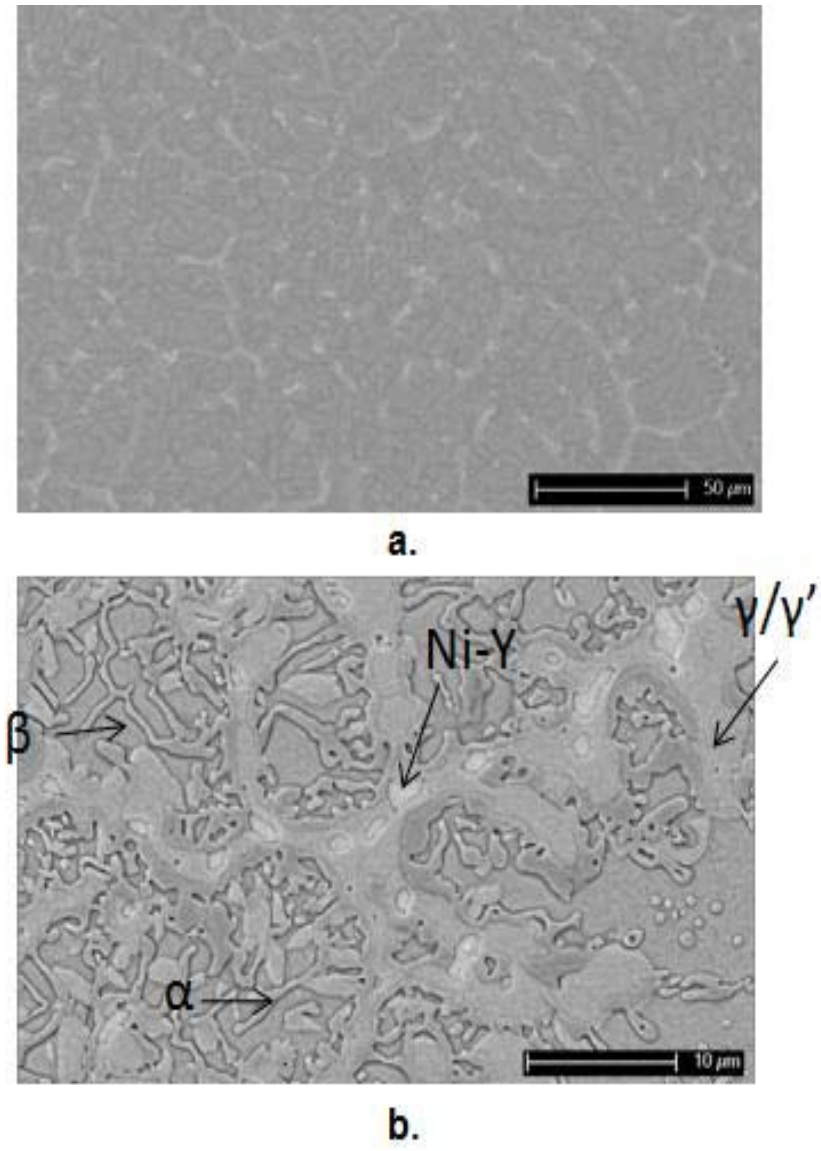

Figure 12. DC NiCrAlY, as-received

A four-phase microstructure is observed, consisting of β-NiAl (primitive cubic intermetallic), γ (FCC Ni-base solid solution) and/or γ′-Ni_3Al (primitive cubic intermetallic), α (BCC Cr-base solid solution), and a Ni-rich yttride phase. The presence of γ and/or γ′ in this alloy at the temperature of the homogenizing heat treatment will be explained in more detail subsequently.

5.1.1.2 Injection Cast

Representative BSE micrographs showing the microstructure of the injection cast (IC) NiCrAlY alloy are shown in Figure 13. Regions of the cylindrical pin close to the edge and towards the center of the cross section are shown.

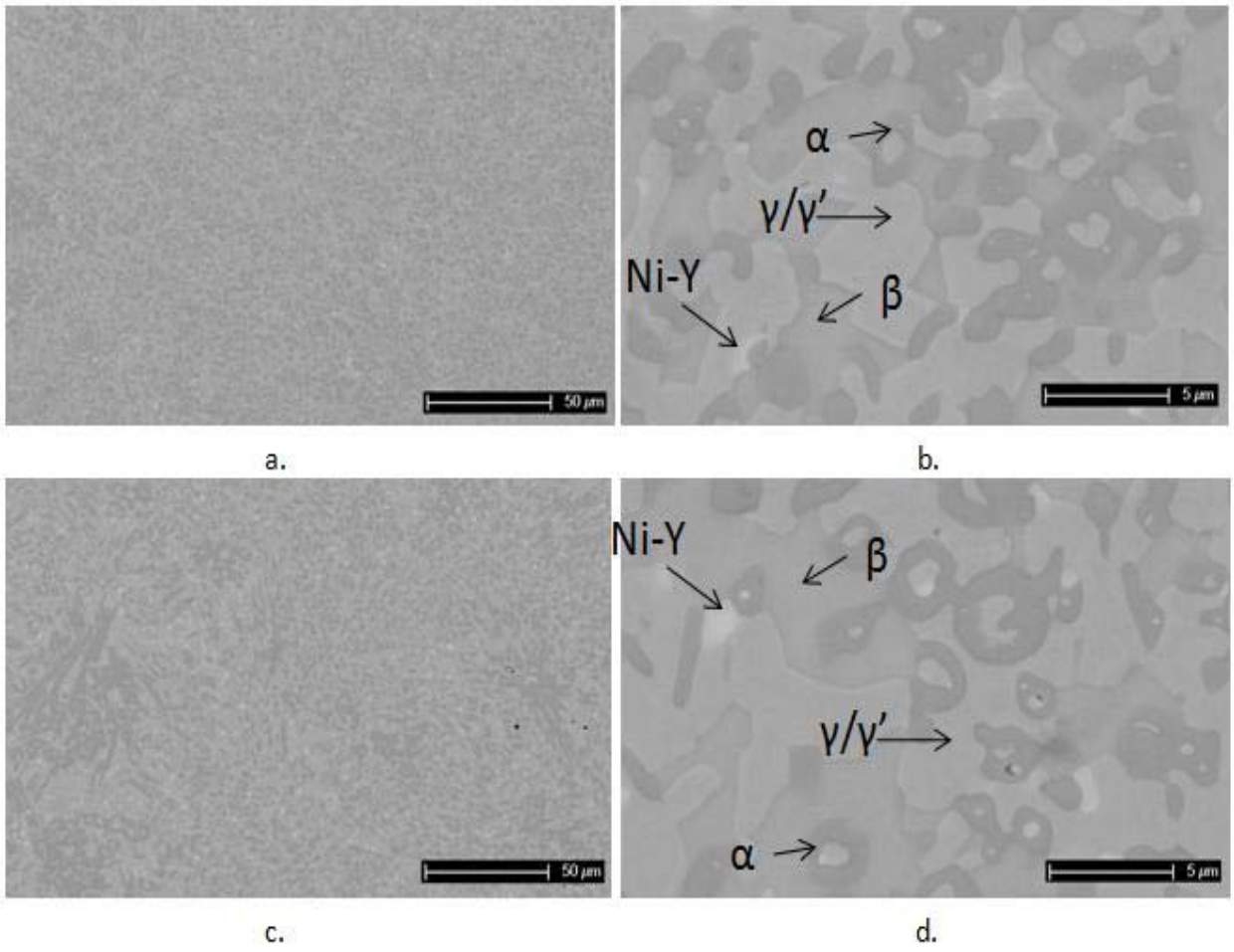

Figure 13. IC NiCrAlY, as-received: (a,b) edge of specimen, (c,d) center of specimen

A four phase microstructure is observed, consisting of γ-Ni solid solution, β-NiAl, α-Cr solid solution, and a Ni-rich yttride phase. Some coarsening of the microstructure occurs toward the center of the casting during solidification. Nonetheless, comparison of Figure 12 and Figure 13 clearly demonstrates the refined microstructure achieved by the injection casting process.

5.1.2 CoCrAlY

Representative BSE micrographs showing the microstructure of the CoCrAlY alloy following casting and homogenization are shown in Figure 14:

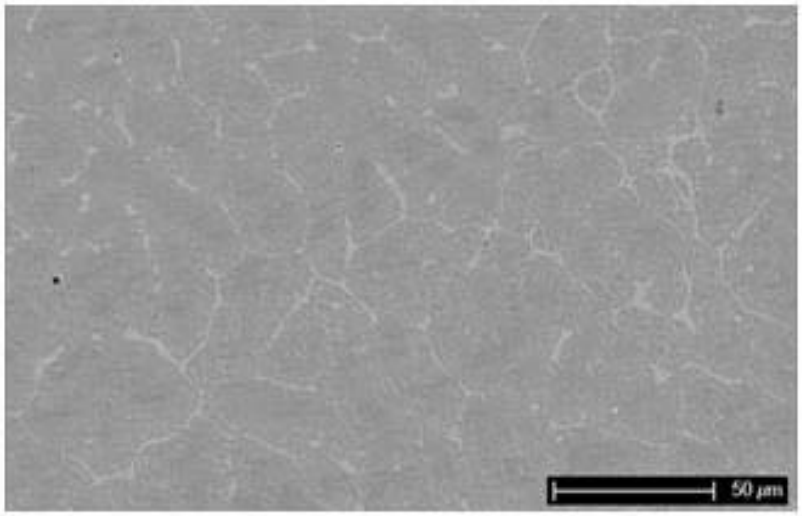

a.

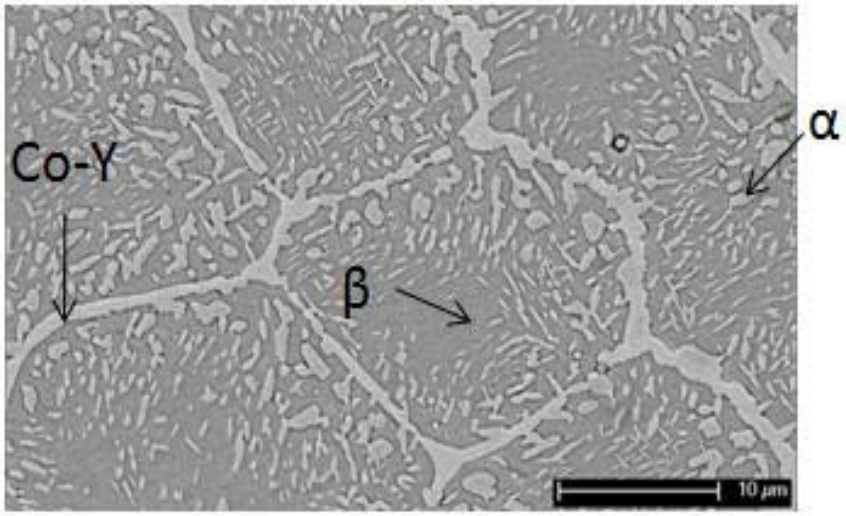

b.

Figure 14. DC CoCrAlY, as-received

A three-phase microstructure is observed, consisting of β-CoAl (primitive cubic intermetallic), α (hexagonal Co-base solid solution), and a Co-rich yttride phase.

5.1.3 NiCoCrAlY

5.1.3.1 Drop Cast

Representative BSE micrographs showing the microstructure of the DC NiCoCrAlY alloy following casting and homogenization are shown in Figure 15:

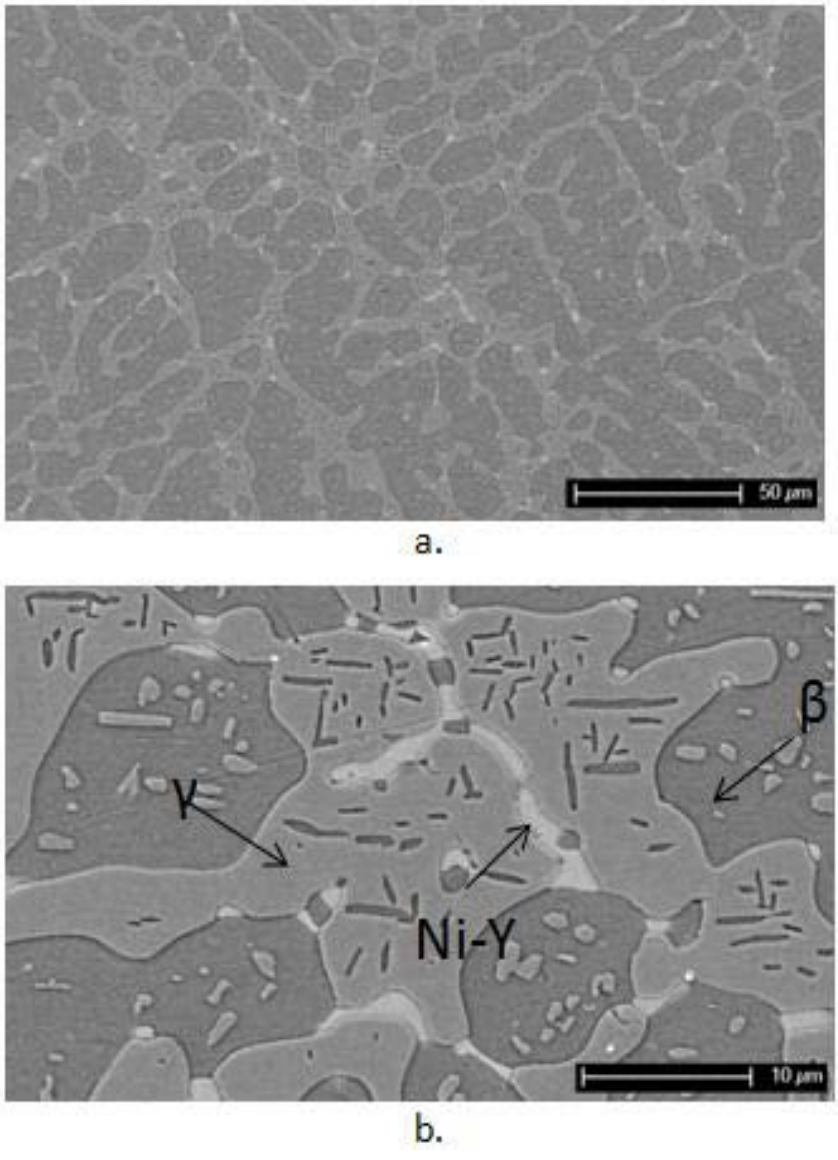

Figure 15. DC NiCoCrAlY, as-received

A three-phase microstructure is observed, consisting of β-NiAl, γ-Ni solid solution, and a Ni-rich yttride phase.

5.1.4 NiCoCrAlY-2

Representative BSE micrographs showing the microstructure of the NiCoCrAlY-2 alloy following casting and homogenization are shown in Figure 16:

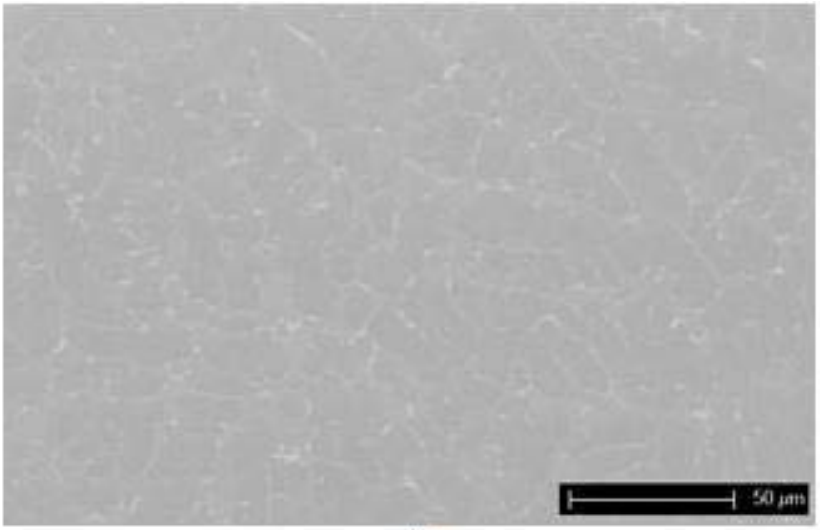

a.

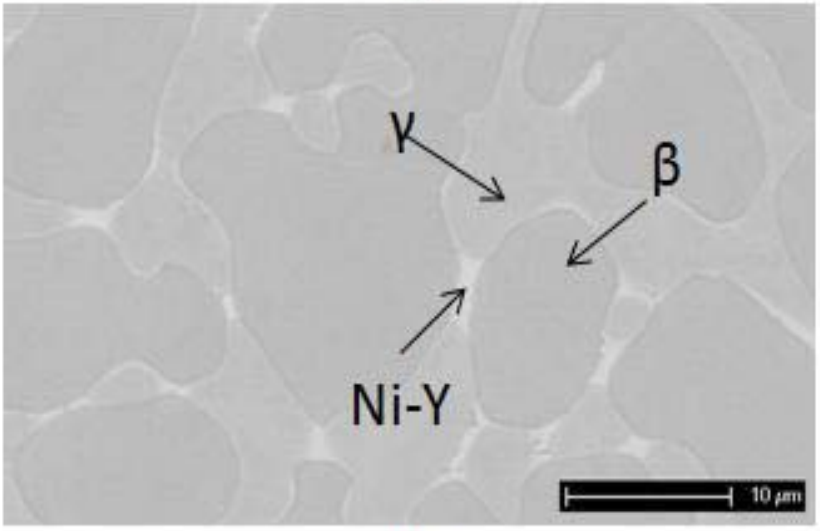

b.

Figure 16. DC NiCoCrAlY-2, as-received

A three-phase microstructure is observed, consisting of β-NiAl, γ-Ni solid solution, and a Ni-rich yttride phase.

5.1.5 NiCoCrAlY-3

Representative BSE micrographs showing the microstructure of the NiCoCrAlY-3 alloy following casting and homogenization are shown in Figure 17:

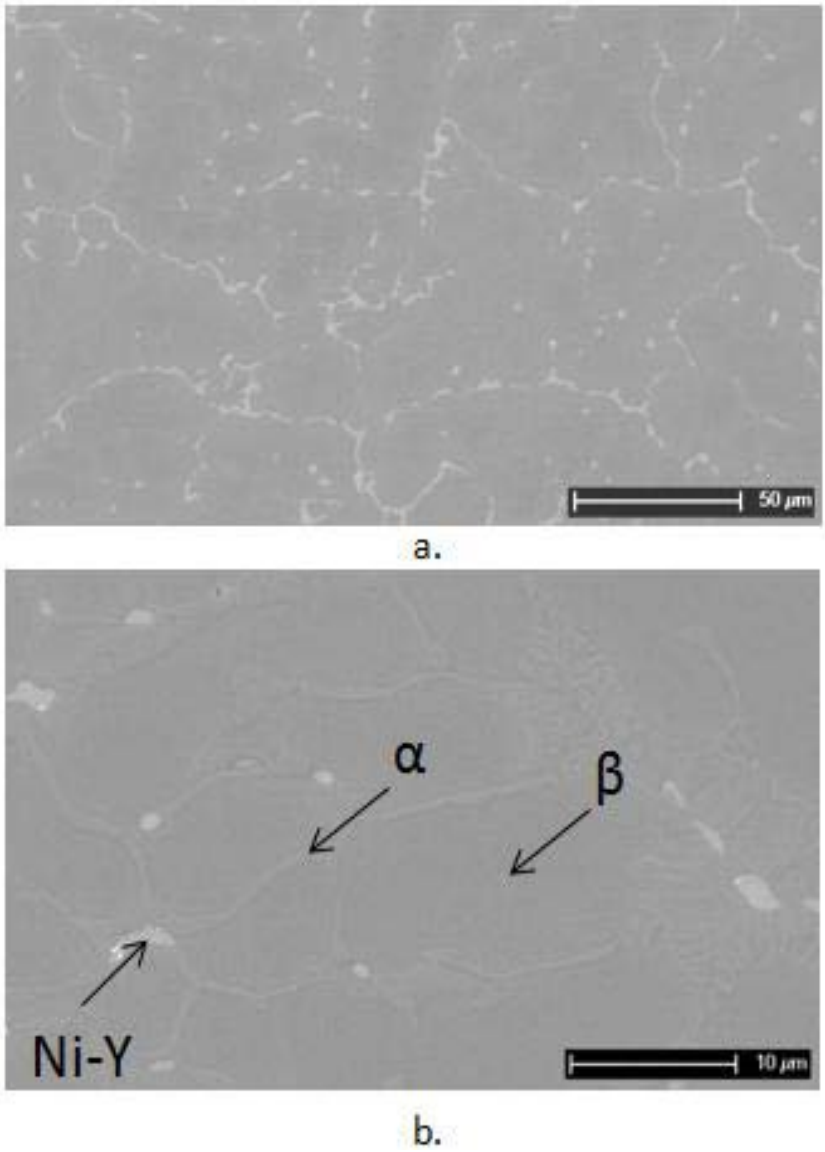

Figure 17. DC NiCoCrAlY-3, as-received

A three-phase microstructure is observed, consisting of β-NiAl, α-Cr solid solution, and a Ni-rich yttride phase.

5.2 HOT CORROSION AND OXIDATION OF DROP CAST NiCrAlY, CoCrAlY, and NiCoCrAlY

5.2.1 Type I Hot Corrosion of Drop Cast NiCrAlY, CoCrAlY, and NiCoCrAlY

Type I hot corrosion exposures of the NiCrAlY, CoCrAlY, and NiCoCrAlY alloys were carried out for up to 1040 hours. Kinetic plots of the weight change per unit area vs. time for these three specimens are shown in Figure 18.

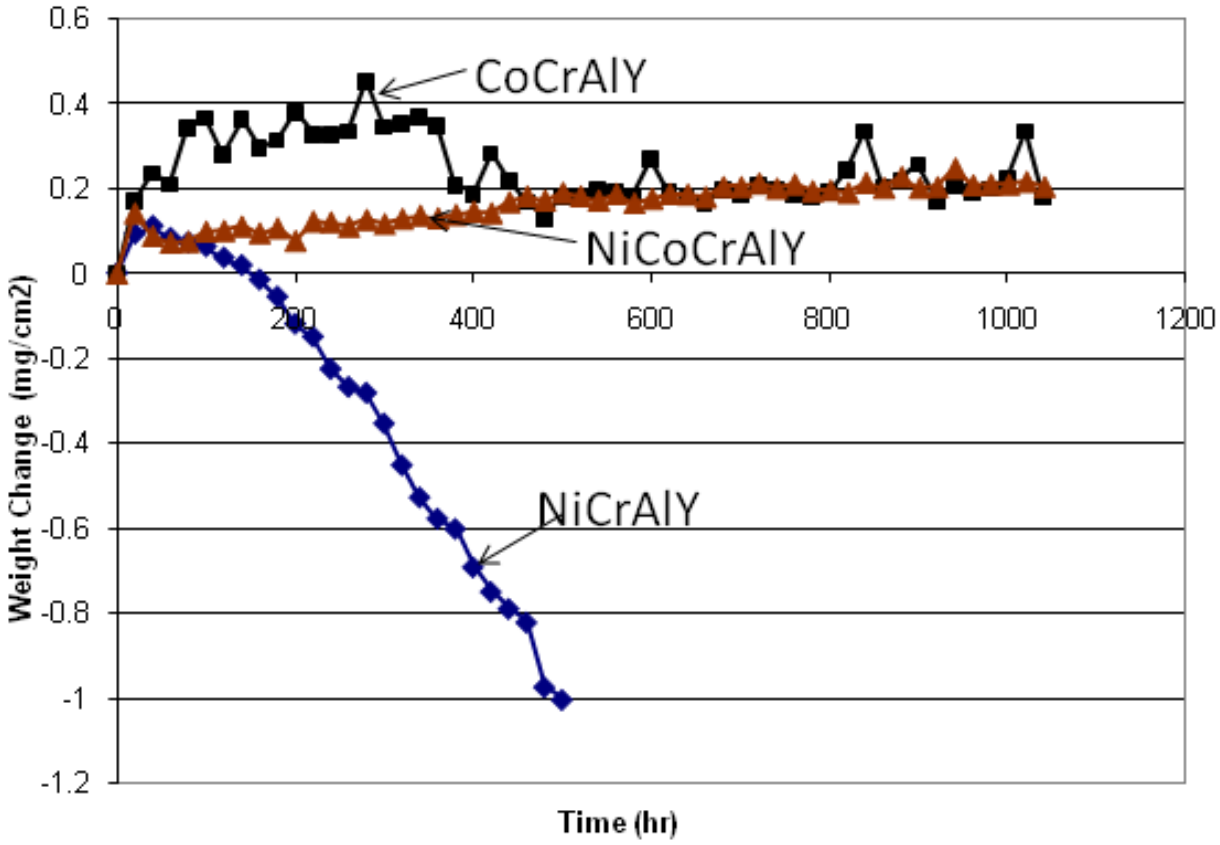

Figure 18. Weight change vs. time: NiCrAlY, CoCrAlY, NiCoCrAlY, Type I hot corrosion

The NiCoCrAlY and CoCrAlY specimens exhibited small, positive weight changes which were sustained up to 1040 hours, when the tests were terminated. Conversely, the NiCrAlY specimen exhibited a smooth, roughly linear decrease in mass, beginning after approximately 100 hours of exposure. Typically, mass loss is indicative of scale spallation, however in this case washing away of dissolved chromate ions prior to measuring the mass of the specimen is likely the cause of the observed negative weight changes. Scale spallation commonly results in weight change curves which show rapid, sharp mass losses, whereas the NiCrAlY curve in Figure 18 changes much more gently. Also, the wash water from the NiCrAlY specimen was consistently yellow, which is indicative of the presence of CrO_4^{2-} ions. It appears that Cr_2O_3 dissolves into the melt as chromate ions according to Reaction 23, and this reaction product is washed away during cleaning in between 20 hour cycles.

Figure 19 shows cross sectional BSE micrographs from these specimens. The NiCrAlY was exposed for 500 hours prior to sectioning, and the NiCoCrAlY and CoCrAlY were exposedfor 1040 hours.

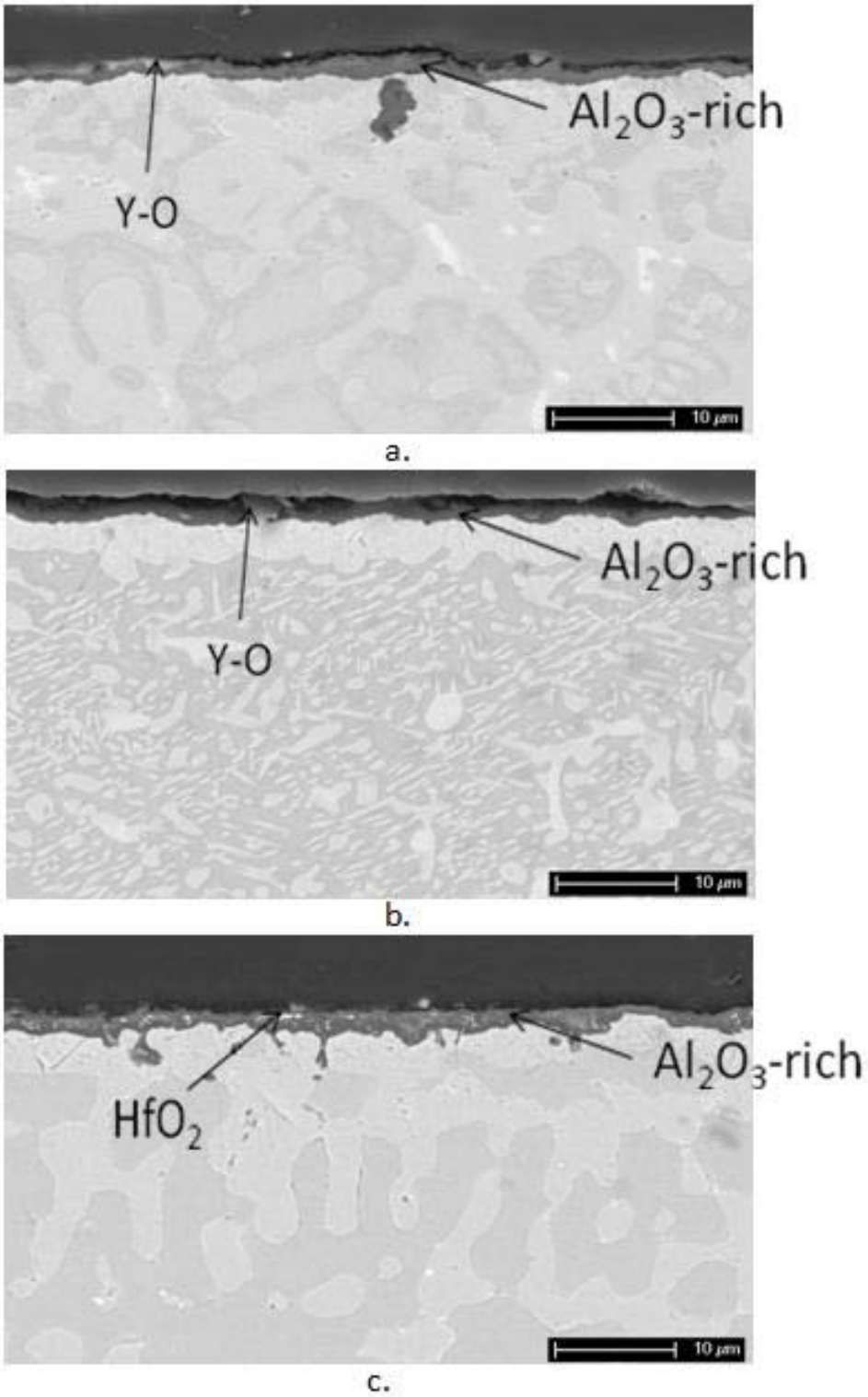

Figure 19. Type I hot corrosion microstructures: a.) NiCrAlY, b.) CoCrAlY, c.) NiCoCrAlY

All specimens have a relatively thin, planar surface oxide which is rich in α-Al_2O_3. XRD also revealed the presence of Cr_2O_3 on the NiCrAlY, $CoAl_2O_4$ spinel on the CoCrAlY, and $CoAl_2O_4$/$NiAl_2O_4$ spinel on the NiCoCrAlY. Yttrium-rich oxides were found on the surfaces of all specimens, as indicated in Figure 19 a and b. HfO_2 can also be found in the scale on the NiCoCrAlY specimen, which likely formed as a result of the exchange reaction:

$$3\underline{Hf} + 2Al_2O_3 = 3HfO_2 + 4\underline{Al} \quad (40)$$

which has a ΔG^o value of -98kJ at 900°C. A subsurface layer of β-phase depletion, resulting from Al consumption during oxidation, is observed only in the CoCrAlY and NiCoCrAlY specimens. Metal recession is occurring rapidly enough in the NiCrAlY to outpace the diffusional processes required for Al to be transported from the β phase to the surface, which is consistent with the weight losses observed for this specimen. Therefore, such a depletion layer is not seen in the NiCrAlY. No cracking or other evidence of spallation is observed in the oxide scale in Figure 19a, further supporting the assertion that negative weight changes are not occurring as a result of scale spallation.

The Type I hot corrosion of all specimens is nearly negligible. As mentioned, these tests were stopped after no longer than 1040 hours; it is expected that given sufficient time, all alloys would enter the propagation stage and severe degradation would occur [6]. To demonstrate by comparison the strong resistance of these alloys to Type I degradation, a micrograph showing a Ni-8Cr-6Al alloy after 120 hours of Type I hot corrosion exposure is presented in Figure 20:

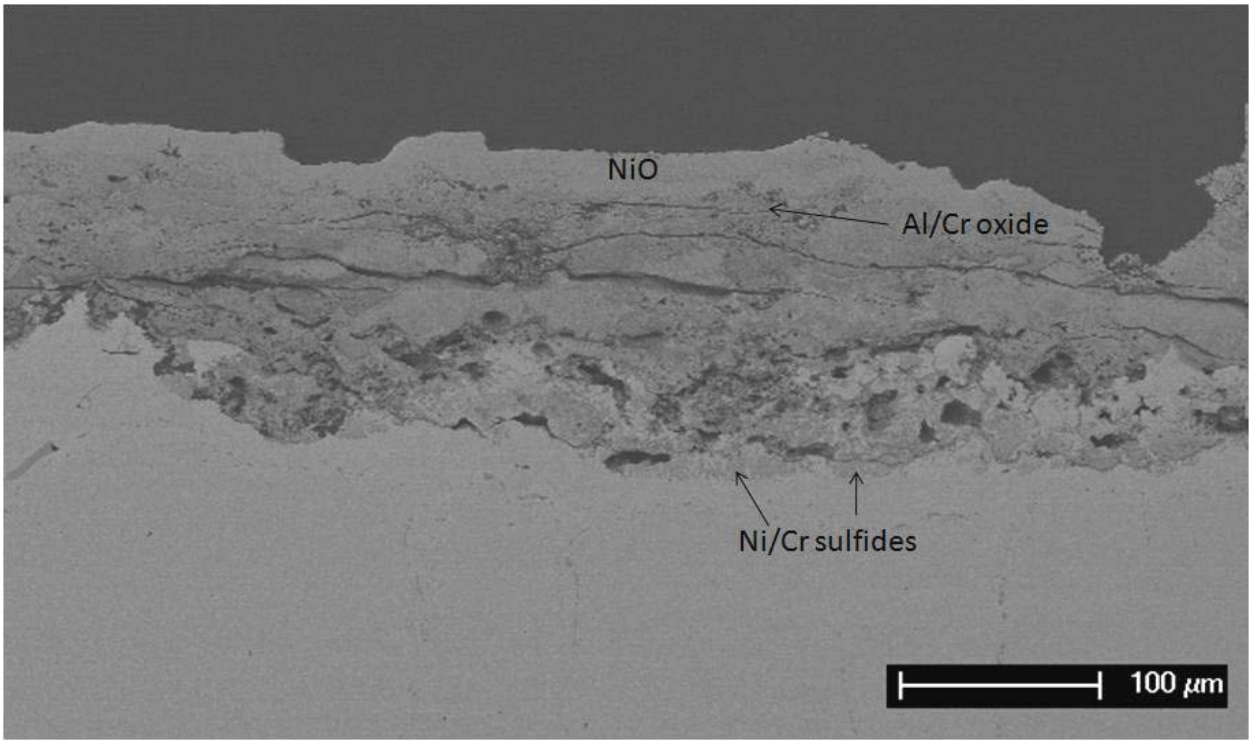

Figure 20. Type I hot corrosionmicrostructure: Ni-8Cr-6Al

A rather non-protective corrosion product is observed to form on this alloy, consisting of a voluminous NiO with interspersed Al/Cr-rich oxides. A layer of internal sulfides is observed in advance of the corrosion front. The weight change as a function of time for this specimen was presented in Figure 1. This plot shows rather large amounts of spallation after 120 hours of exposure. Clearly, this form of hot corrosion can be quite severe; the NiCrAlY, CoCrAlY, and the NiCoCrAlY are not particularly susceptible to this attack over the range of exposure times studied.

5.2.2 Type II Hot Corrosion of Drop Cast NiCrAlY, CoCrAlY, and NiCoCrAlY

Type II hot corrosion exposures of the NiCrAlY, CoCrAlY, and NiCoCrAlY alloys were carried out for 10 hours. Kinetic plots of the weight change per unit area vs. time can be very difficult to accurately interpret for this kind of attack, and therefore microstructural analysis was heavily relied upon. Cross-sectional microstructures of these alloys after Type II exposure are presented in Figure 21.

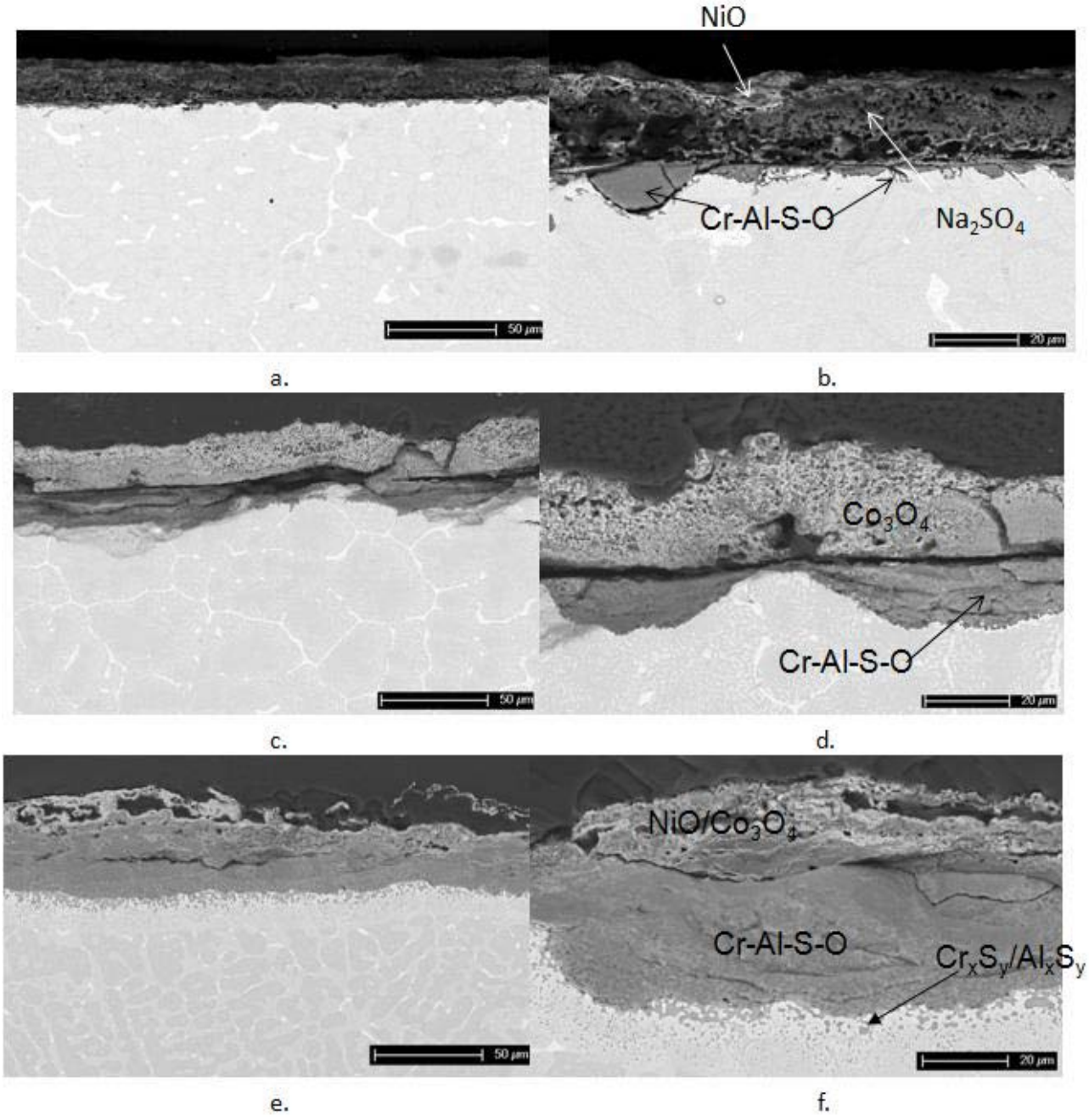

Figure 21. Type II hot corrosion microstructures: a,b.) NiCrAlY, c,d) CoCrAlY, e,f) NiCoCrAlY

The NiCrAlY was corroded the least out of the three alloys. A solidified Na_2SO_4 layer can be observed on the surface of the specimen with some NiO precipitating out near the salt/gas interface. Some relatively small corrosion pits, rich in Cr, Al, S, and O, are found in the specimen. However, these are very shallow compared to those formed on the other MCrAlY alloys. Preferential oxidation/sulfidation attack is found to occur along phase boundaries surrounding the α phase. This is shown more clearly in Figure 22.

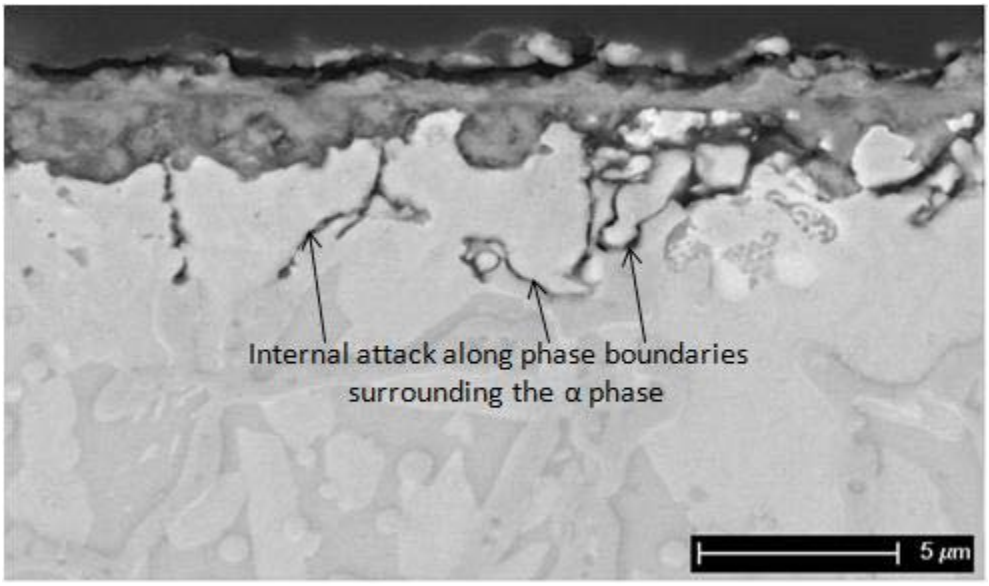

Figure 22. NiCrAlY Type II microstructure demonstrating interphase attack

In some cases this internal attack has consumed entire α grains. The phases present on the surface of the specimen were identified via XRD to be Na_2SO_4, NiO, Cr_2O_3, and possibly $NiCr_2O_4$ spinel. It is expected, based on EDS, that Al_2O_3 and/or $NiAl_2O_4$ are also present within the pit.

The attack of the CoCrAlY was consistent with the extensive literature on the Type II hot corrosion of Co-base alloys [37, 39-41, 43]. The specimen was severely pitted; the pits contained Cr, Al, S, and O, and Al and S were concentrated at the base of the pit. No distinct sulfide phases were detected within the pit or below it. At the surface, a rather thick (~30μm) oxide cap rich in Co was observed. The phases present on the surface of the specimen were identified via XRD to

be Co_3O_4, Cr_2O_3, and possibly $CoAl_2O_4$. Based on EDS, it is expected that Al_2O_3 is also present within the pit.

The NiCoCrAlY alloy displayed a pitting morphology similar to that seen on the CoCrAlY. However, often these pits were very broad and almost planar; they were not always extremely well defined as is commonly observed with CoCrAlY alloys (Figure 21c). The pits contained Cr, Al, S, and O, and a base metal oxide cap was observed above the pits. In some cases, these pits extended down to unaffected alloy, while in others an Al- depletion zone and/or Al and Cr sulfides were observed beneath the pit. A very distinct γ / β ghost microstructure existed within the pits in many regions of the specimen, as shown in Figure 23.

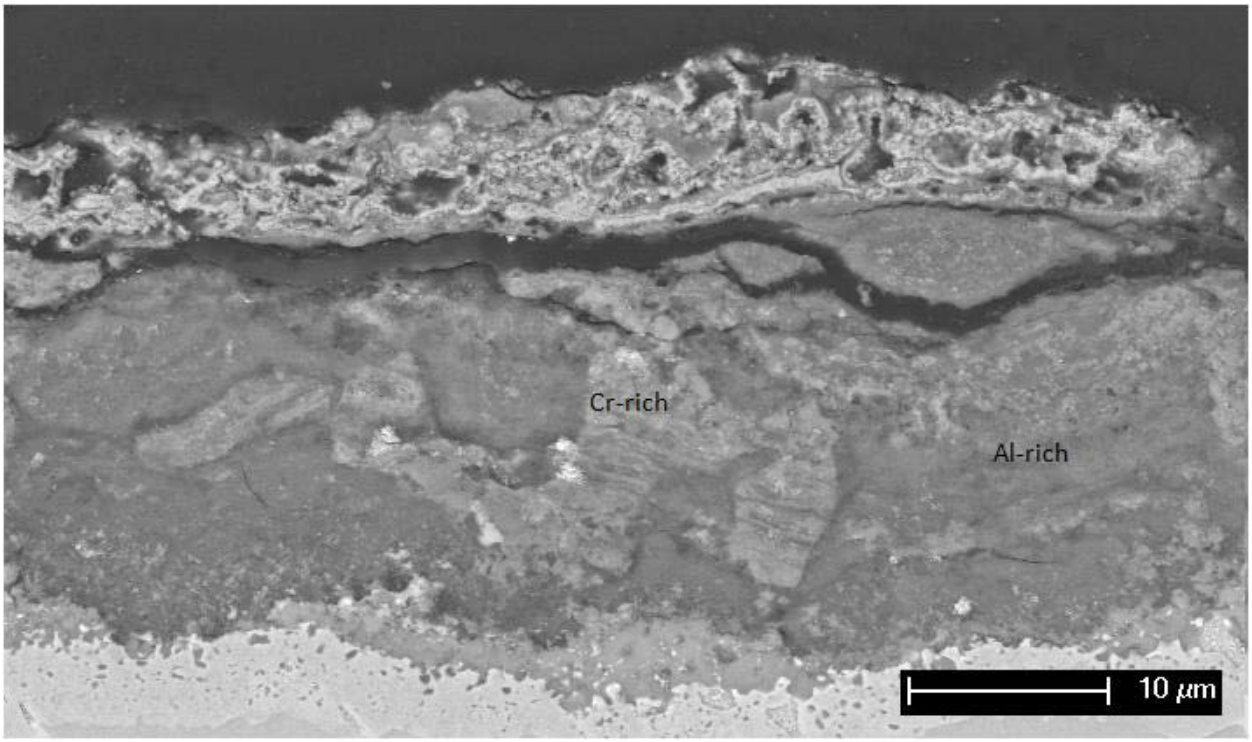

Figure 23. NiCoCrAlY Type II ghost microstructure

The regions corresponding to γ were rich in Cr, while those corresponding to β were Al-rich, indicating that the Al and Cr in these phases were indeed oxidized in situ as predicted by the Luthra mechanism [44]. The phases present on the surface of the specimen were identified via XRD to be Co_3O_4, NiO, and $CoAl_2O_4$. It is expected, based on EDS, that Al_2O_3 and/or Cr_2O_3 were also present within the pit.

X-ray maps from selected regions of the Type II specimens can be found in Figure 24, Figure 25, and **Figure 26**:

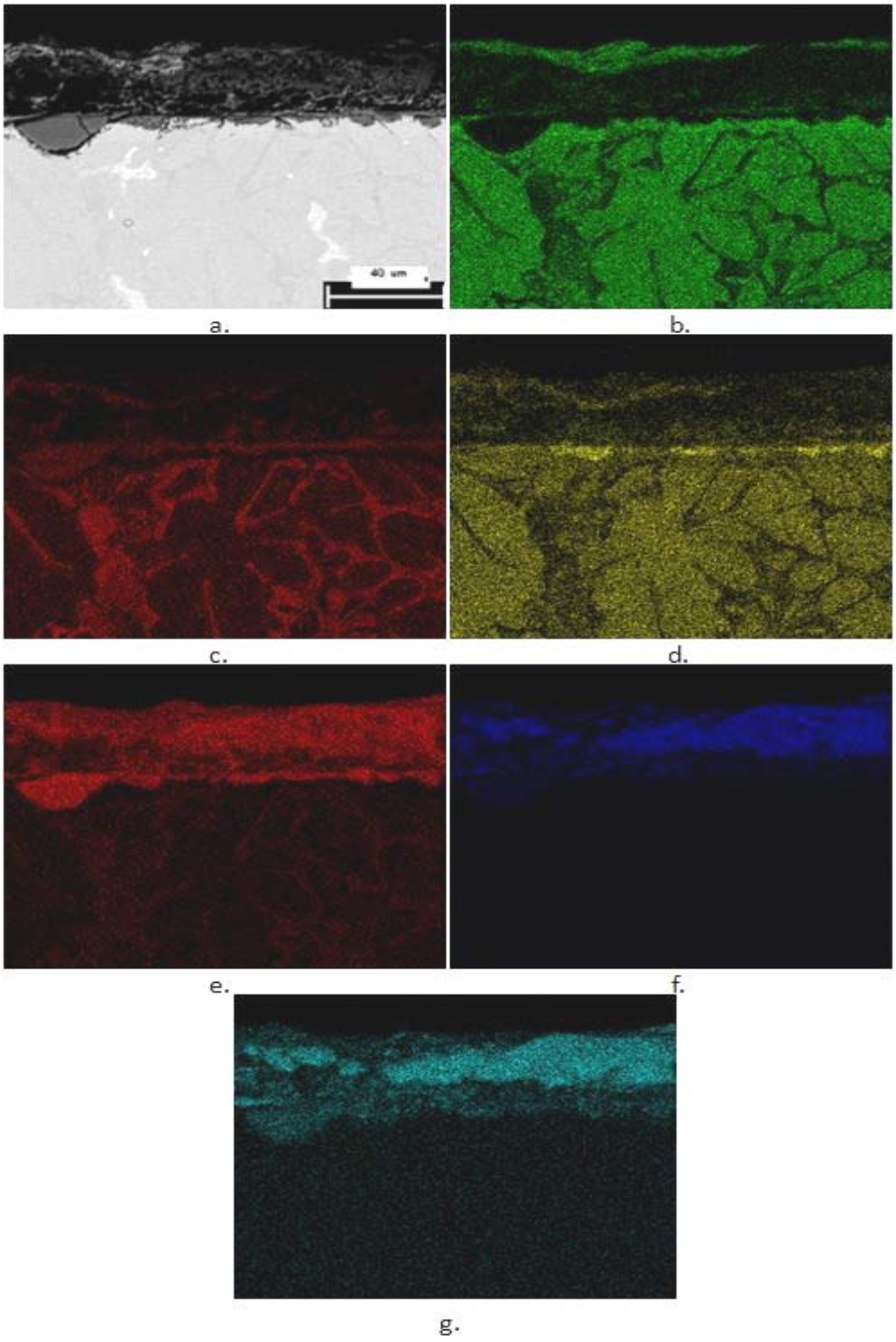

Figure 24. NiCrAlY Type II x-ray map: a.) BSEmicrograph, b.) Ni, c.) Cr, d.)Al, e.) O, f.) Na, g.) S

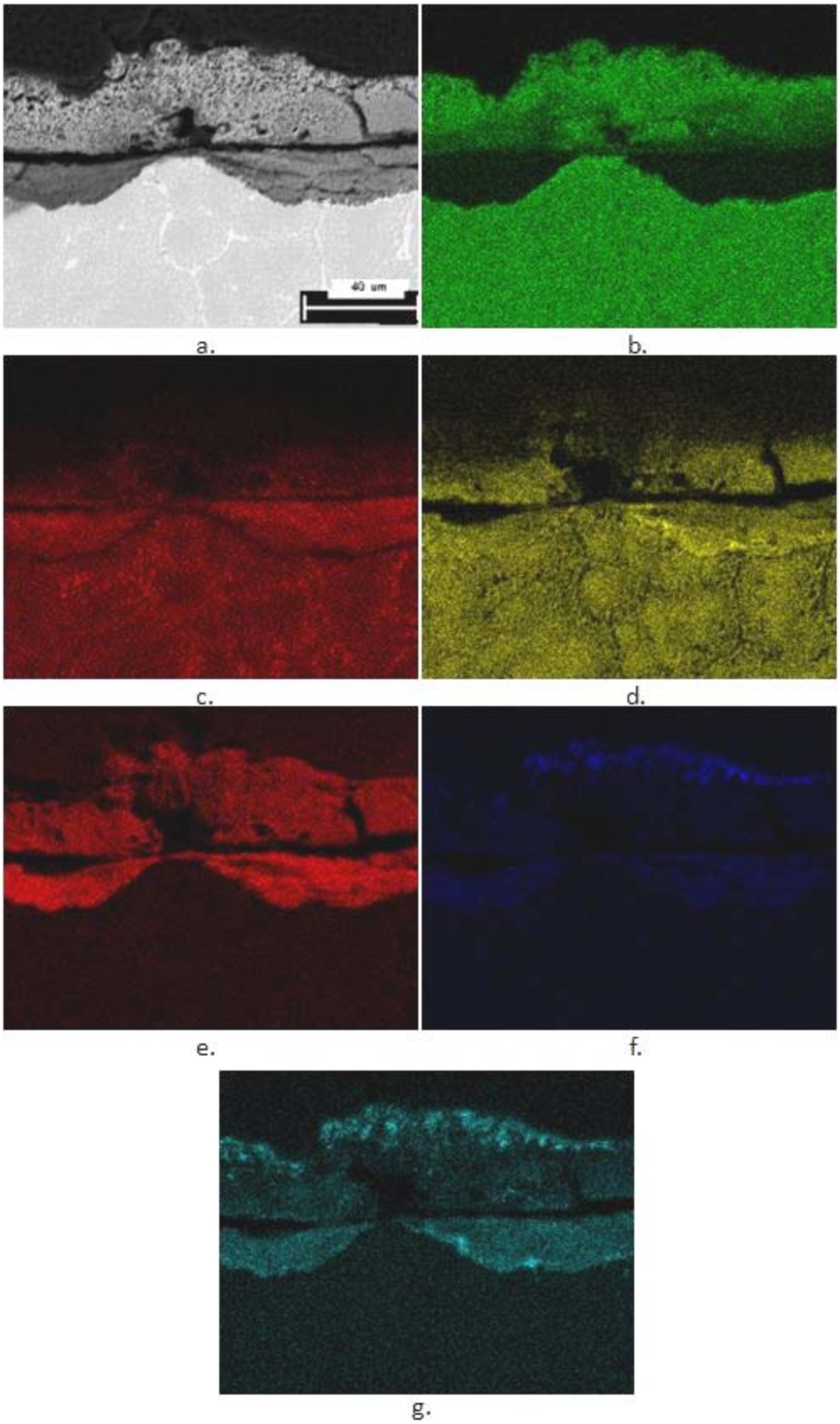

Figure 25. CoCrAlY Type II x-ray map: a.) BSEmicrograph, b.) Co, c.) Cr, d.)Al, e.) O, f.) Na, g.) S

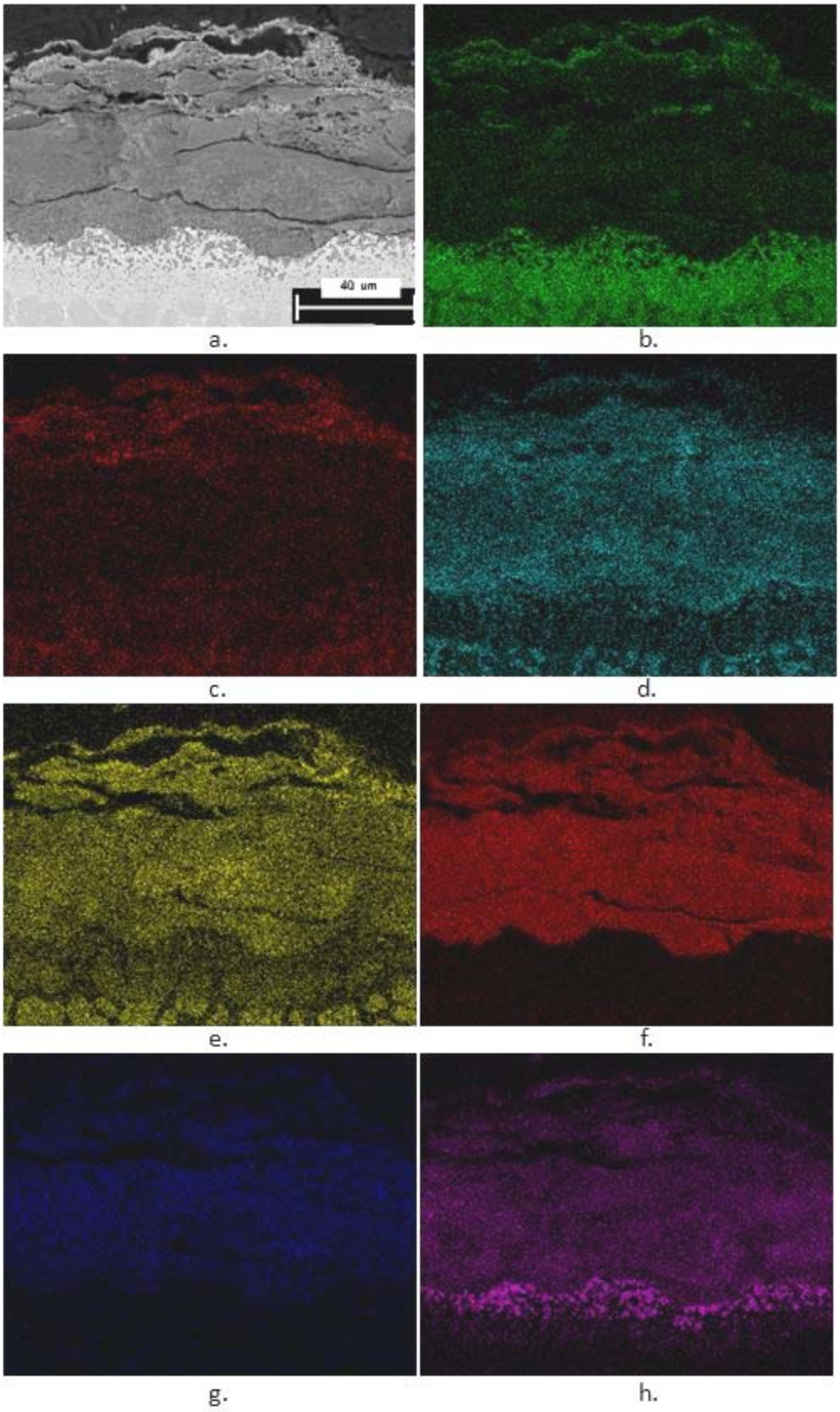

Figure 26. NiCoCrAlY Type II x-ray map: a.) BSEmicrograph, b.) Ni, c.) Co, d.) Cr, e.) Al, f.) O, g.) Na, h.) S

It is reasonable to conclude that the CoCrAlY specimen degraded under Type II conditions in a manner very similar to the many Co-base alloys that have been studied in the past. The degradation mechanisms proposed by Luthra [44] and Chiang et al [41] both seem to adequately explain the microstructural observations made in our laboratory and numerous others. Based on Figure 21 and Figure 25, CoCrAlY seems to have quite poor Type II hot corrosion resistance. It is to be noted that the pits observed on the CoCrAlY specimen were commonly deeper than those observed in Figure 25. Also, spallation of very thick corrosion products was often unavoidable during cooling.

As discussed previously, the hot corrosion of materials below the melting point of Na_2SO_4 is critically dependent on the formation of a low-melting point MSO_4-Na_2SO_4 eutectic. The relatively low resistance of the CoCrAlY to Type II degradation has been partially attributed to the greater stability of MSO_4 when M=Co compared to Ni [44-45]. Consider Reactions 31 and 41:

$$NiO + SO_3 = NiSO_4 \quad (41)$$

For Reaction 31, the formation of $CoSO_4$ from Co_3O_4, $\Delta G^o_{700^\circ C}$ = -59.3 kJ/mol $CoSO_4$, and for Reaction 41, $\Delta G^o_{700^\circ C}$ = -52.8 kJ/mol $NiSO_4$. Thus, indeed $CoSO_4$ is the more stable compound and can therefore form at a lower p_{SO_3}. In addition, the solubility of MSO_4 in Na_2SO_4 must be taken into account. Consider the $NiSO_4$-Na_2SO_4 binary phase diagram in Figure 27 [6]:

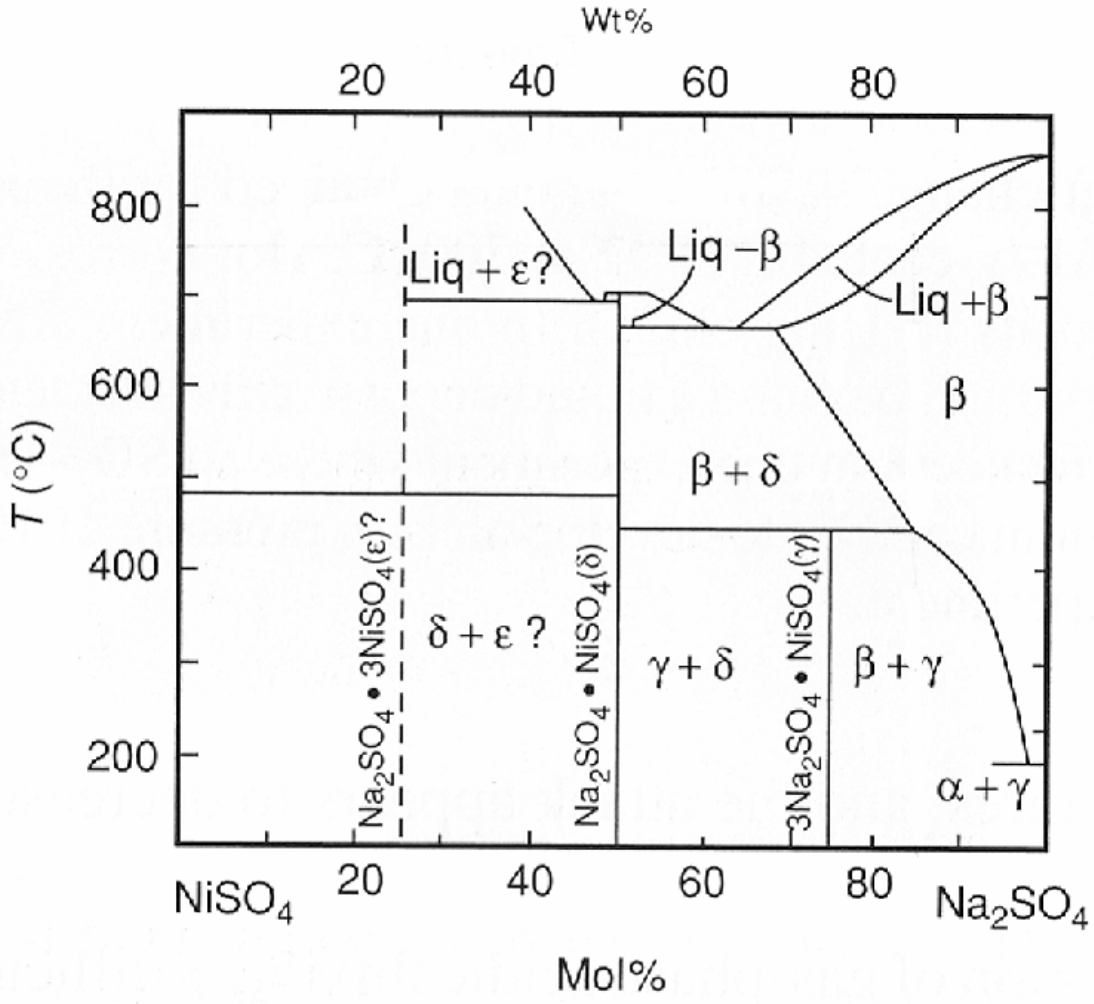

Figure 27. $NiSO_4$ - Na_2SO_4 phase diagram

At 700°C, Na_2SO_4 can dissolve approximately 22 mol% $NiSO_4$ before liquid formation would be expected. According to the $CoSO_4$-Na_2SO_4 phase diagram, Figure 7, only ~19 mol% $CoSO_4$ can be dissolved in Na_2SO_4 before liquid is formed. Therefore, the poor performance of cobalt-containing alloys in Type II hot corrosion can be attributed partly to the greater stability of both MSO_4 and the MSO_4-Na_2SO_4 liquid when M=Co.

5.2.3 Cyclic Oxidation and Intermittent Hot Corrosion of Drop Cast NiCrAlY, CoCrAlY, and NiCoCrAlY

The kinetic plots for the cyclic oxidation and intermittent hot corrosion of the drop cast MCrAlY alloys for up to 100 cycles of cyclic oxidation can be found in Figure 28. Note that the abscissa indicates the cyclic oxidation time, so that the intermittent hot corrosion specimens have already been exposed to 20 hr of Type I hot corrosion conditions at zero time on the plot.

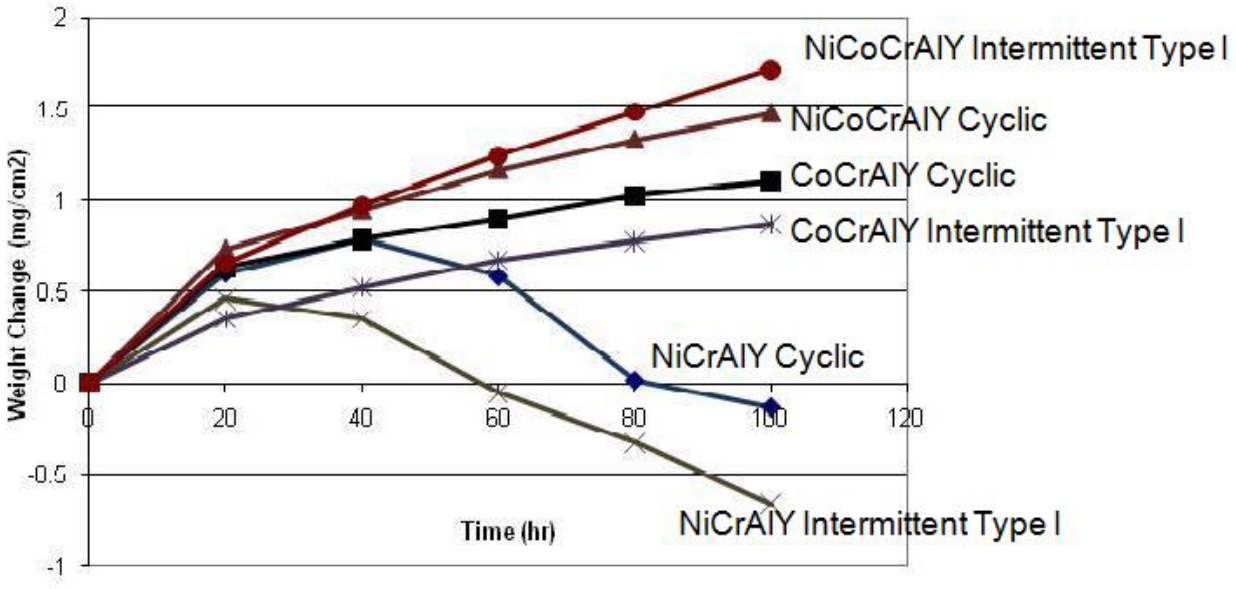

Figure 28. Weight change vs. time: NiCrAlY, CoCrAlY, NiCoCrAlY intermittent Type I and cyclic oxidation

A number of interesting observations can be made from this plot. Firstly, the NiCoCrAlY and the CoCrAlY alloys display parabolic kinetics, which would be expected for the growth of an α-Al_2O_3 scale at 1100°C. The NiCrAlY, however, performs very poorly and shows evidence of significant scale spallation after approximately 40 hours of oxidation. In addition, Figure 28 suggests that the initial Type I hot corrosion exposure had very little effect on the subsequent oxidation behavior of the MCrAlY alloys. Cross-sectional SEM micrographs of the MCrAlY alloys after cyclic oxidation and intermittent hot corrosion exposure can be found in Figure 29:

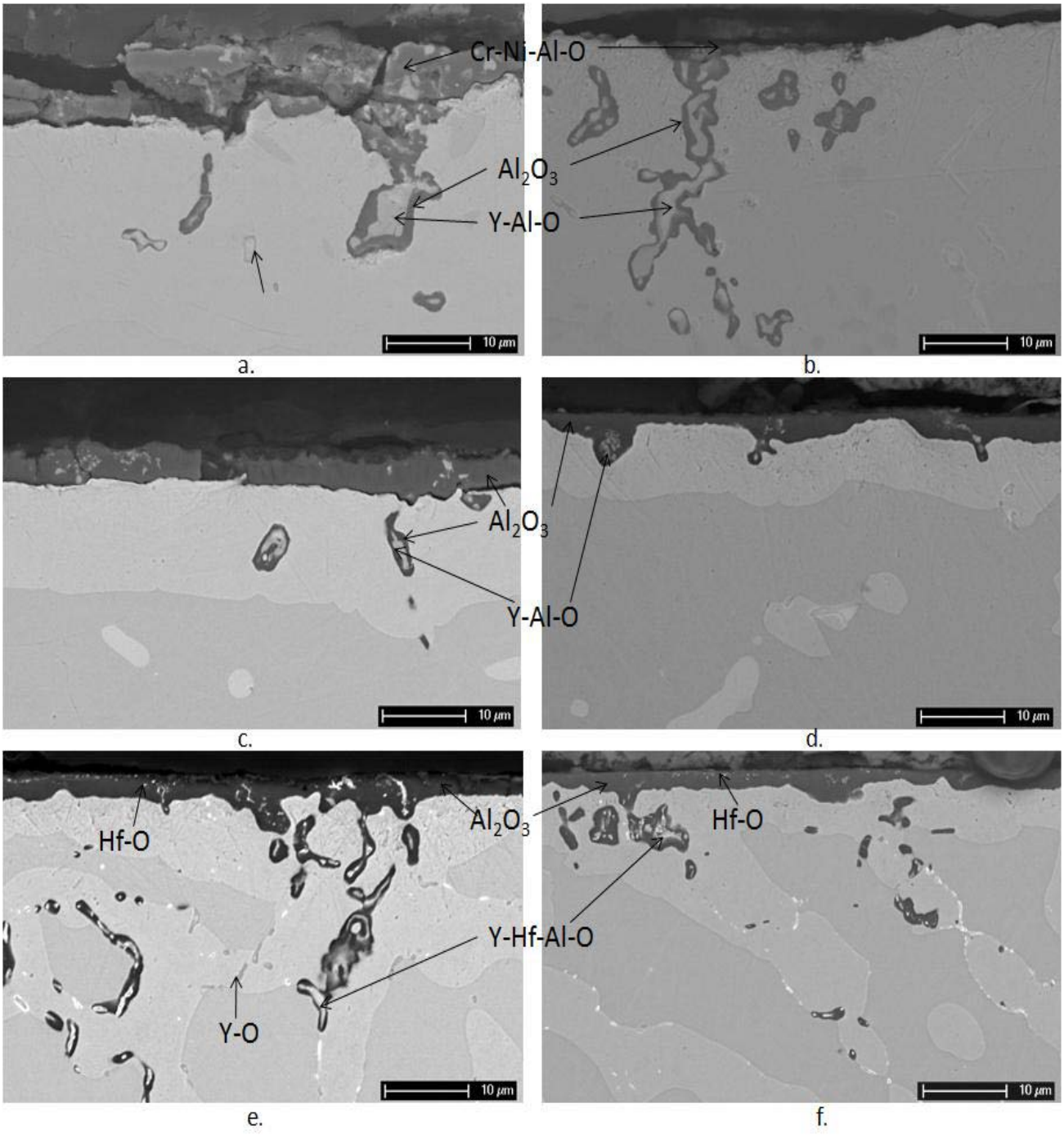

Figure 29. Cyclic oxidation and intermittent Type I microstructures: a.) NiCrAlY cyclic, b.) NiCrAlY intermittent Type I, c.) CoCrAlY cyclic, d.) CoCrAlY intermittent Type I, e.) NiCoCrAlY cyclic, f.) NiCoCrAlY intermittent Type I

In accordance with Figure 28, these microstructures indicate no large difference in oxidation behavior when cyclic oxidation is preceded by a brief period of Type I hot corrosion. In both cases, the CoCrAlY and NiCoCrAlY alloys have grown planar, adherent α-Al_2O_3 scales. β-phase depletion layers can be observed in both specimens, and a significant amount of internal oxidation is observed in the NiCoCrAlY. Preferential oxidation of Y/Hf-rich phases can result in the formation of oxide intrusions in the alloy [46]. Such oxide intrusions are clearly evident in all micrographs in Figure 29, where the Y-rich oxides are sheathed in Al_2O_3, as is commonly observed [47-48] .

Figure 28 and Figure 29 clearly indicate that the NiCrAlY alloy experiences a significant amount of scale spallation during cyclic oxidation. This does not appear to be a result of the initial hot corrosion exposure because the same behavior is observed in both specimens. This behavior will be explained in section 5.4.

It is evident that the initial Type I hot corrosion exposure had minimal effect on the oxidation of the MCrAlY alloys. These are very good Al_2O_3-forming alloys and are quite resistant to Type I hot corrosion (section 5.2.1), and so a short Type I exposure did not hinder the alloys' abilities to form protective scales during oxidation. For comparison, the single crystal Ni-base superalloy René N5 (Ni-7Cr-6.2Al-7.5Co-6.5Ta-6W-0.6Mo-1Ti-0.1Hf-3Re-0.1Y) was tested under the same conditions. The kinetic plot for the cyclic oxidation and intermittent hot corrosion of the N5 is presented in Figure 30:

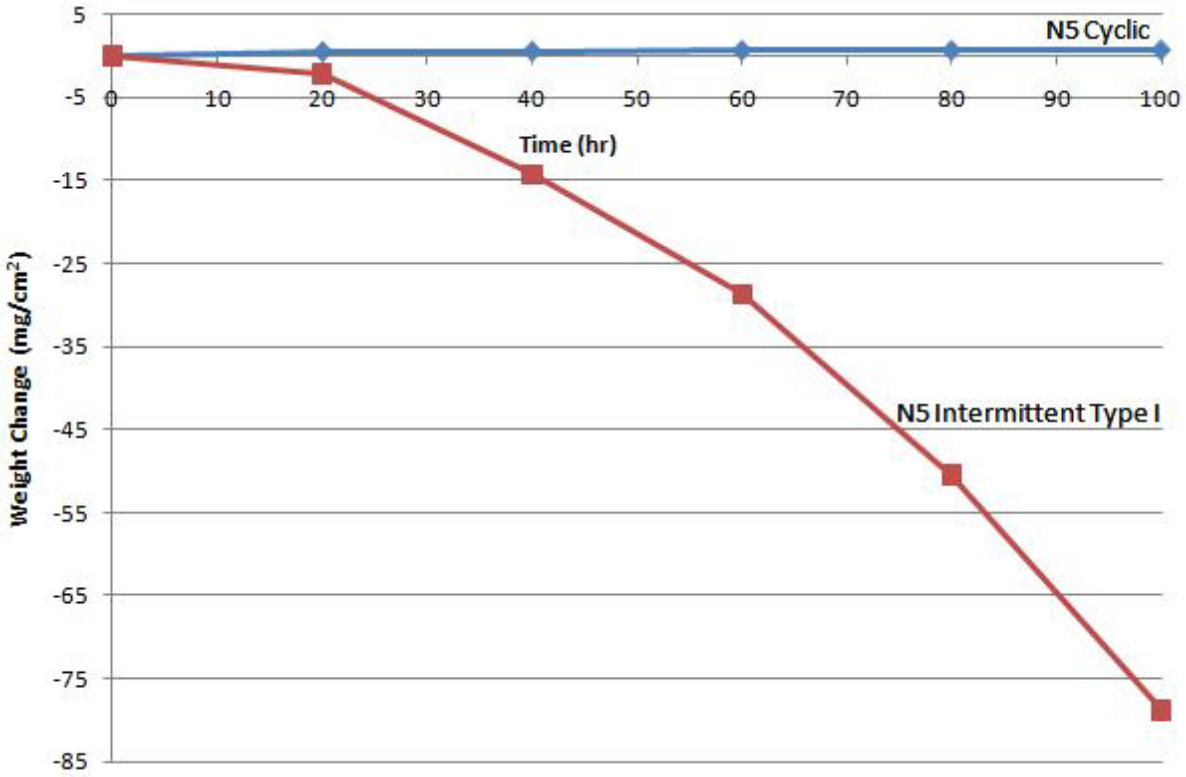

Figure 30. Weight change vs. time: René N5 intermittent Type I and cyclic oxidation

The N5 exposed only to cyclic oxidation at 1100°C displays parabolic growth kinetics throughout the exposure, while large amounts of spallation are observed during oxidation when it is preceded by a Type I exposure. Cross-sectional SEM micrographs of these two N5 specimens can be found in Figure 31, Figure 32 and Figure 33.

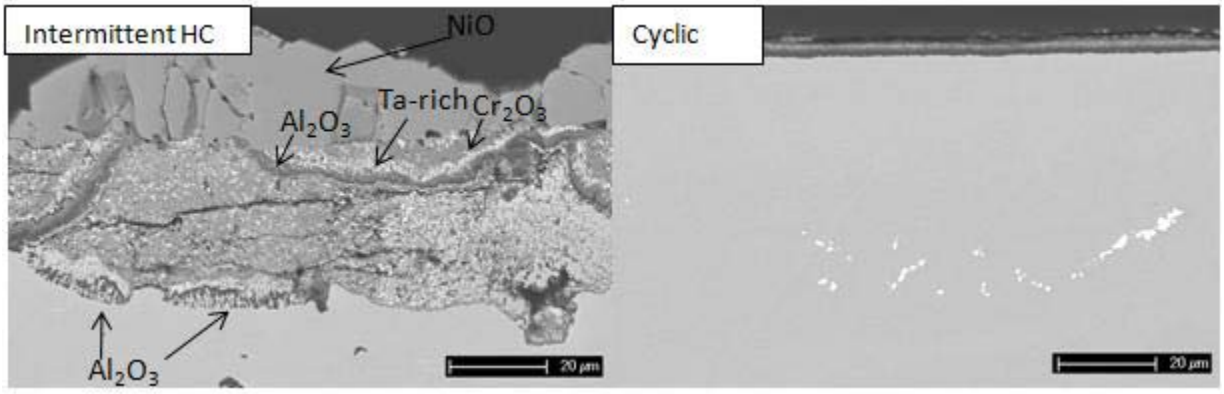

Figure 31. Intermittent Type I and cyclic oxidation microstructures: René N5

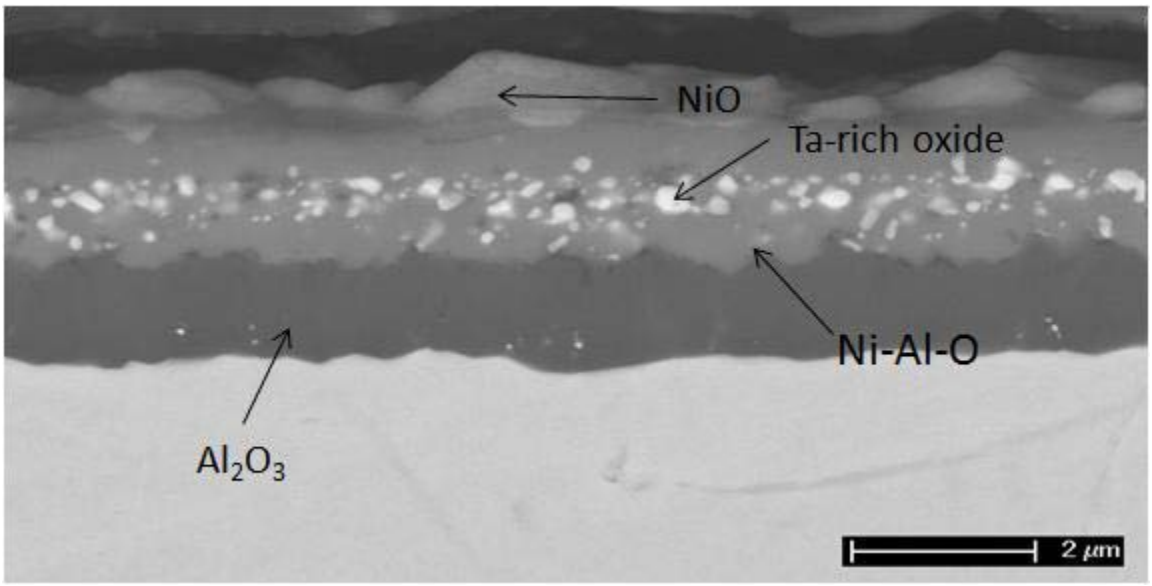

Figure 32. Cyclic oxidation microstructure: René N5

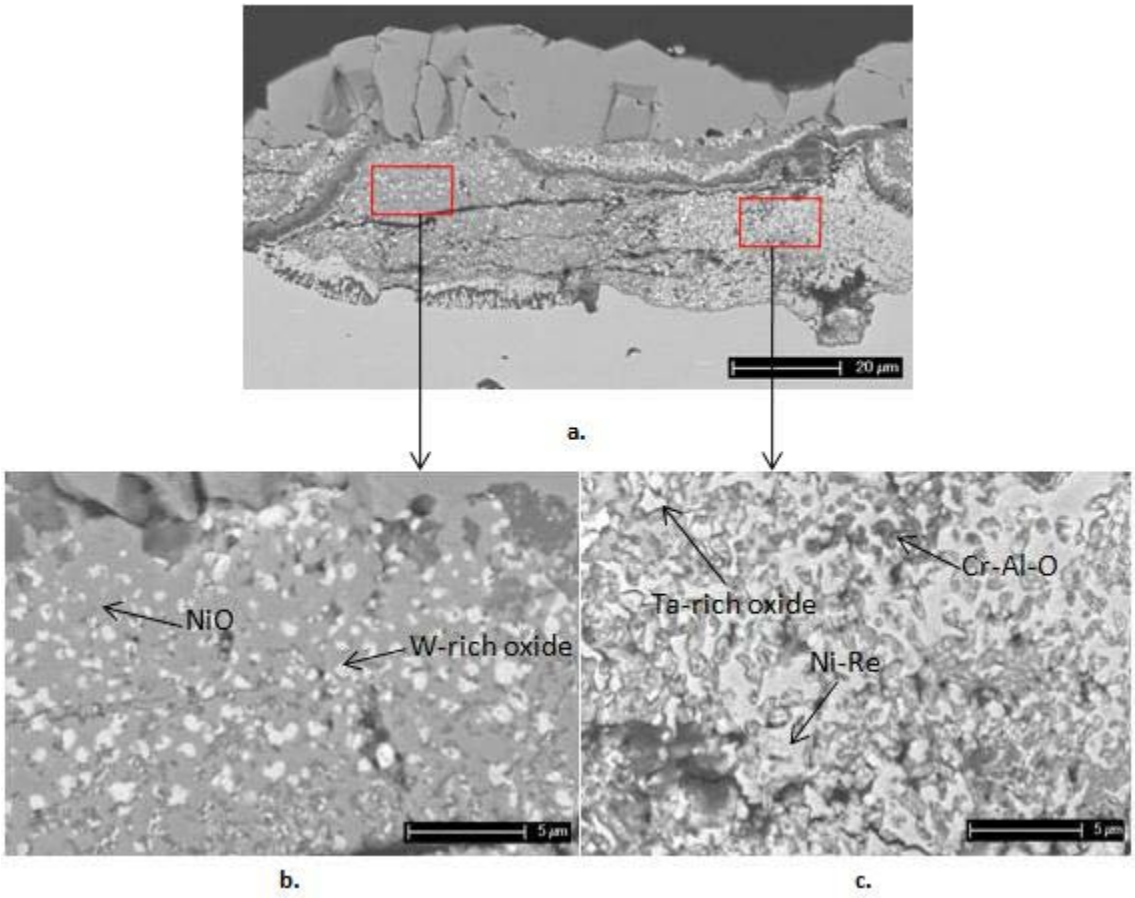

Figure 33. Intermittent Type I microstructure: René N5

It is found in Figure 32 that under these conditions, René N5 forms a protective multilayer scale during oxidation. At the base, a thin Al_2O_3 scale is formed, above which there is a Ni-Al- rich oxide, likely $NiAl_2O_4$ spinel, embedded with Ta-rich oxides. NiO is present at the surface. Scales with such significant amounts of adherent transient oxides have previously been observed on single crystal Ta-containing superalloys [49-50]. Steady-state oxide growth should, in this case, be controlled by the thickening of the Al_2O_3 scale.

Clearly, an initial hot corrosion exposure interrupts the selective oxidation of Al during subsequent cyclic oxidation (Figure 31). This is due to depletion of the scale-forming elements Al and Cr during the hot corrosion exposure. It is also likely that sulfur, which is injected into the alloy during hot corrosion, weakens the scale/alloy interface and promotes spallation [51]. A thick (~25μm), columnar NiO scale is observed at the surface of the alloy, underneath which a complex reaction product consisting of the oxides of every reactive element in the alloy has formed. In many regions the NiO has spalled, leaving only a mixed oxide at the alloy surface (see Figure 35). Somewhat similar corrosion products, consisting of a thick Ni-rich oxide scale above a complex mixed oxide, have been observed on N5 after high temperature oxidation in the presence of solid CaO deposits [52].

The intermittent hot corrosion exposure of N5 presents an interesting case of internal oxidation in the presence of an external base-metal scale. The internal oxidation zone shown in Figure 33c. is similar to what one may expect under these conditions, i.e., a matrix of basically pure Ni with some Re in solution with a dispersion of internal oxide precipitates. The classical theory of internal oxidation states that at the NiO/alloy interface, the p_{O_2} is fixed by the following equilibrium:

$$Ni + \frac{1}{2}O_2(g) = NiO \tag{42}$$

$$K = \frac{1}{a_{Ni}p_{O_2}^{1/2}} \tag{43}$$

In the simplified case of a binary alloy, a_{Ni} ~1. Atomic oxygen diffuses from this interface through the Ni matrix to the internal oxidation front, where the critical activity product $a_O a_B$ (B=solute species) for the oxide BO_v is reached and thus this oxide is precipitated internally [53]. A schematic of the concentration profiles of oxygen and solute during the internal oxidation of a simplified binary alloy are shown in Figure 34:

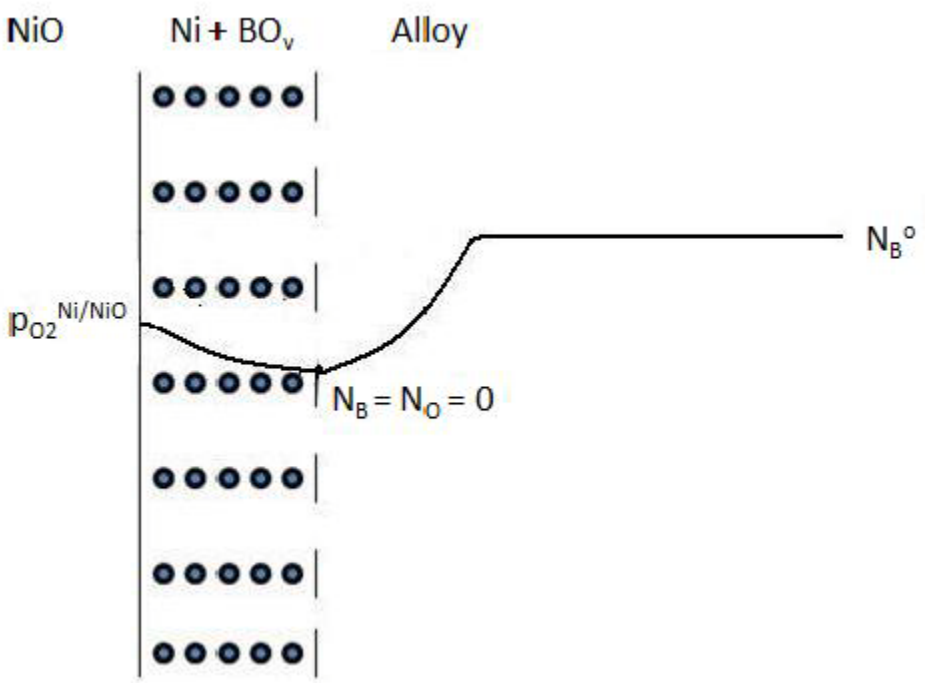

Figure 34. Schematic oxygen and solute concentration profiles during internal oxidation of a binary Ni-base alloy

where N_B^O is the bulk concentration of solute B in the alloy. According to this mechanism, the activity of oxygen is not sufficient to form NiO within the internal oxidation zone (IOZ). However, in Figure 33 b. there is a distribution of internal oxides within a NiO matrix, all below an external NiO scale. Therefore the activity of oxygen in the IOZ must have been raised to a value higher than the equilibrium p_{O_2} calculated using Eq. 43.

Figure 35 shows a lower-magnification SEM micrograph of the N5 intermittent hot corrosion specimen:

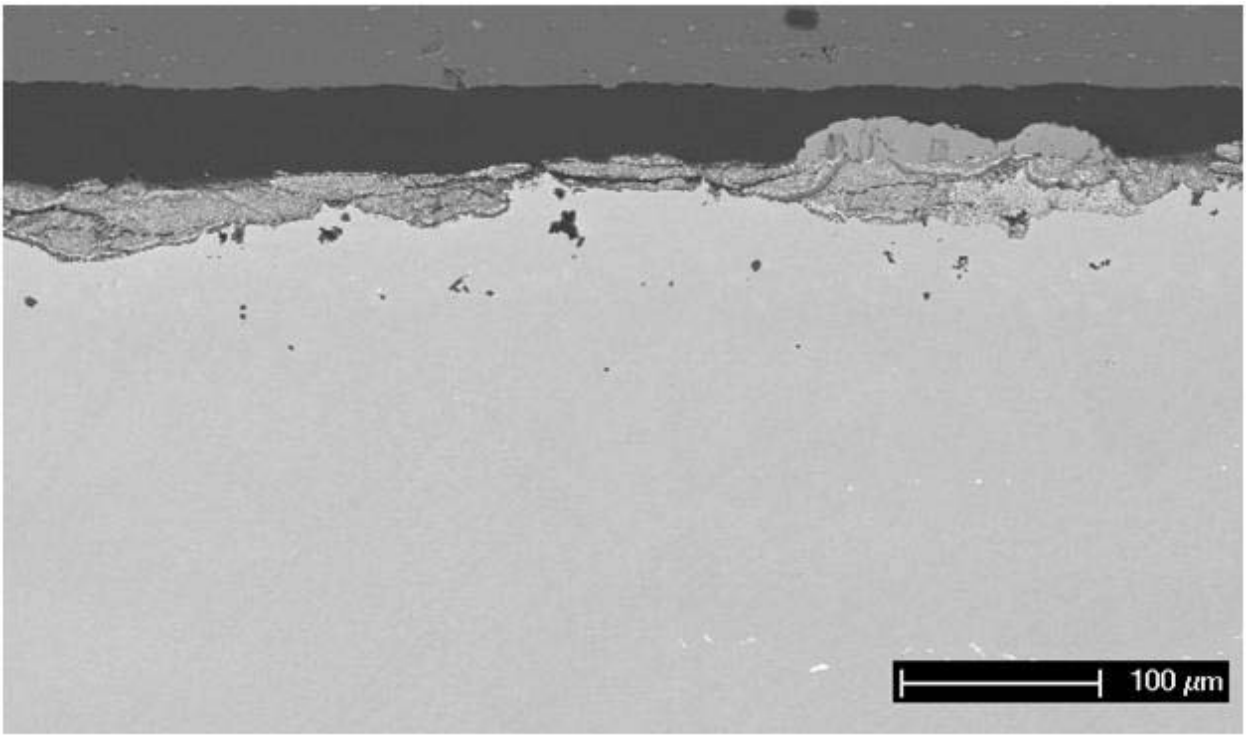

Figure 35. Intermittent Type I microstructure: René N5 (low mag)

In the leftmost region of the micrograph, the external NiO scale has spalled, leaving only the IOZ. These areas are similar to those found in Figure 33b., i.e. the internal oxide precipitates are embedded in a matrix of NiO. When the external NiO scale spalls, the surface of the IOZ is then exposed to a much higher p_{O_2} (~0.2 atm) than that provided by the Ni/NiO equilibrium. This results in a large inward flux of oxygen which is sufficient to oxidize the Ni matrix in the IOZ, resulting in the observed microstructure.

The diffusivity of oxygen in Ni at 1100°C is 7.98 x 10^{-10} cm^2/s [54]. Therefore, the diffusion distance of oxygen in Ni for 100 hours at 1100°C,$\sqrt{Dt}$, is approximately 170 μm. The oxidation of the Ni matrix in the IOZ below a NiO scale can thus be explained by the lateral diffusion of oxygen from neighboring regions where the external scale has spalled. Experimentally, this calculation will be complicated by the blocking of oxygen by previously-formed internal oxides; however, this effect will be at least partially offset by the enhanced diffusivity of oxygen along internal oxide/Ni interfaces.

NiO is a cation-deficient oxide which typically forms by outward-migration of Ni^{2+} ions [6, 55]. If, under these experimental conditions, there is significant inward growth of NiO, it would be possible for the inward-growing NiO to engulf the oxides in the IOZ, resulting in the microstructure shown in Figure 33 b. There is, however, no evidence to support this scenario.

5.3 HOT CORROSION AND OXIDATION OF DROP CAST NiCoCrAlY-2 and NiCoCrAlY-3

Based on the results presented in section 5.2, the alloys were ranked in terms of resistance to cyclic oxidation, intermittent Type I hot corrosion, Type I hot corrosion, and Type II hot corrosion. The results of this ranking are, from most resistant to least resistant:

Oxidation: NiCoCrAlY/CoCrAlY, NiCrAlY

Intermittent Type I: NiCoCrAlY/CoCrAlY, NiCrAlY

Type I: NiCoCrAlY/CoCrAlY, NiCrAlY

Type II: NiCrAlY, NiCoCrAlY, CoCrAlY

The most aggressive condition examined in this study is clearly Type II hot corrosion, and under these conditions the NiCrAlY alloy out-performed all others. However, due to the inferiority of the NiCrAlY under Type I and particularly 1100°C cyclic oxidation conditions, it was precluded from being chosen for further development. The CoCrAlY alloy proved to be fairly resistant to degradation due to Type I hot corrosion, cyclic oxidation (up to 100 cycles), and intermittent Type I hot corrosion. However, this alloy is extremely susceptible to Type II hot corrosion attack and was therefore not chosen for further development. The results for the NiCoCrAlY alloy seem most promising. It performed quite well under Type I, intermittent Type I, and cyclic oxidation conditions, and although it was badly degraded during Type II hot corrosion, degradation was not as catastrophic as was observed for the CoCrAlY. Therefore, compositional changes were made to this alloy in an attempt to optimize its resistance to Type II hot corrosion without sacrificing its resistance to all other types of degradation.

Due to the well-known vulnerability of Co-base alloys to Type II hot corrosion, the atomic percentage of Co in the NiCoCrAlY was reduced to half of its original value. From this point, two new alloys were created, one by replacing the Co with Ni (NiCoCrAlY-2), and the other by replacing it with Cr (NiCoCrAlY-3).

5.3.1 Type I Hot Corrosion of Drop Cast NiCoCrAlY-2 and NiCoCrAlY-3

Type I hot corrosion exposures of the NiCoCrAlY-2 and NiCoCrAlY-3 were carried out for up to 500 hours. A kinetic plot of weight change per unit area vs. time is presented in **Figure 36.** The data for the NiCoCrAlY specimen is also included for comparison.

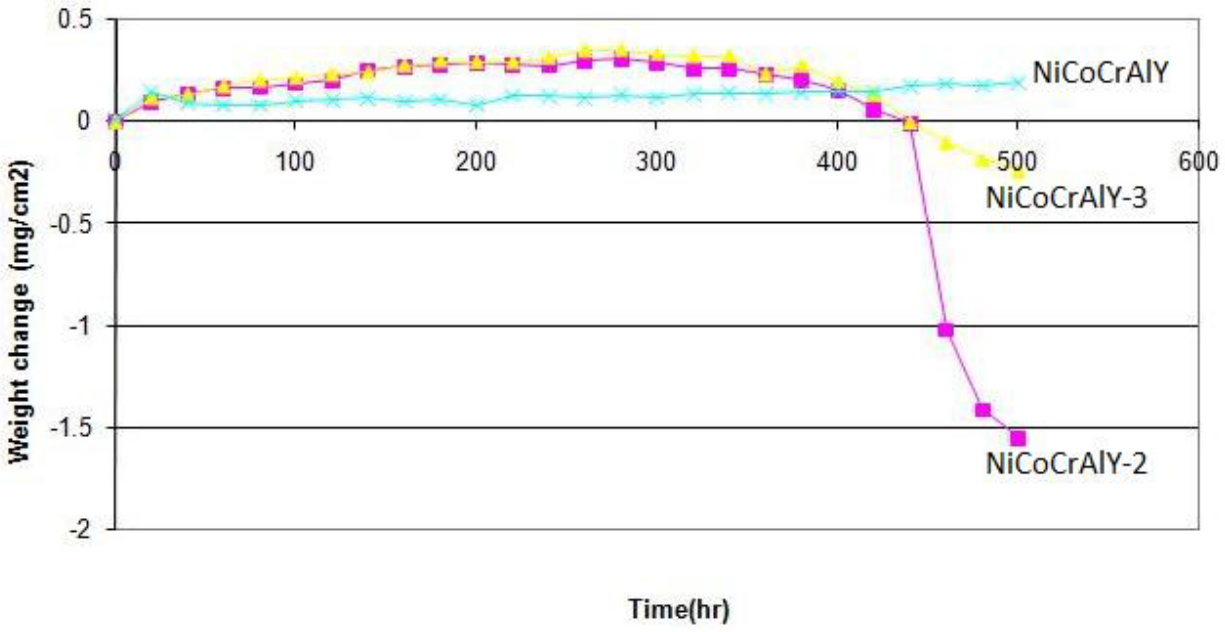

Figure 36. Weight change vs time: NiCoCrAlY, NiCoCrAlY-2, NiCoCrAlY-3 Type I hot corrosion

These kinetic data suggest that up to approximately 400 hr, the modified NiCoCrAlY alloys suffered no decrease in Type I hot corrosion resistance. Weight gains were approximately equal for the NiCoCrAlY-2 and NiCoCrAlY-3 throughout this time period. These weight gains were slightly higher than those observed in the case of the NiCoCrAlY, however they were modest and indicative of protective scale formation. Beyond 400 hr, weight losses were observed for the NiCoCrAlY-2 and NiCoCrAlY-3 alloys, however these were initiated at casting defects in the center of the specimens and were thus not representative of the alloys' performances.

Representative microstructures of the NiCoCrAlY-2 and NiCoCrAlY-3 alloys after 500 hr exposure to Type I conditions are shown in Figure 37.

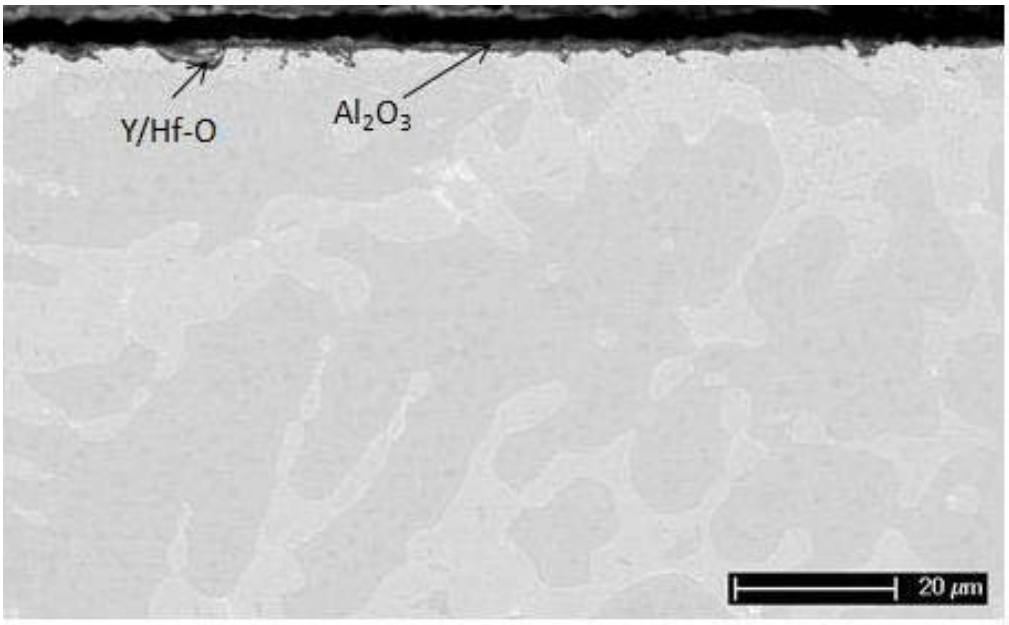

a.

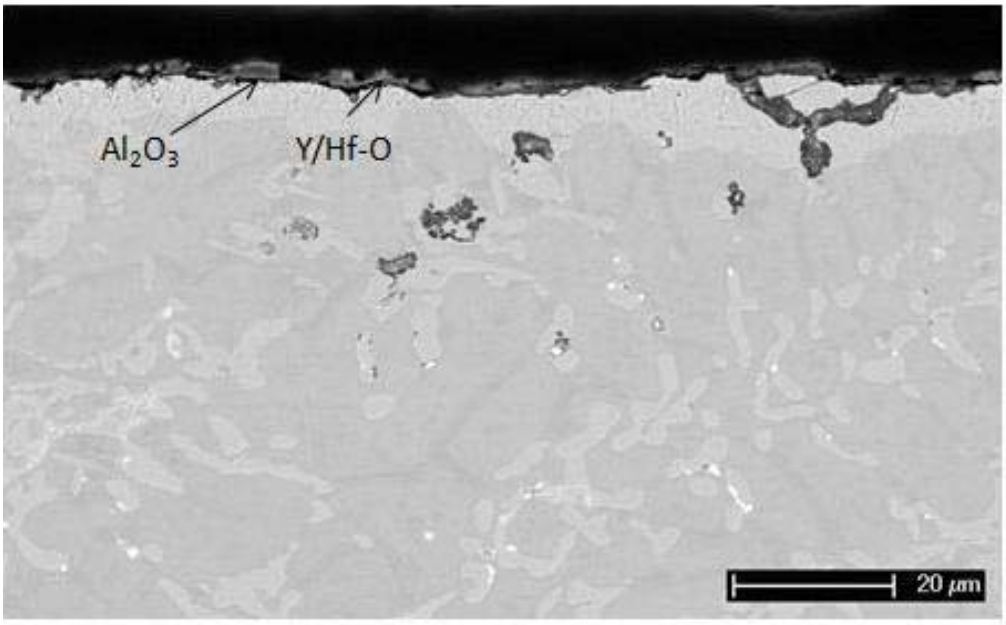

b.

Figure 37. Type I hot corrosion microstructures: a.) NiCoCrAlY-2, b.) NiCoCrAlY-3

The microstructures in Figure 37 indicate that fairly protective scales were indeed formed over the majority of the surfaces of these two specimens. Hf and Y rich oxide inclusions, similar to those observed in Figure 19c., were present in the scale.

From Figure 36 and Figure 37 it is apparent that the compositional modifications made to the NiCoCrAlY alloy resulted in no appreciable decrease in Type I hot corrosion resistance for the exposure times utilized in the current study.

5.3.2 Type II Hot Corrosion of Drop-Cast NiCoCrAlY-2 and NiCoCrAlY-3

Cross sectional microstructures of the NiCoCrAlY-2 and NiCoCrAlY-3 alloys after 10 hours of exposure to Type II hot corrosion conditions are presented in Figure 38:

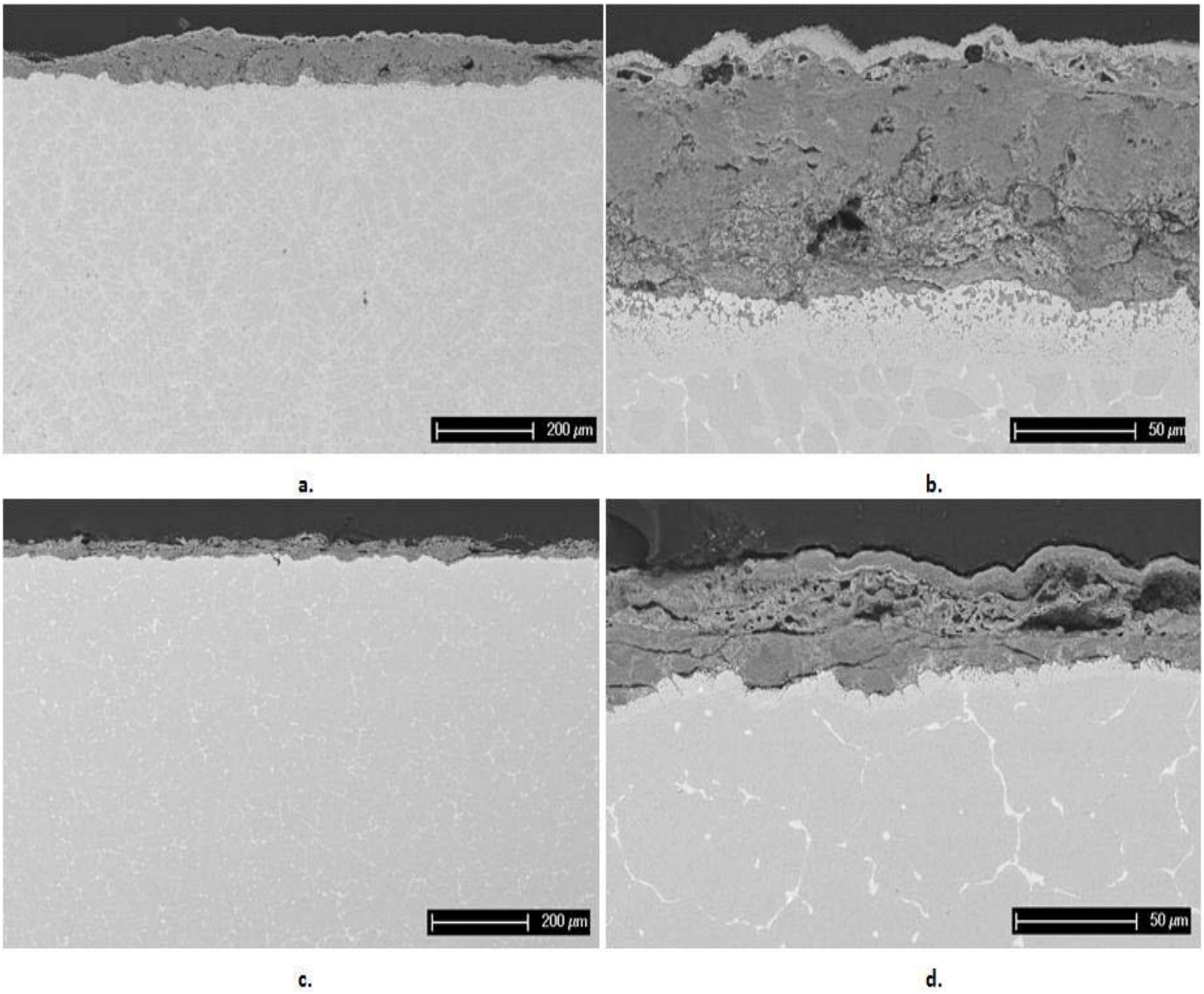

Figure 38. Type II microstructures: a,b.) NiCoCrAlY-2, c,d.) NiCoCrAlY-3

It is observed in Figure 38a. and b. that lowering the Co content of the NiCoCrAlY alloy and replacing it with Ni, as was done in the case of NiCoCrAlY-2, had no beneficial effect in terms of Type II hot corrosion resistance. The higher-Cr NiCoCrAlY-3, however, while still rapidly degraded under these conditions, displayed slightly more protective behavior. The corrosion product formed on this alloy was approximately 2-3 times thinner than that formed on NiCoCrAlY and NiCoCrAlY-2, the Al-denuded zone was much shallower, and the degree of internal sulfidation was greatly reduced. X-ray maps of NiCoCrAlY-2 and NiCoCrAlY-3 specimens after 10 hours of Type II hot corrosion exposure are presented in Figure 39 and Figure 40, respectively.

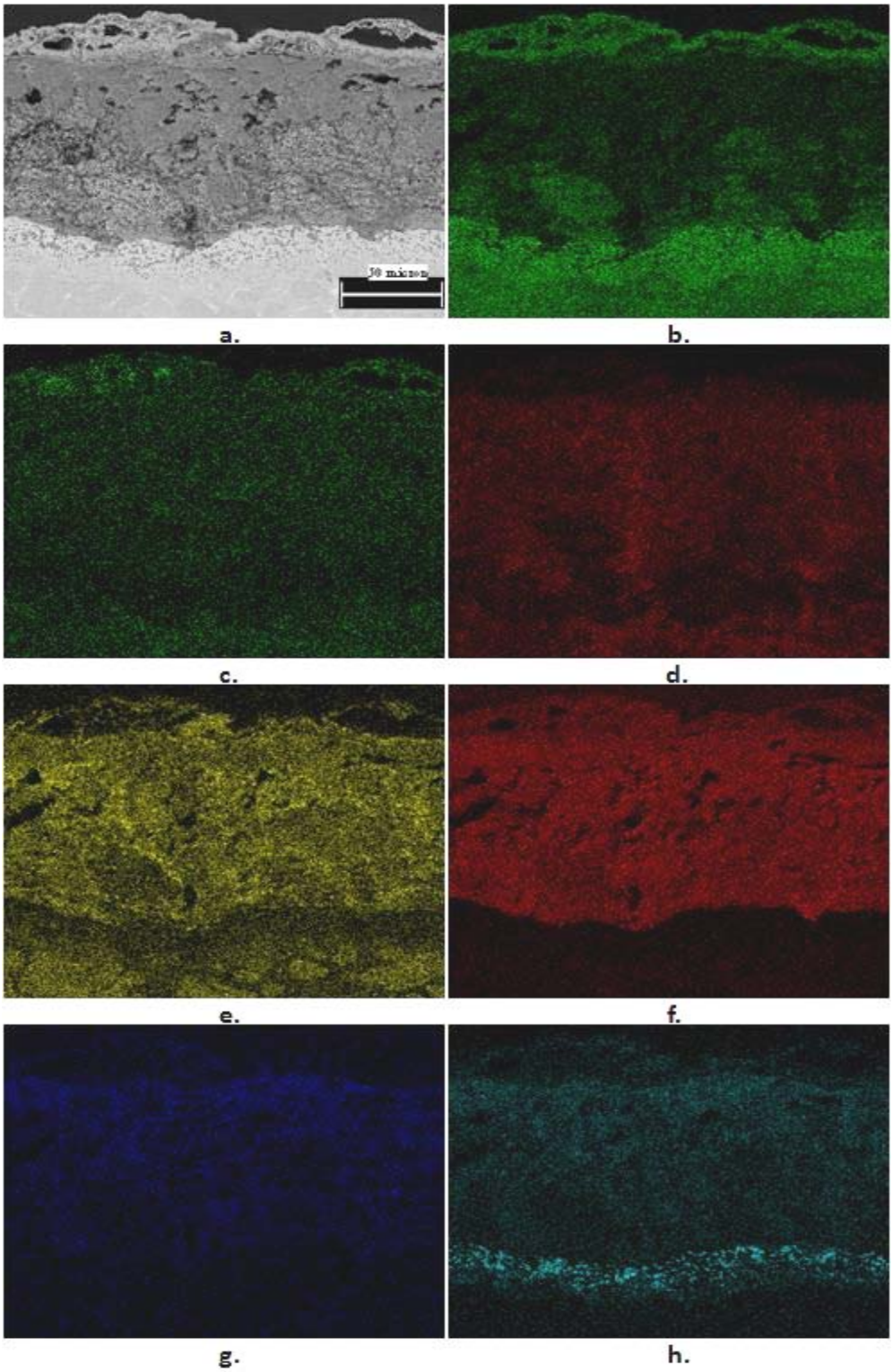

Figure 39. NiCoCrAlY-2 Type II x-ray map: a.) BSEmicrograph, b.) Ni, c.) Co, d.) Cr, e.) Al, f.) O, g.) Na, h.) S

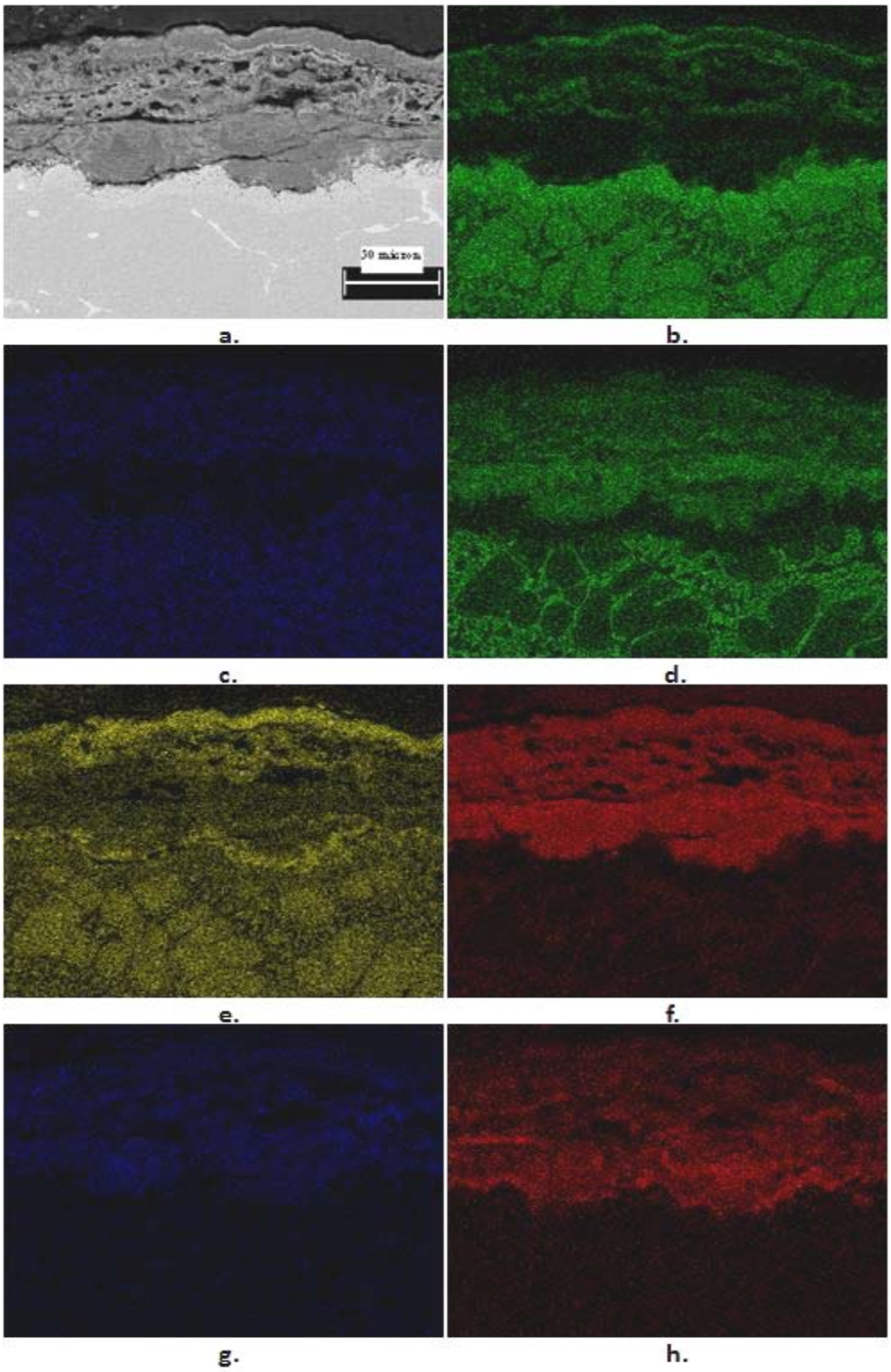

Figure 40. NiCoCrAlY-3 Type II x-ray map: a.) BSEmicrograph, b.) Ni, c.) Co, d.) Cr, e.) Al, f.) O, g.) Na, h.) S

In the NiCoCrAlY-2 alloy (Figure 39), no significant Cr or Al enrichment is observed at the base of the pit. The Cr and Al denuded zone below the pit is therefore attributed solely to the internal sulfidation of these elements, as is clearly observed in Figure 38 b. and Figure 39 h. Conversely, the NiCoCrAlY-3 has a significant enrichment of Cr at the base of the pit. There is a small amount of internal oxidation/sulfidation below the pit, typically occurring along interphase boundaries surrounding the α-phase, but it is not significant. Thus, the Cr-denuded zone beneath the corrosion front in the NiCoCrAlY-3 alloy is attributable largely to the formation of a Cr-rich corrosion product at the base of the pit.

The formation of a Cr-rich corrosion product at the base of the corrosion pits in the NiCoCrAlY-3 alloy seems to be responsible for the enhanced Type II hot corrosion resistance of this alloy, relative to the NiCoCrAlY and NiCoCrAlY-2. The NiCoCrAlY-3 has a cellular microstructure, consisting of a β matrix surrounded by a fairly continuous network of α-Cr (Figure 17). High Cr levels, leading to the precipitation of α-Cr in the microstructure, are beneficial in terms of Type II hot corrosion resistance. As will be discussed in section 5.5, it is not only the presence of the α phase which is important, but in addition its distribution plays a major role. In the NiCoCrAlY-3, this phase is continuous rather than discrete and discontinuous, which promotes protective Cr-rich oxide formation.

5.3.3 Cyclic Oxidation and Intermittent Hot Corrosion of Drop Cast NiCoCrAlY-2 and NiCoCrAlY-3

Kinetic plots for the cyclic oxidation and intermittent hot corrosion of the drop cast NiCoCrAlY alloys for up to 100 cycles of cyclic oxidation are presented in Figure 41:

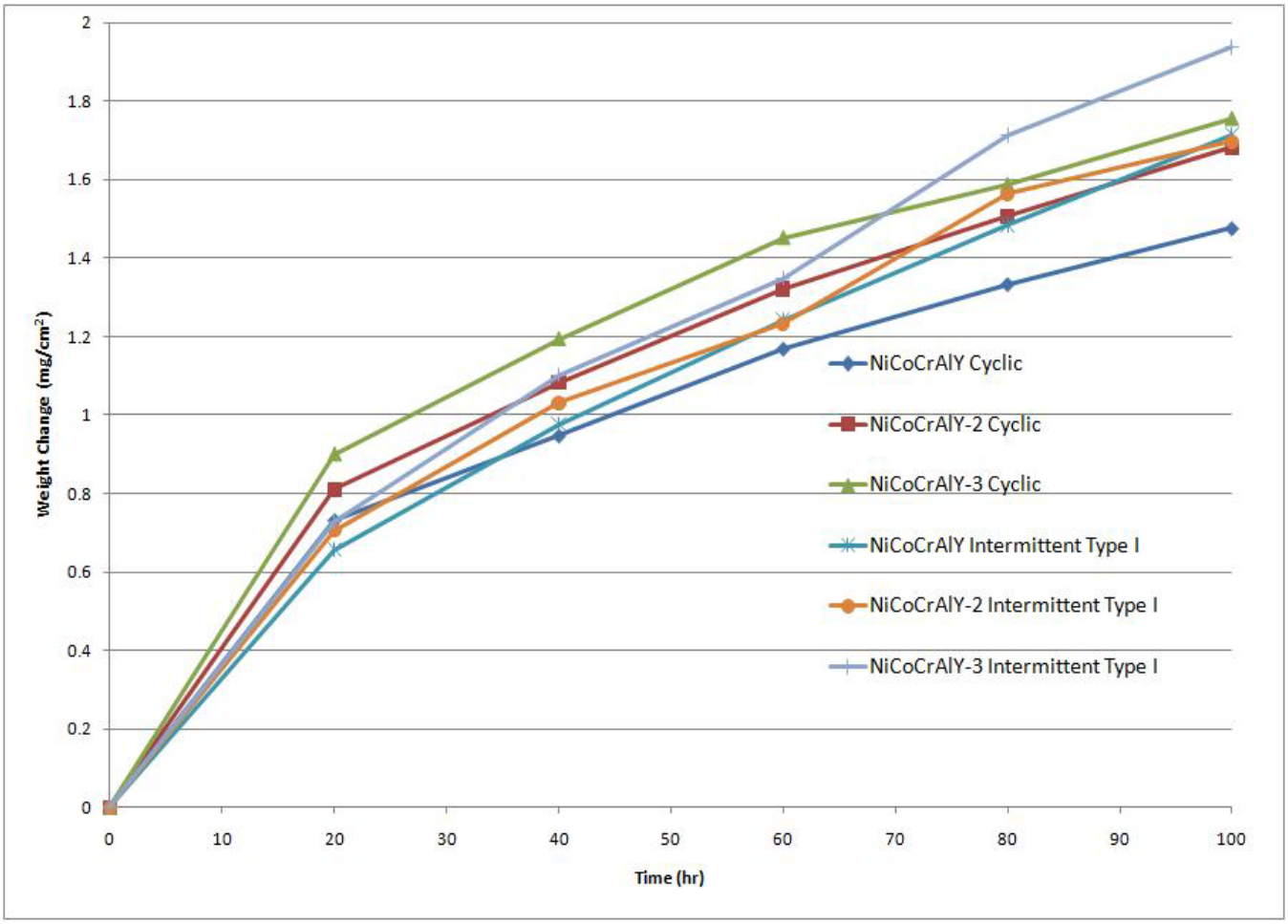

Figure 41. Weight change vs. time: NiCoCrAlY, NiCoCrAlY-2, NiCoCrAlY-3 intermittent Type I and cyclic oxidation

This kinetic plot suggests that the compositional modifications made to the original NiCoCrAlY did not have a negative effect on cyclic oxidation or intermittent hot corrosion performance. The cyclic oxidation plots for the NiCoCrAlY-2 and the NiCoCrAlY-3 were very similar to the plot for the NiCoCrAlY, which is included in Figure 41 for comparison. Also, for each alloy, the plots for intermittent hot corrosion and cyclic oxidation coincide, as is true for all MCrAlY alloys examined in this study (*cf.* Figure 28).

Comparative micrographs of the NiCoCrAlY-2 and NiCoCrAlY-3 alloys exposed to intermittent hot corrosion and cyclic oxidation are presented in Figure 42:

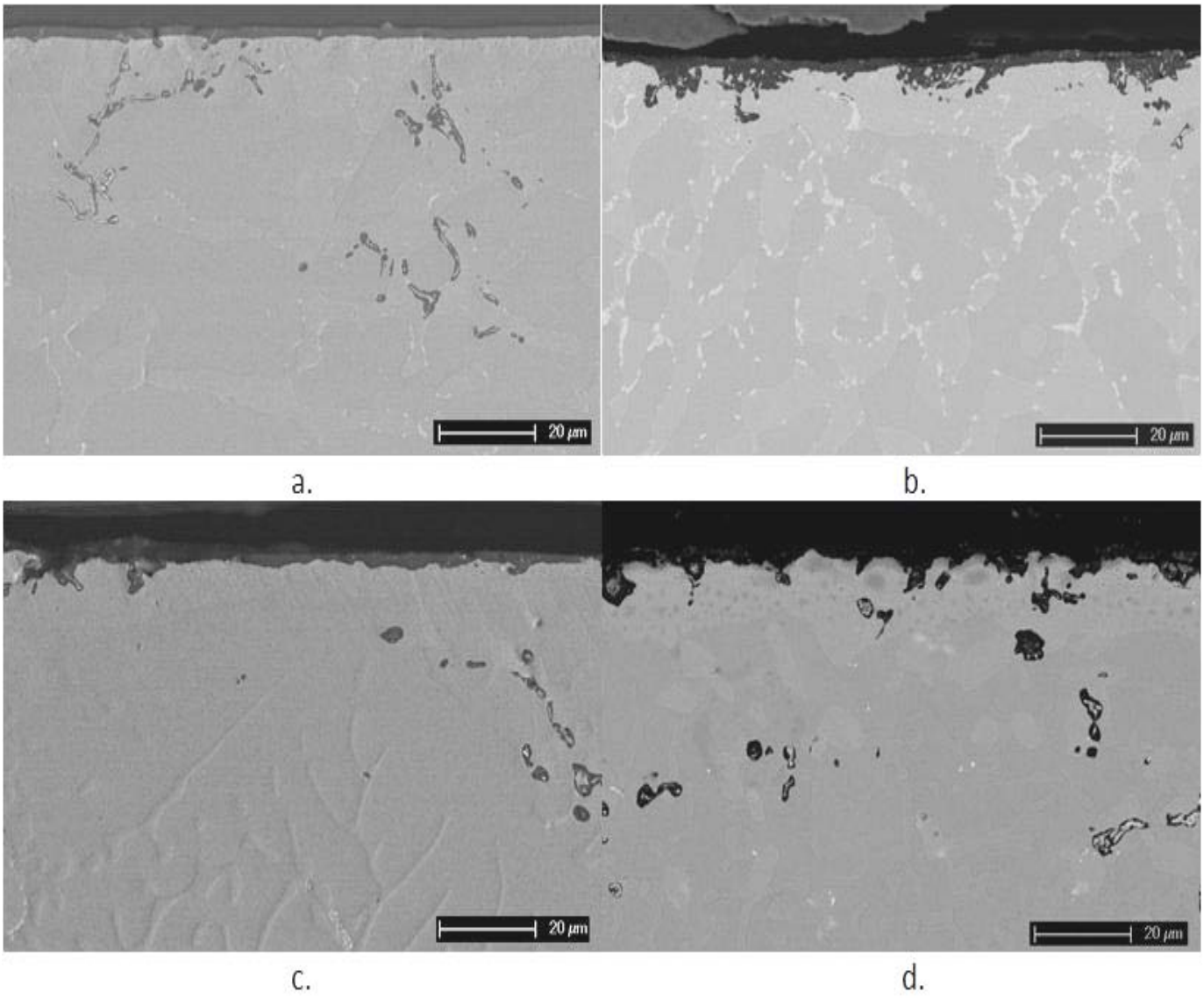

Figure 42. Cyclic oxidation and intermittent Type I microstructures: a.) NiCoCrAlY-2 cyclic, b.) NiCoCrAlY-2 intermittent Type I, c.) NiCoCrAlY-3 cyclic, d.) NiCoCrAlY-3 intermittent Type I

No significant microstructural differences are observed between specimens exposed only to cyclic oxidation and cyclic oxidation preceded by 20 hours of Type I exposure. Thin Al_2O_3 scales formed and remained adherent in all cases. Significant internal oxidation of the reactive-element rich phases is once again observed. This resulted in considerable local Al-depletion and $\beta \rightarrow \gamma$ transformation to depths >100μm, as shown in Figure 43, but this did not seem to have a negative effect on the oxidation resistance of this alloy for the exposure times studied. It is recognized, however, that in the case of a coated superalloy, such internal oxidation may pose a significant problem since the IOZ depth is approaching the thickness of a common overlay coating.

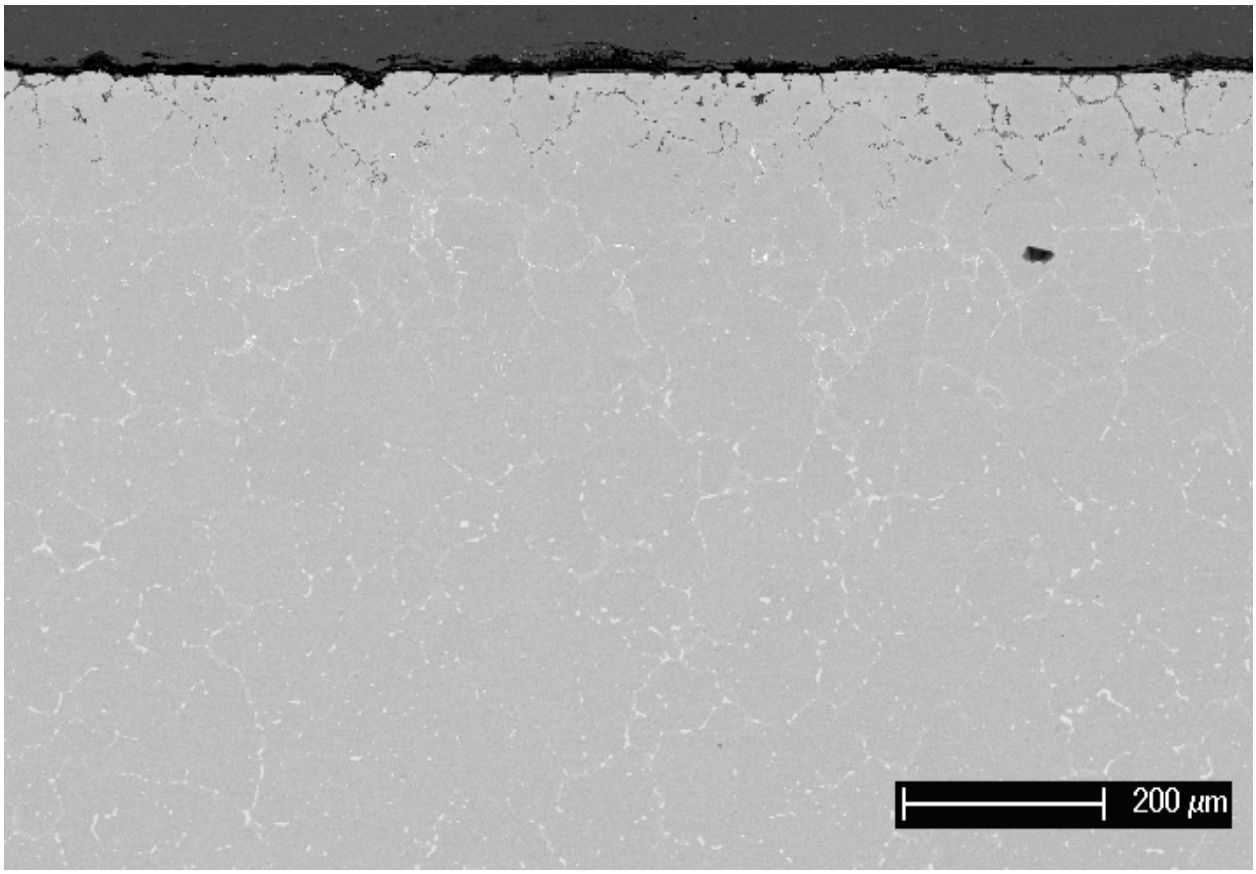

Figure 43. Intermittent Type I microstructure: NiCoCrAlY-3

5.4 PHASE EQUILIBRIA IN THE NiCrAlY SYSTEM

5.4.1 Computational and Experimental Study of Phase Stability

The identity, relative amount, and approximate composition of each phase of the NiCrAlY alloy were determined after equilibration at 700°C, 900°C, and 1100°C using SEM/EDS, XRD, and image analysis. The CALPHAD method was used to predict the phase equilibria in this system, and the results were compared with experiment. This analysis, coupled with dilatometric data, was used to explain the poor oxidation behavior displayed by the NiCrAlY (see Section 5.2.3).

5.4.1.1 Microstructural Equilibration

Specimens ~3 mm thick were equilibrated at 700°C, 900°C, and 1100°C by heat treating for 400 h, 200 h, and 30 h, respectively, in a tube furnace. Specimens were water quenched after exposure in an attempt to prevent any diffusional transport below the heat-treating temperature and thus maintain the equilibrated structures.

5.4.1.2 Comparison of Measured and Calculated Phase Distribution

Cross-sectional SEM micrographs of the NiCrAlY alloy after equilibration at each temperature are presented in Figure 44, along with a plot of the CALPHAD-predicted mass fractions as a function of temperature. For the CALPHAD predictions, a ternary Ni-Cr-Al database available in the literature [56] was used coupled with the commercially-available software package ThermoCalc**.** Predicted Ni-Cr-Al ternary phase diagrams at 700°C, 900°C, and 1100°C are presented in Figure 45.

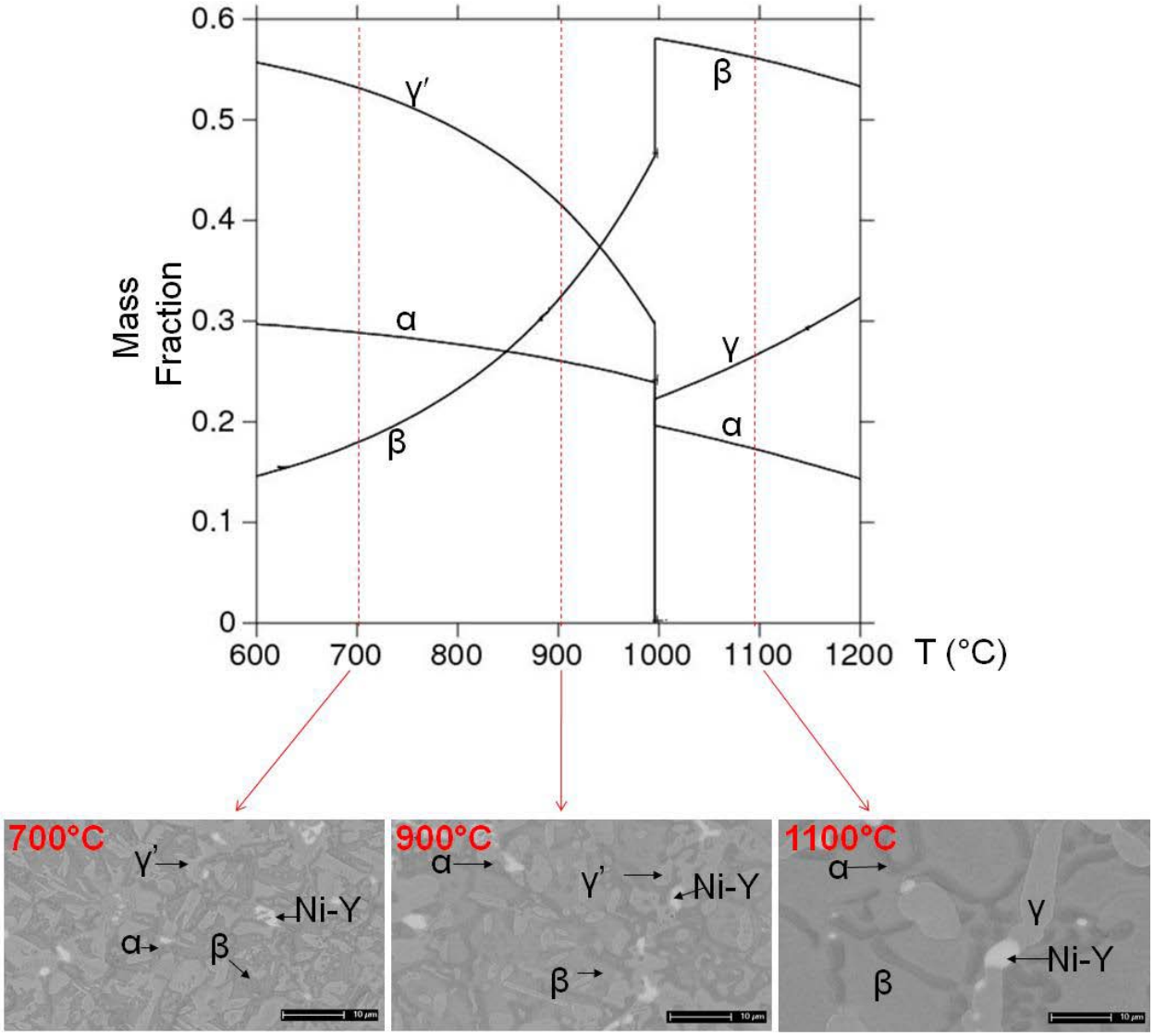

Figure 44. NiCrAlY equilibrated at various temperatures along with a plot of predicted mass fractions of each phase as a function of temperature

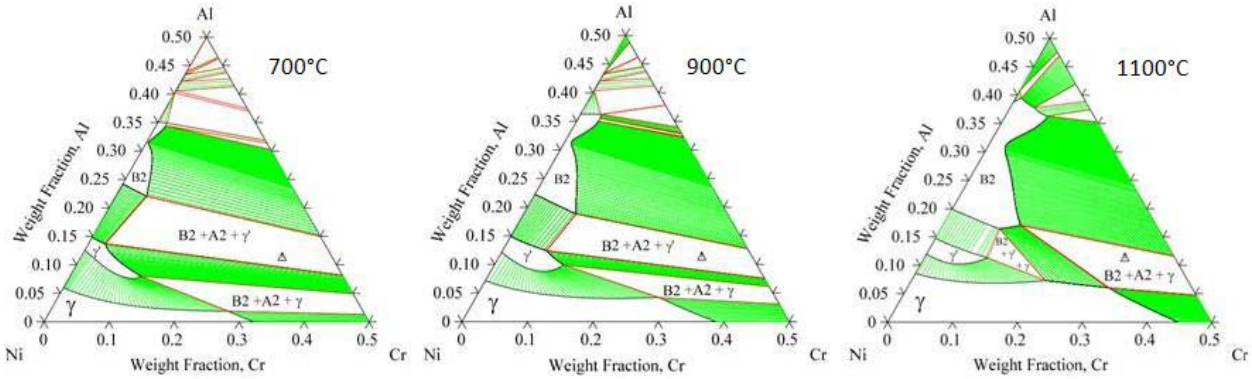

Figure 45. Isothermal sections through the Ni-Cr-Al space diagram

The phases are identified in Figure 44 on the basis of both XRD and EDS analysis. The phases present are generally in agreement with the CALPHAD predictions. Each specimen contains β-NiAl, α-Cr solid solution, γ′-Ni_3Al and/or γ-Ni solid solution, and a Ni-Y intermetallic phase. The Ni-Y phase is inferred to be a yttride. A yttride was not predicted by ThermoCalc because the necessary thermodynamic data for Yttrium was not available. At 700°C and 900°C, γ′, α, and β were detected via XRD in accord with CALPHAD predictions; their presence was confirmed using SEM. At 1100°C, α and β were also found, as predicted, however, it was not clear based on XRD whether γ′ was present in the microstructure in addition to γ. The presence of γ′ could be due to the inability to completely suppress its formation upon cooling from 1100°C, in spite of the water quench. A significant coarsening of the microstructure was observed with increasing heat treatment temperature.

Area fractions of each of these phases were measured using ImageJ software. The images shown in Figure 44, along with 24 others from each specimen, were digitally manipulated such that each of the phases could be isolated and its area fraction measured. An example is presented in Figure 46, which contains an image from the specimen equilibrated at 1100°C, manipulated such that the area fractions of each phase can be measured. Specifically, when a grayscale image is opened in the ImageJ software, each pixel is assigned a color value 0

through 255. One has the ability to create a binary image, such that all grayscale values below a certain number (0-255) are turned white, and all those above are turned black.

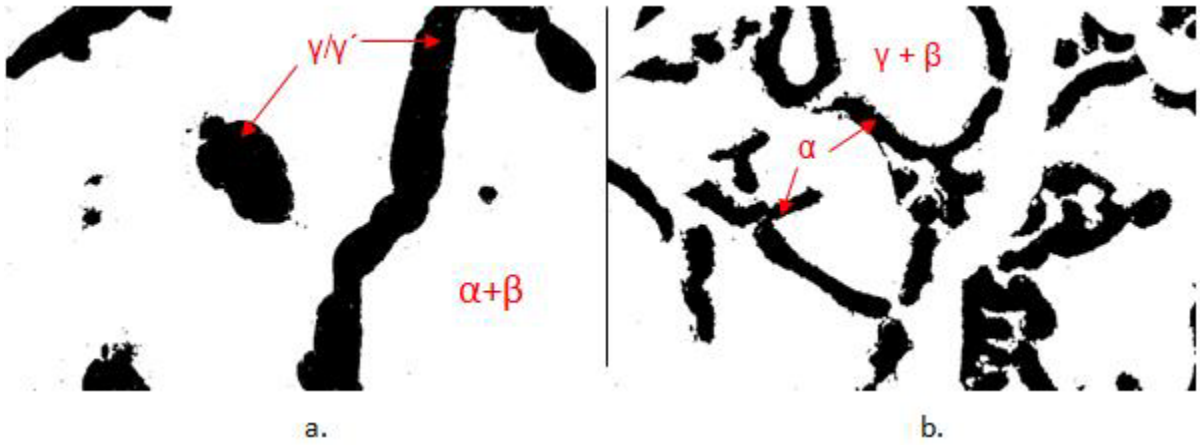

Figure 46. SEM images of the NiCrAlY equilibrated at 1100°C manipulated for quantitatve metallography

By isolating the γ/γ´ and separately isolating the α, the individual area fractions of all phases could be obtained. The area fraction of the yttride was measured prior to any image manipulation due to the sharp shading contrast which exists between this phase and the rest of the microstructure.

In accordance with relationships established from the science of quantitative stereology, the measured area fractions were taken to be equivalent to volume fractions. This is deemed a reasonable assumption provided a sufficient number of sections through the microstructure are examined [57]. Table 3 compares the measured and the CALPHAD-predicted volume fractions of each phase for the three heat treatment temperatures that were studied. This comparison is also illustrated graphically in Figure 47 for the γ/γ́ and β phases. The values in parentheses in the "Measured V_f" column in Table 3 are standard deviations. Agreement between predicted and measured values is reasonably good, with the former commonly being within one standard deviation of the latter.

Table 3. Measured and CALPHAD-predicted NiCrAlY phase volume fractions

Phase	Temperature (°C)	Predicted V_f	Measured Vf
γ′	700	0.50	0.53 (0.04)
β	700	0.22	0.20 (0.05)
α	700	0.28	0.26 (0.02)
Ni-Y	700	-	0.01 (0.01)
γ′	900	0.38	0.34 (0.04)
β	900	0.38	0.35 (0.07)
α	900	0.24	0.29 (0.06)
Ni-Y	900	-	0.02 (0.01)
γ/γ′	1100	0.20	0.22 (0.06)
β	1100	0.64	0.54 (0.09)
α	1100	0.16	0.22 (0.04)
Ni-Y	1100	-	0.02 (0.01)

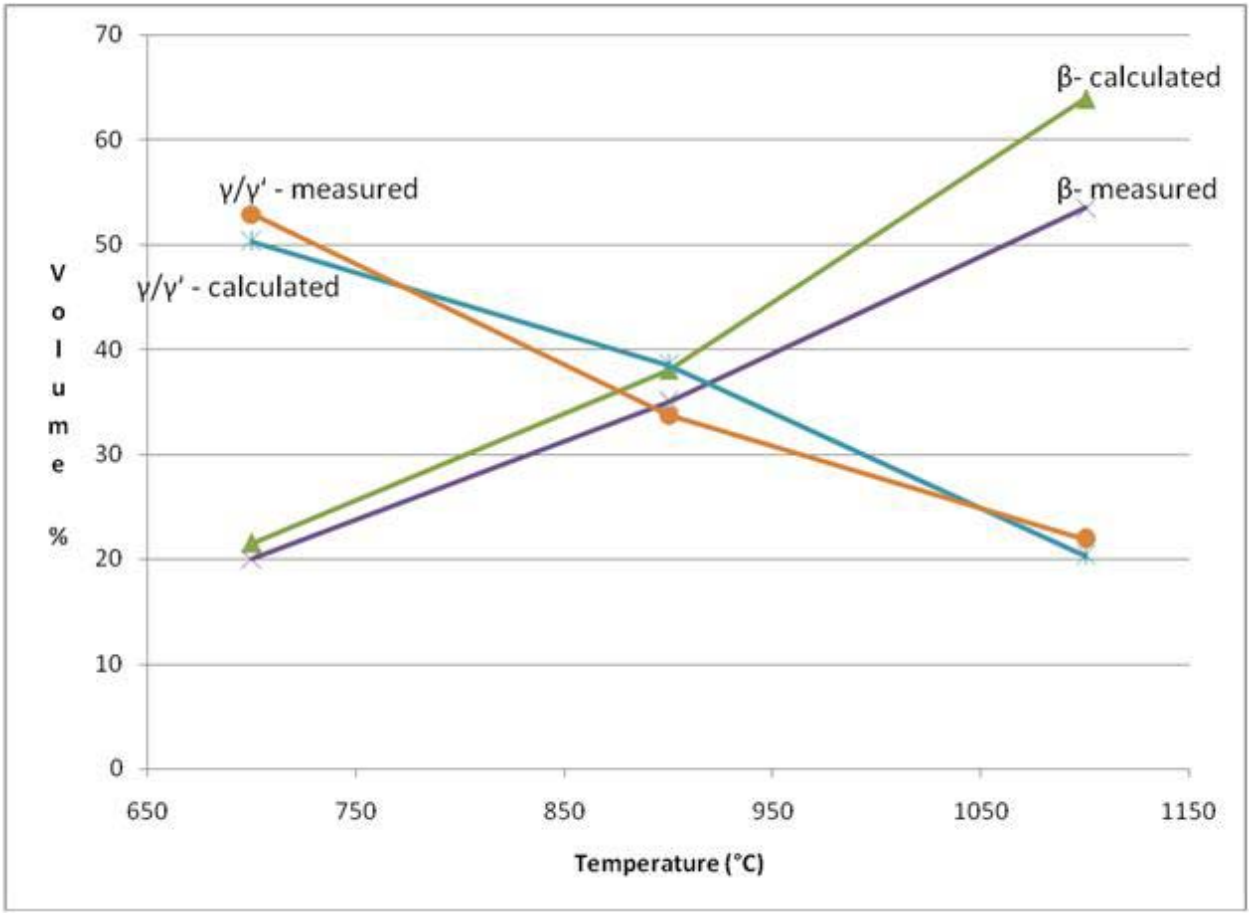

Figure 47. Measured and CALPHAD-predicted NiCrAlY phase volume percent vs. temperature

In addition to the error introduced in assuming the equality of area fraction and volume fraction, the presence of Y in the alloy clearly has an effect on the phase equilibria in this system, as indicated by the presence of yttrides. This would introduce another source of error. Finally, the calculations were done in terms of mass fractions, and these values were converted into volume fractions. In order to make these conversions, densities were chosen based on the assumption that γ and α were composed of pure Ni and Cr, respectively, and the intermetallics β and γ′ were pure, stoichiometric NiAl and Ni_3Al, respectively. This would also introduce error in the measurements; however, a more accurate method to determine actual densities was not devised on account of the reasonable agreement that was found (Figure 47).

In a similar study conducted by Toscano et al [58], it was shown that ThermoCalc very accurately predicted the phases present in NiCoCrAlYRe and CoNiCrAlY coatings, however phase fractions were not measured quantitatively.

5.4.1.3 Comparison of Measured and Calculated Phase Compositions

The composition of each phase at each temperature was determined using SEM/EDS. Ten point-count measurements were taken at randomly selected areas of each phase, and the measured compositions were averaged. These compositions are compared in Table 4 to the CALPHAD-predicted equilibrium compositions.

Table 4. Measured and CALPHAD-predicted NiCrAlY phase compositions

Phase	Temperature (°C)	Predicted wt% Ni	Measured wt% Ni	Predicted wt% Cr	Measured wt% Cr	Predicted wt% Al	Measured wt% Al
γ′	700	83.0	75.5 (2.1)	4.0	10.1 (2.7)	13.0	14.4(0.8)
β	700	72.0	-	6.0	-	22.0	-
α	700	0.3	-	99.7	-	0.0	-
γ′	900	81.0	78.6 (0.6)	7.0	6.7 (0.4)	12.0	14.7 (0.3)
β	900	72.5	69.8 (1.3)	8.5	9.0 (2.0)	19.0	21.2 (0.9)
α	900	1.8	14.3 (4.2)	98.2	82.1 (5.0)	0.0	3.6 (0.9)
γ	1100	62.0	61.9 (0.7)	31.5	31.2 (0.7)	6.5	6.9 (0.2)
β	1100	67.5	68.6 (0.6)	15.0	11.7 (0.4)	17.5	19.7 (0.4)
α	1100	6.8	9.5 (0.7)	92.9	89.4 (0.9)	0.3	1.1 (0.5)

At 900°C and 1100°C, agreement is seen to be generally quite good. Significant divergence is observed in the 900°C α composition due to the fact that the microstructure was too fine to make accurate EDS measurements. This problem was particularly pronounced for the α and β phases at 700°C, and so these data were not included in Table 4.

5.4.1.4 Dilatometer Studies

Dilatometry was conducted at Ames Laboaratory on a NETZSCH DIL 402 C dilatometer through to 1150°C. Any phase transformation which occurs is inevitably accompanied by a volume change, and this appears as a change in slope of the expansion (heating) or contraction (cooling) curve ($\Delta L/L_0$ vs. T) shown in Figure 48.

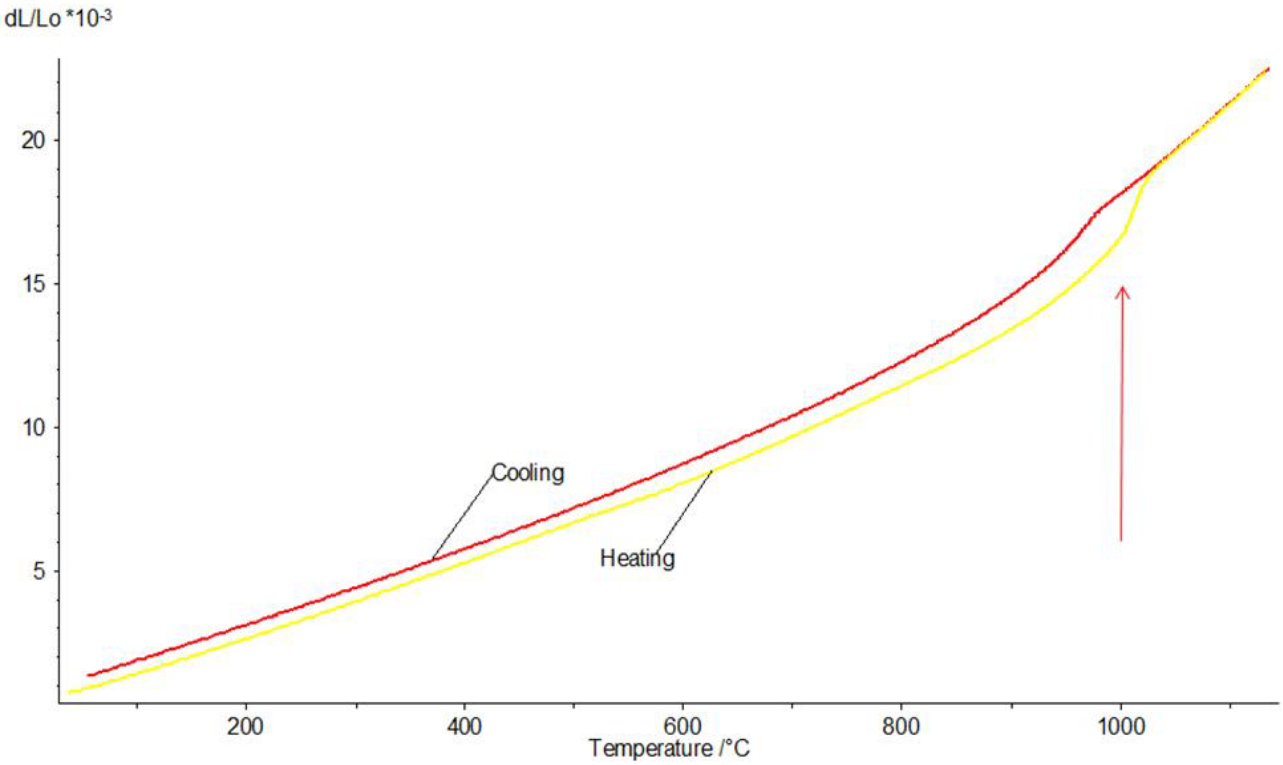

Figure 48. NiCrAlY expansion curve

A rapid increase in slope, indicated by the red arrow in Figure 48, occurs at approximately 1000°C upon heating with some hysteresis during cooling. This corresponds quite well with the four-phase class II quasi-peritectoid reaction [59]

$$\alpha + \gamma' \rightarrow \beta + \gamma \quad (44)$$

which was identified via CALPHAD in the current work to occur at 996°C, as well as in other laboratories at approximately 990 ± 3°C[60-61]. The exact bulk compositions over which this invariant reaction occurs are unknown; however the experimental and computational work presented above confirms that a Ni-31Cr-11.25Al alloy does indeed fall in this compositional range. Taylor and Walsh [62] performed dilatometry on a Ni-20Cr-11Al-0.5Y alloy and observed similar behavior, i.e. a phase transformation at around 950-1000°C upon heating and a reversal upon cooling with some hysteresis.

5.4.2 Consequences for Cyclic Oxidation Performance

The homogenized NiCrAlY alloy was exposed to cyclic oxidation conditions at 900°C and 1100°C for a total of 100 cycles, and at 1050°C for 180 cycles. The resulting plots of the weight change kinetics are presented in Figure 49:

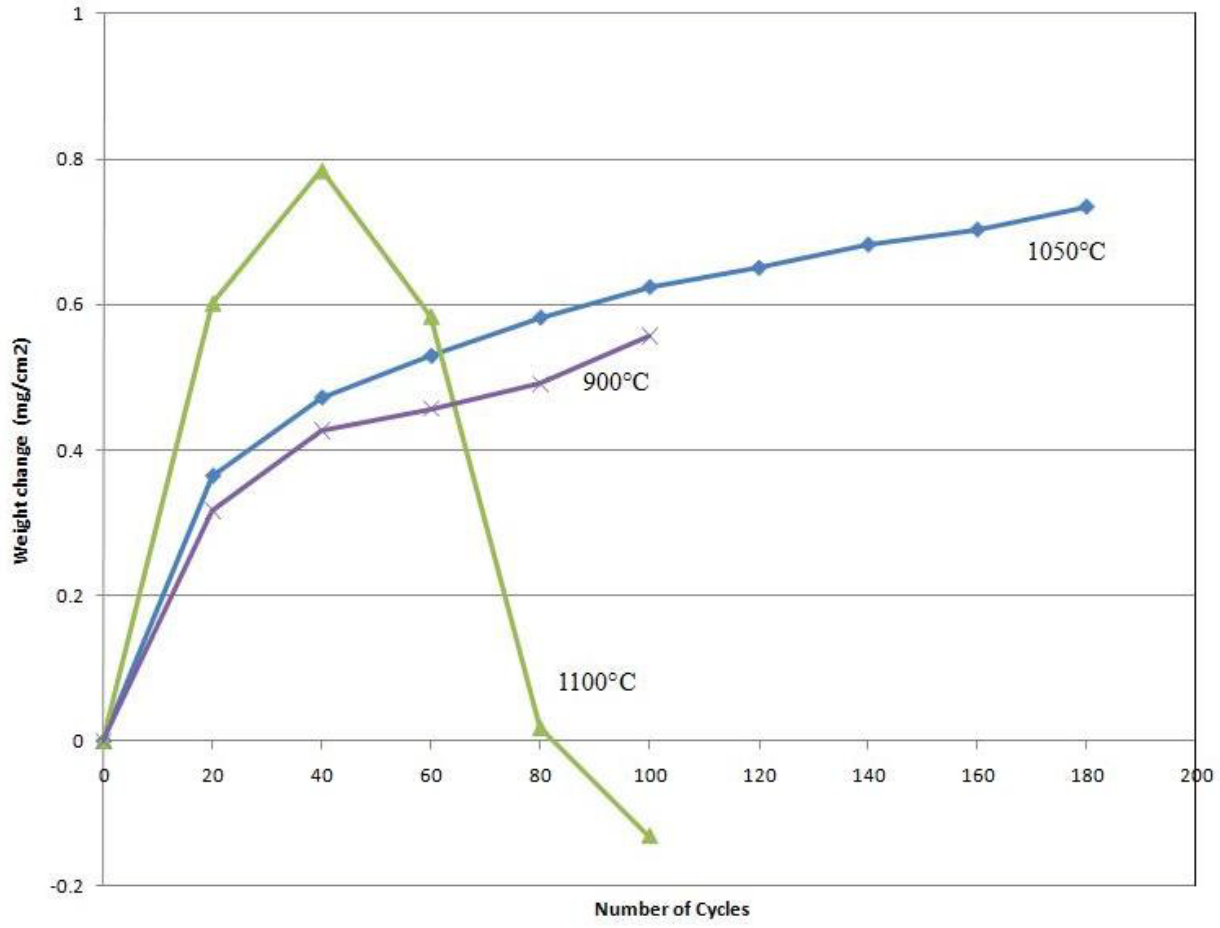

Figure 49. Weight change vs. time: NiCrAlY cyclic oxidation

At 900°C, the NiCrAlY oxidized at a roughly parabolic rate up to 100 cycles after a short period of relatively rapid transient oxidation. At 1100°C, oxidation occurs at a higher rate than at 900°C for a period of approximately 40 cycles, after which time spallation of the α-Al_2O_3 scale begins to occur, as indicated by the negative rate of weight change. At 1050°C, the specimen oxidized at an intermediate rate up to 180 cycles, forming an adherent scale with no observable spallation. Figure 50 shows cross-sectional SEM micrographs of the 900°C and 1100°C specimens after 100 cycles. The oxide scale has clearly spalled from the 1100°C specimen, and an extensive α/β-denuded zone is observed. At 900°C, however, a thin and adherent Al_2O_3 scale is found with minimal Al-depletion.

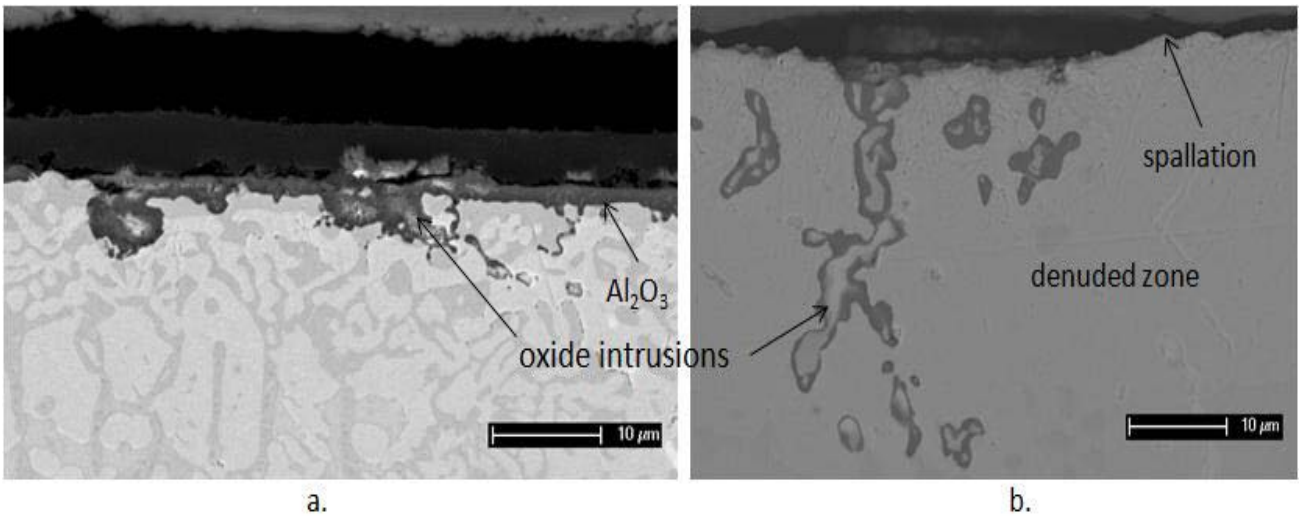

Figure 50. NiCrAlY cyclic oxidation microstructures: a.) 900°C, b.) 1100°C

Many factors are known to contribute to oxide scale spallation during high-temperature thermal cycling. Such factors include thermal mismatch stresses, i.e., stresses due to a thermal expansion mismatch between the oxide and substrate [63], oxide growth stresses, which increase with increasing oxide thickness [6], and segregation of impurities to the alloy/TGO interface [51]. In addition, the oxide intrusions formed in all of the alloys in the current study during

cyclic oxidation can lead to a decrease in oxidation resistance, particularly in the case of coated superalloys [46].

The effects identified above become more pronounced with increasing temperature, and so each help to explain the increased propensity for scale spallation during cycling to 1100°C relative to 900°C. As will be shown in the following, another factor contributing to the scale spallation at 1100°C is the occurrence of a phase transformation in the alloy during cooling from this higher temperature.

Figure 51 shows the calculated specific volume of the NiCrAlY alloy as a function of temperature. The specific volume was calculated using the following formula:

$$(\text{S.V.})_T = \sum_i (m_i/\rho_i)_T \quad (45)$$

for phases i of mass fraction m_i and density ρ_i, which are both functions of temperature. The mass fractions were taken from the CALPHAD work conducted in the current study, and the density values were calculated based on the work of Lowell et al. [64], who determined the lattice parameters of the common phases in MCrAlY coatings as a function of temperature using high-temperature XRD.

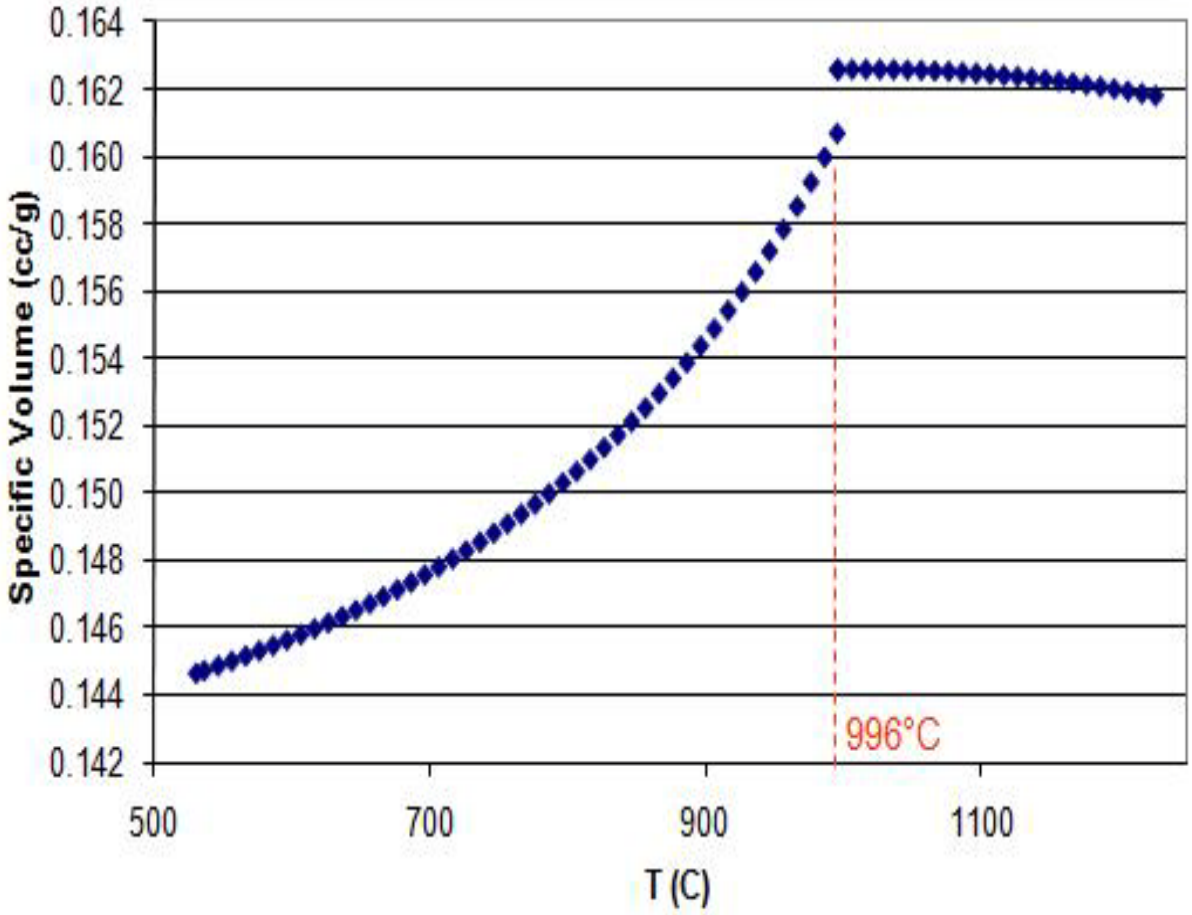

Figure 51. NiCrAlY specific volume as a function of temperature

As shown in Figure 51, an approximately 1% decrease in specific volume occurs upon cooling through 996°C, the calculated temperature of the four-phase equilibrium in this system (Eq. 44). The compressive stresses in the oxide scale generated from this repeated contraction during thermal cycling likely contributed to the spallation observed during 1100°C cyclic oxidation (Figure 49 and Figure 50). The alloy did not undergo this transformation when cycled to 900°C, and so there was a reduced inducement for scale spallation to occur during thermal cycling at this temperature. However, when cycled to 1050°C, which is above the observed phase transformation temperature, no spallation is observed after 180 cycles. Therefore, the observed oxidation behavior is the combined result of the following factors:

1. Thermal mismatch stresses in the oxide, which arise as a result of the difference in the coefficient of thermal expansion between the oxide and the substrate, are directly proportional to ΔT, the temperature range through which the specimen is cooled. Since all specimens are cooled down to approximately the same temperature during each thermal cycle, these stresses clearly increase as the exposure temperature increases.
2. Spallation occurs when the stored elastic strain energy in the oxide exceeds the fracture resistance of the oxide/alloy interface. This stored elastic energy increases linearly with oxide thickness. For a given exposure time, the oxide thickness, and therefore the stored elastic strain energy, increases with increasing exposure temperature.
3. Compressive stresses in the oxide develop during cooling through the above-mentioned phase transformation at ~996°C due to rapid volume contraction of the alloy.

It is interesting to note that the specific volume begins to decrease with increasing temperature above the transformation temperature (Figure 51). According to Figure 44, above 996°C, β begins to dissolve, resulting in an increase in the fraction of γ in the microstructure. β is primitive cubic (B2) and γ is face-centered cubic (A1). An increase in the amount of the close-packed γ phase (specific volume = 0.13 cm^3/g at 1097°C) at the expense of the more open-structured β (specific volume = 0.18 cm^3/g at 1097°C) is responsible for this decrease in specific volume.

5.5 THE EFFECT OF PHASE DISTRIBUTION ON THE TYPE II HOT CORROSION RESISTANCE OF NiCrAlY ALLOYS

Samples of the NiCrAlY alloy equilibrated at 700°C, 900°C, and 1100°C were exposed to Type II conditions for 10 hours in order to determine the effect of phase distribution on the resistance to this type of degradation. The equilibrated microstructures, prior to hot corrosion exposure, are presented in Figure 44. Injection casting was used in addition to heat treatment in order to alter the microstructure of this alloy. The IC NiCrAlY had the finest microstructure (Figure 13), the scale of which is more comparable to that observed in the case of actual MCrAlY coatings deposited on superalloys. In order to define the degree of coarseness of the heat-treated specimens, quantitative metallography was used to measure the relative amounts of phase boundary area. For each specimen, binary images such as the one found in Figure 46b. were further manipulated using the ImageJ software such that a single layer of pixels was placed at the interphase boundaries surrounding the α phase. An example of this binary image for the 1100°C specimen is presented in Figure 52. The area fractions of these phase-boundary pixels were then measured in order to obtain an "area fraction of α phase boundary", the values of which can be found in Table 5.

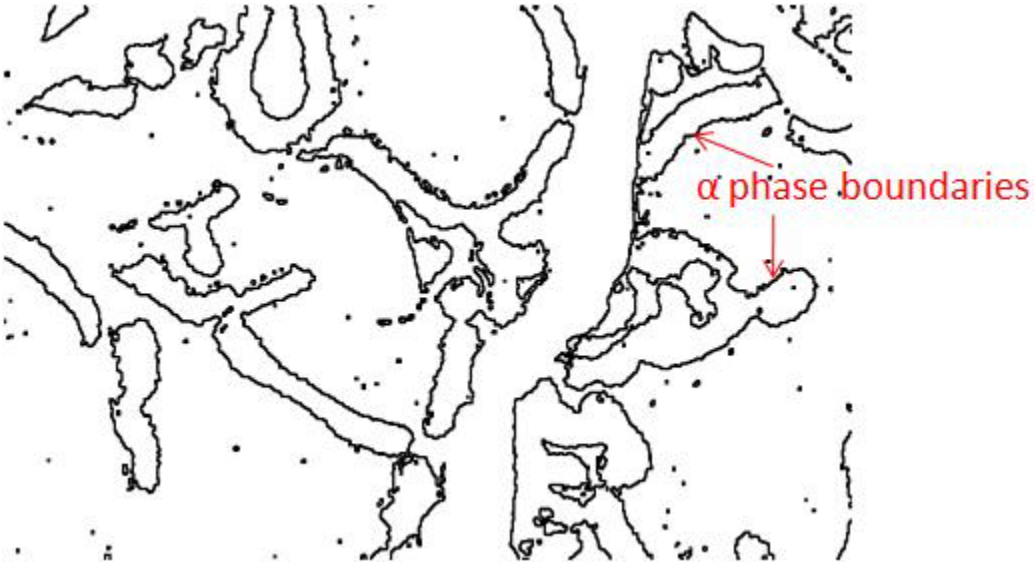

Figure 52. SEM image of the NiCrAlY equilibrated at 1100°C manipulated for phase boundary area calculation

Table 5. Area fraction of phase boundary surrounding the α phase: NiCrAlY

T (°C)	700	900	1100
Area fraction of α phase boundary	0.236	0.170	0.090

It is to be noted that, as the resolution of this "area fraction of α phase boundary" measurement technique can be no better than 1 pixel, these are only relative values, not actual grain boundary area fractions. The decrease in this relative value with increasing heat-treatment temperature indicates a coarsening of the microstructure with increasing temperature.

Microstructures of the specimens after 10 hours of Type II hot corrosion exposure are presented in Figure 53:

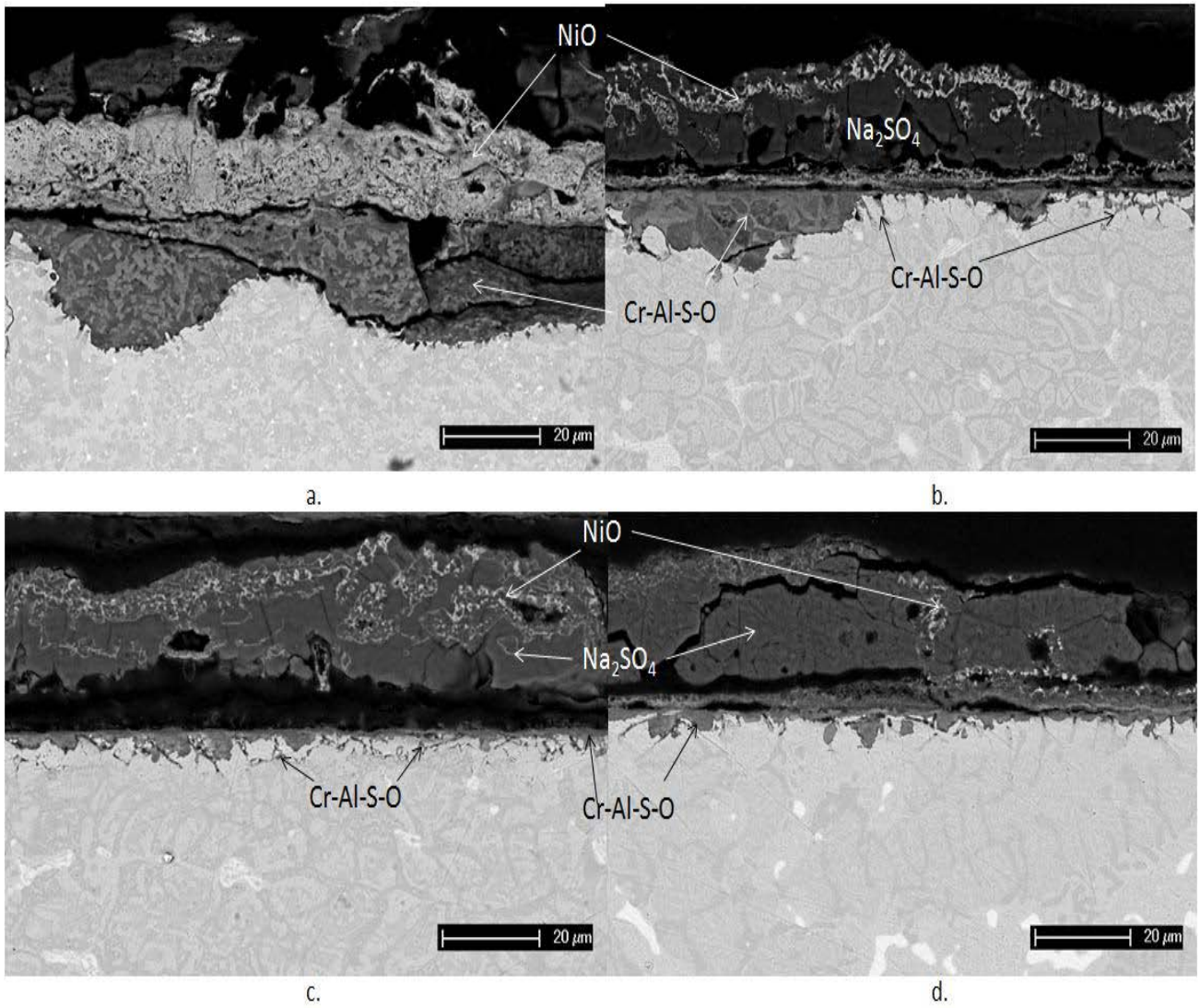

Figure 53. Type II hot corrosion microstructures: NiCrAlY a.) injection cast, and equilibrated at b.) 700°C, c.) 900°C, and d.) 1100°C

It is apparent in Figure 53 that the distribution of phases has a profound effect on Type II hot corrosion resistance. Specifically, degradation becomes more severe as the microstructure is refined. Based on microstructural observation, the degree of corrosion can be described in terms of the amount and density of NiO precipitated at the surface of the salt, the extent of internal attack along interphase boundaries, and the depth and frequency of the corrosion pits. Based on these three parameters, the hot corrosion attack becomes more severe as the microstructure is refined. This is particularly clear when one compares Figure 53 a. and d., i.e. the degradation of the NiCrAlY specimens with the finest and coarsest microstructures, respectively. In the case of the IC specimen, a thick NiO layer has precipitated out at the surface of the specimen, the corrosion pits are ~20μm deep and present over the entire cross section, and internal attack can be found just ahead of the corrosion front, nearly always initiating at interphase boundaries surrounding the α phase. By contrast, the specimen initially equilibrated at 1100°C shows nearly no evidence of Type II hot corrosion attack. Very small amounts of NiO are indeed observed near the surface of the salt, but they are far from coalescing into a continuous layer. There are some pit-like intrusions into the alloy, however they are quite shallow in comparison to those found in the IC specimen. Finally, some internal attack is observed along interphase boundaries, however this attack is quite scarce. Specimens equilibrated at 700°C and 900°C represent intermediate cases.

X-ray maps of the NiCrAlY specimens found in Figure 53 a. and d. are presented in Figure 54 and Figure 55, respectively.

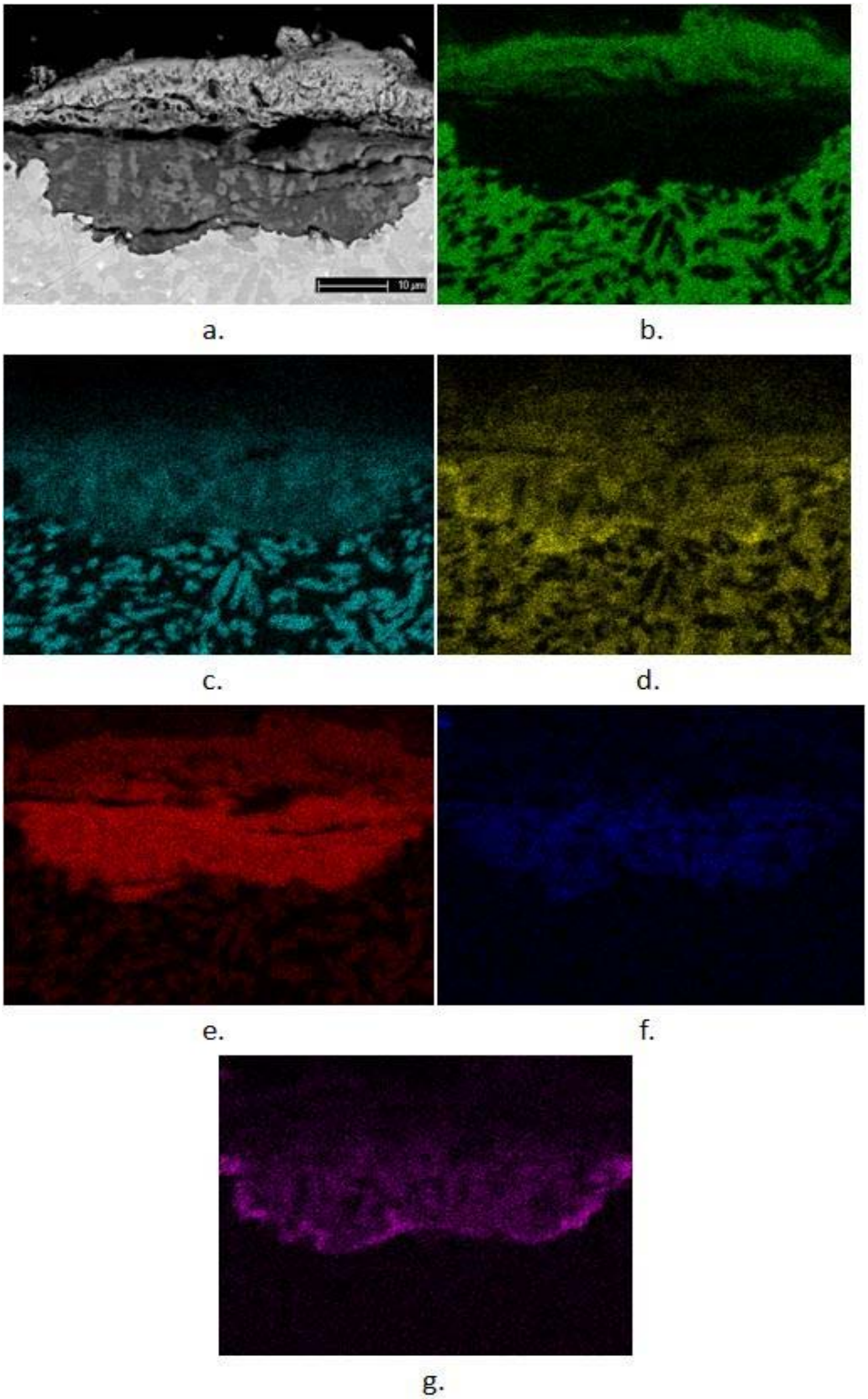

Figure 54. NiCrAlY IC Type II x-ray map: a.) BSEmicrograph, b.) Ni, c.) Cr, d.) Al, e.) O, f.) Na, g.) S

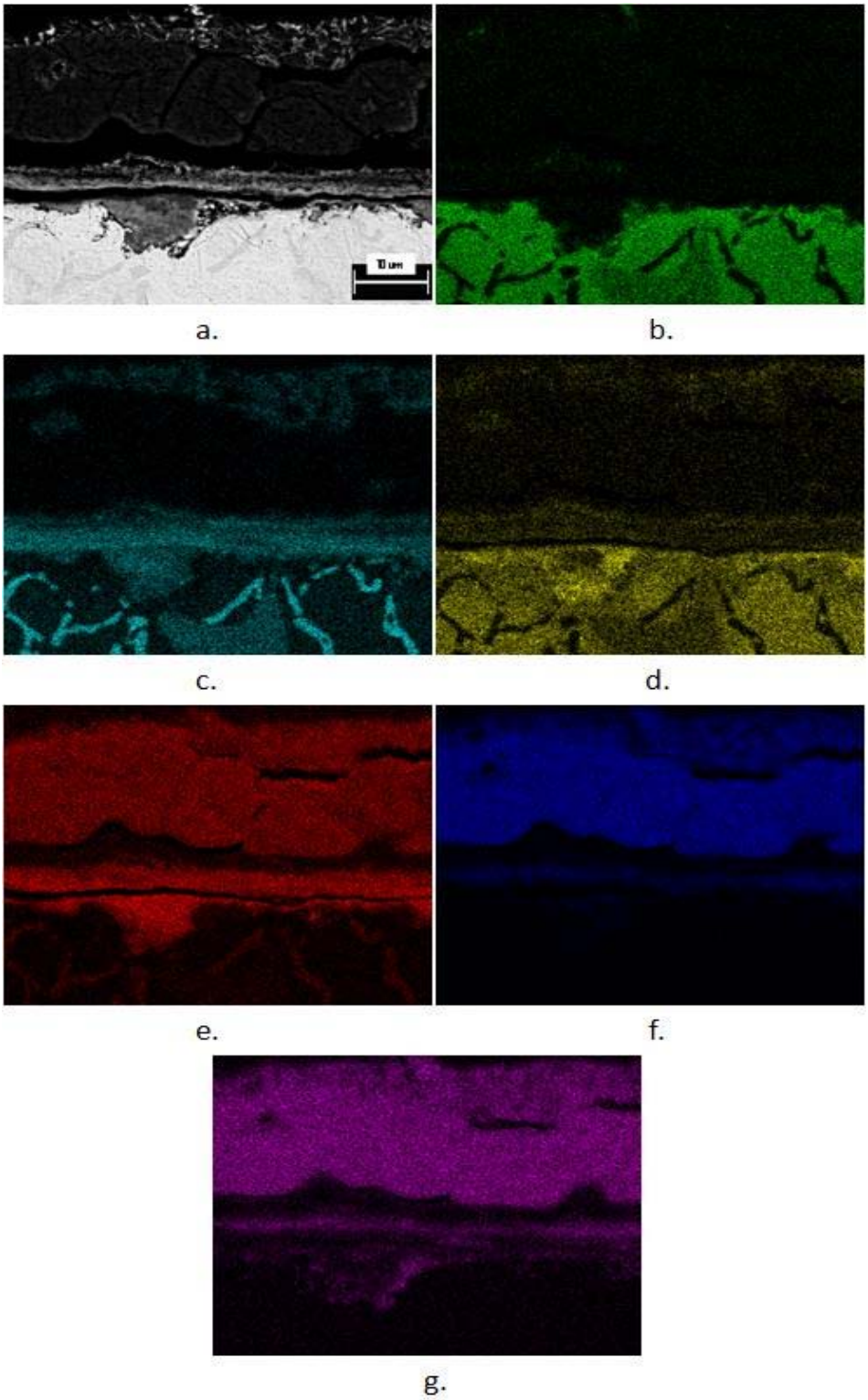

Figure 55. NiCrAlY 1100°C + Type II x-ray map: a.) BSEmicrograph, b.) Ni, c.) Cr, d.) Al, e.) O, f.) Na, g.) S

The alloy heat treated at 1100°C prior to Type II exposure has formed a continuous Cr-rich corrosion product which appears to have resulted in rather protective behavior. This is similar to what was observed in the NiCoCrAlY-3 alloy in section 5.3.2, however the effect here is much more pronounced. The microstructural feature that is shared by this heat treated NiCrAlY and the NiCoCrAlY-3 is a fairly course, nearly continuous network of α-Cr, which seems to aid in the formation of a Cr-rich scale.

However, injection casting of the NiCrAlY alloy results in a very fine microstructure containing discrete, discontinuous α-Cr (Figure 13). During Type II hot corrosion exposure, severe attack is observed with no continuous Cr-rich phase in the corrosion product (Figure 54). α-Cr, therefore, seems to be most beneficial when it is oriented such that the formation of a continuous scale is favorable, i.e. when it is fairly coarse. The fine α precipitates in the IC NiCrAlY alloy do not impart much protection from Type II hot corrosion.

In the field of high-temperature oxidation, it is commonly found that finer microstructures are beneficial in terms of oxidation resistance. The expression for the minimum solute concentration required for an alloy to form a continuous external scale rather than discontinuous internal oxide precipitates is given in Equation 46 [6]:

$$N_B^O > \left[\frac{\pi g^*}{2\upsilon} N_O^{(s)} \frac{D_O V_m}{D_B V_{ox}}\right]^{1/2} \quad (46)$$

where N_B^O is the bulk solute concentration in the alloy, g^* is the critical volume fraction of internal oxide for the coalescence into an external scale for a given alloy system, υ is a stoichiometric constant, $N_O^{(s)}$ is the oxygen solubility in the alloy, D_O is the oxygen diffusivity, V_m is the alloy molar volume, V_{ox} is the oxide molar volume, and D_B is the diffusivity of the solute. The solute of interest, species B in this case, is the element responsible for forming the protective oxide. The dominant effect of microstructural refinement in alloy oxidation is an increase in D_B.

In a polycrystalline material, the diffusivity can be expressed as:

$$D_B = D_B^l + \frac{\delta}{d} D_B^{GB} \quad (47)$$

where D_B^l is the commonly-measured lattice diffusivity, D_B^{GB} is the grain boundary diffusivity, and $\frac{\delta}{d}$ is the total grain boundary thickness per unit specimen thickness. By refining the grain size of a polycrystalline material, $\frac{\delta}{d}$ is increased, resulting in an increase in D_B. This reduces the critical N_B^O for external oxide formation, resulting in a more oxidation-resistant alloy.

However, in the case of Type II hot corrosion studied here, microstructural refinement also results in an increase in the amount of internal attack. Internal oxidation/sulfidation is detrimental to high temperature oxidation and corrosion resistance because it decreases N_B^O, the bulk concentration of the solute responsible for forming a protective oxide. If this concentration is decreased below the minimum concentration defined in Eq. 46, a protective oxide will not form and the material will be highly susceptible to rapid degradation. A micrograph showing the internal oxidation/sulfidation which occurred ahead of the corrosion front during the Type II hot corrosion of the IC NiCrAlY is presented in Figure 56:

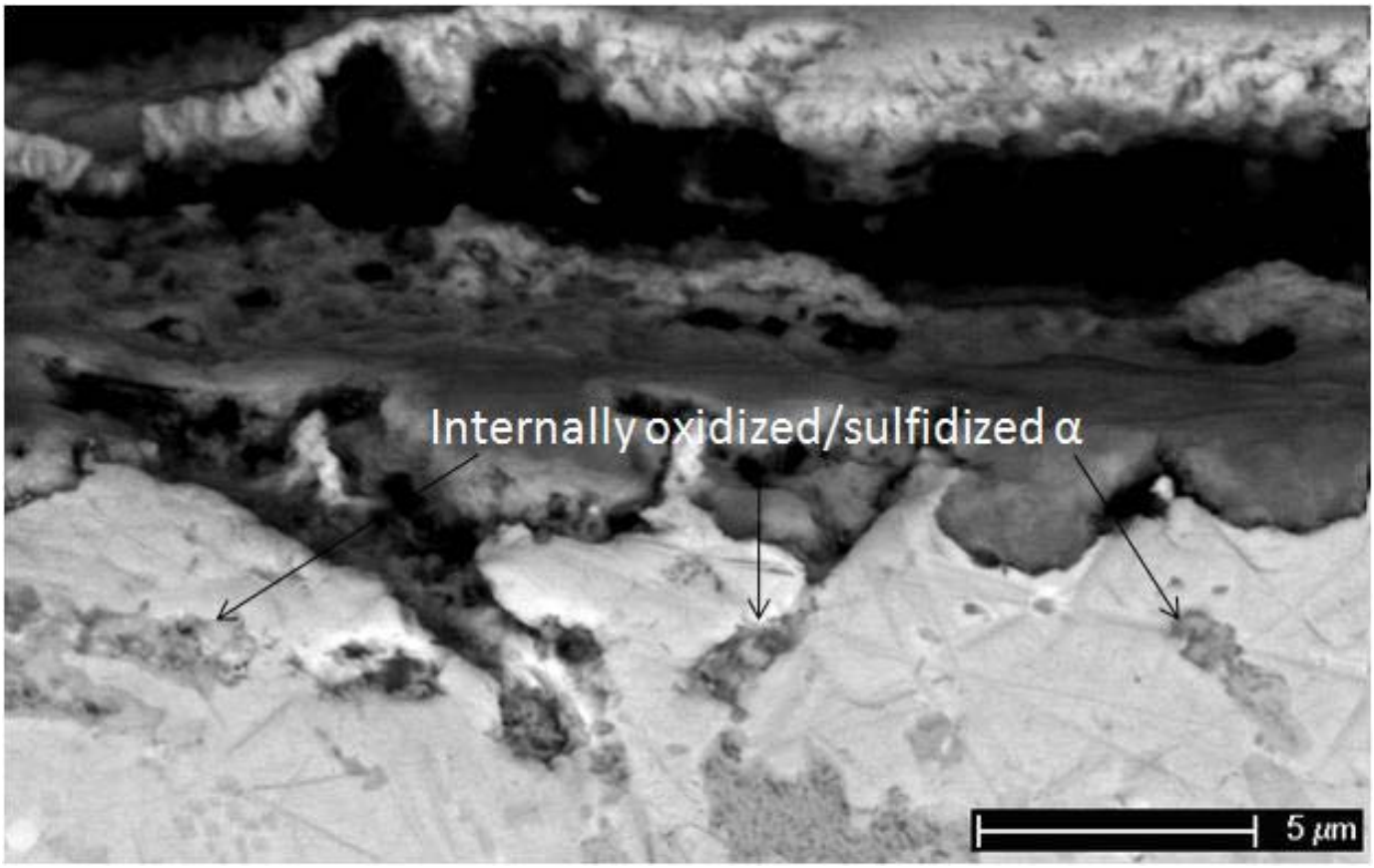

Figure 56. IC NiCrAlY Type II hot corrosion microstructure showing internal attack of α phase

This internal attack lowers the value of N_{Cr}^{O}, making the alloy more susceptible to corrosive damage, as observed in Figure 53. Internal oxidation and sulfidation does indeed occur during the Type II hot corrosion of all α-Cr-containing alloys in this study, however when the microstructure is relatively fine, internal oxidation is more prevalent and a protective Cr-rich scale fails to form.

6.0 CONCLUSIONS

Cast alloys of compositions Ni-31Cr-11.25Al-0.65Y, Co-23Cr-13Al-0.65Y, Ni-20Co-18Cr-12.5Al-0.6Y-0.4Hf-0.25Si, Ni-10Co-18Cr-12.5Al-0.6Y-0.4Hf-0.25Si, and Ni-10Co-27.1Cr-12.5Al-0.6Y-0.4Hf-0.25Si were tested under Type I hot corrosion, Type II hot corrosion, cyclic oxidation, and intermittent Type I hot corrosion conditions. An uncoated superalloy, René N5, was also tested under cyclic oxidation and intermittent Type I conditions for comparison. The effects of alloy composition and microstructure on the resistance to degradation in these aggressive environments were determined.

All MCrAlY alloys demonstrated good resistance to Type I hot corrosion. The NiCrAlY alloy lost weight throughout the exposure, but this was attributed to the dissolution and subsequent washing away of Na_2CrO_4. No evidence of Type I degradation (i.e., internal sulfidation) was observed in the microstructure.

Type II hot corrosion degradation was severe in most cases. The NiCrAlY alloy was relatively resistant to this type of attack; however, it was found that this resistance depended largely on the alloy microstructure. Heat treating the NiCrAlY at 1100°C prior to Type II exposure resulted in a coarse-grained microstructure and good corrosion resistance. Heat treating at lower temperatures resulted in finer microstructures, and the Type II corrosion resistance decreased. An extremely fine microstructure was achieved by injection casting small-diameter rods of the same alloy composition, and this resulted in a large decrease in corrosion resistance. This inverse relationship between the degree of microstructural refinement and Type II hot corrosion resistance is attributed largely to the increased propensity for internal oxidation/sulfidation in the fine-grained specimens. Specifically, the internal attack occurred mostly along interphase boundaries surrounding the α phase, the areal density of which increased as the microstructure became finer. Internal oxidation/sulfidation depletes the neighboring material of protective scale-forming elements, resulting in an increased susceptibility to

corrosive attack. When the microstructure is coarse, many α-Cr grains are oriented such that preferential oxidation/ sulfidation of this phase allows for a fairly protective Cr-rich layer to form at the base of the corrosion product.

Reducing the Co content of the NiCoCrAlY alloy did not result in an increase in Type II hot corrosion resistance unless the Cr content was increased beyond the solubility limit in γ-Ni. In the case of the NiCoCrAlY-3, the Cr content was high enough to precipitate a nearly continuous network of α-Cr, which had an effect similar to that discussed above for the coarse-grained NiCrAlY.

All alloys, except for the NiCrAlY, formed thin and adherent Al_2O_3-rich scales during cyclic oxidation at 1100°C. The NiCrAlY, however, showed scale spallation after around 40 cycles at 1100°C. Spallation was not observed for up to 100 cycles at 900°C and 180 cycles at 1050°C. This behavior can be explained in terms of increased thermal mismatch stress and oxide thickness (resulting in an increase in stored elastic strain energy) with increasing thermal cycling temperature. In addition, volume contraction of the alloy upon cooling due to a phase transformation at 996°C results in a compressive stress in the oxide, which also contributes to spallation at 1100°C. A thorough examination of the phase equilibria in the NiCrAlY system, using data from both experiments and thermodynamic predictions, aided in the interpretation of these results.

Finally, a 20 hour Type I hot corrosion pre-treatment did not seem to have any significant effect on the 1100°C cyclic oxidation behavior of the MCrAlY alloys. By contrast, René N5, a marginal Al_2O_3-forming superalloy, degraded catastrophically during cyclic oxidation after 20 hours of Type I hot corrosion. This is likely due to the combined effects of Al and Cr depletion and a decrease in scale adhesion due to the injection of sulfur during the Type I exposure.

When discussing the effect of microstructure on the Type II hot corrosion behavior of the NiCrAlY alloy, it is acknowledged that other factors may be of importance. For example, the relative amounts of the phases present when the alloy was heat treated at 700°C, 900°C, and 1100°C were not correlated with the corrosion resistance. However, even this may not be sufficient, since the composition of each phase varies as a function of heat treatment temperature. The effect of the relative amounts of phases on the hot corrosion resistance of NiCrAlY alloys will be addressed in future work.

BIBLIOGRAPHY

1. Bornstein N.S., A., W.P., *The Chemistry of Sulfidation Corrosion-Revisited.* Mater. Sci. Forum, 1997. **127**: p. 127-134.

2. McCreath, C.G., *Hot Corrosion Site Environment in Gas Turbines.* Mater. Sci. and Technol., 1987. **3**: p. 494-500.

3. DeCrescente, M.A., Bornstein, N.S., *Formation and Reactivity Thermodynamics of Sodium Sulfate with Gas Turbine Alloys.* Corrosion, 1968. **24**: p. 127-133.

4. Hanby, H.I., Beer, J.M., *Salt Deposition and Corrosion in Marine Gas Turbines*. 1969-1972.

5. Janz, G.J., *Molten Salts Handbook*. 1967, New York: Academic Press.

6. Birks, N., Meier, G.H., Pettit, F.S., *Introduction to the High Temperature Oxidation of Metals*. 2 ed. 2006, New York: Cambridge University Press.

7. Giggins, C.S., Pettit, F.S. , *Hot Corrosion Degradation of Metals and Alloys - A Unified Theory*. 1979.

8. Deodeshmukh, V., Gleeson, B. *Environmental and Compositional Effects on the Hot-Corrosion Behavior of Ni-Based Alloys and Coatings*. in *Corrosion 2008*. New Orleans, LA: NACE International.

9. Inman, D., Wrench, D.M., *Corrosion in Fused Salts.* Brit. Corr. J., 1966. **1**: p. 246-250.

10. Rapp, R.A., *Chemistry and Electrochemistry of the Hot Corrosion of Metals.* Corrosion, 1986. **42**: p. 568-577.

11. Gupta, D.K., Rapp, R.A., *The Solubilities of NiO, Co_3O_4, and Ternary Oxides in Fused Na_2SO_4 at 1200°K.* J. Electrochem. Soc., 1980. **127**: p. 2194-2202.

12. Jose, P.D., Gupta, D.K., Rapp, R.A., *The Solubility of α-Al_2O_3 in Fused Na_2SO_4 at 1200°K.* J. Electrochem. Soc., 1985. **132**: p. 735-737.

13. Shi, D.Z., Rapp, R.A. , *The Solubility of SiO_2 in Fused Na_2SO_4 at 900°C.* J. Electrochem. Soc., 1986. **133**: p. 849-580.

14. Deanhardt, M.L., Stern, K.H., *Solubility Products of Metal Oxides in Molten Salts by Coulometric Titration of Oxide Ion Through Zirconia Electrodes.* J. Electrochem. Soc., 1982. **128**: p. 2577-2582.

15. Zhang, Z.S., *Solubilities of Cr_2O_3 in Fused Na_2SO_4 at 1200K.* J. Electrochem. Soc., 1986. **133**: p. 655-657.

16. Zhang, Z.S., Rapp R.A., *Solubility of α-Fe_2O_3 in Fused Na_2SO_4 at 1200K.* J. Electrochem. Soc., 1985. **132**: p. 734-735.

17. Rapp, R.A., Goto, K.S. *The Hot Corrosion of Metals by Molten Salts*. in *The Second International Symposium on Molten Salts*. 1981.

18. Simons, E.L., Browning G.V., Liebhefsky, H.A., *Sodium Sulfate in Gas Turbines.* Corrosion, 1956. **11**: p. 63-64.

19. Quets, J.M., Dresher, W.H., *Thermochemistry of the Hot Corrosion of Superalloys.* J. Mater., 1969. **4**: p. 583-599.

20. Danek, G.J., *State-of-the-Art Survey on Hot Corrosion in Marine Gas Turbines.* Naval Engineers Journal, 1965. **77**: p. 859-869.

21. Seybolt, A.U., *Contribution to the Study of Hot Corrosion.* Trans. TMS AIME, 1968. **242**: p. 1955-1961.

22. Bornstein N.S., D., M.A., *The Relationship Between Compounds of Sodium and Sulfur and Sulfidation.* Trans. TMS AIME, 1969. **245**: p. 1947-1952.

23. Goebel, J.A., Pettit, F.S., *Na_2SO_4- Induced Accelerated Oxidation (Hot Corrosion) of Nickel.* Met. Trans., 1970. **1**: p. 1943-1954.

24. Rapp, R.A., *Hot Corrosion of Materials: A Fluxing Mechanism?* Corrosion Sci., 2002. **44**: p. 209-221.

25. Shores, D.A., Fang, W.C., *Transport of Oxidant in Molten Na_2SO_4 in O_2-SO_2-SO_3 Environments.* J. Electrochem. Soc., 1981: p. 346.

26. Fang, W.C., Rapp, R.A., *Electrochemical Reactions in a Pure Na_2SO_4 Melt.* J. Electrochem. Soc., 1983. **130**: p. 2335.

27. Zheng, X., Rapp, R.A., *Electrochemical Impedance of a Platinum Electrode in Fused Na_2SO_4 melts in SO_2-O_2 Environments.* J. Electrochem. Soc., 1993. **140**: p. 2857-2862.

28. Pettit, F.S., Goebel, J.A., Goward, G.W., *Thermodynamic Analysis of Simultaneous Attack of Some Metals and Alloys by Two Oxidants.* Corrosion Sci., 1969. **9**: p. 903-913.

29. Goebel, J.A., Pettit, F.S., *The Influence of Sulfides on the Oxidation Behavior of Nickel-Base Alloys.* Met. Trans., 1970. **1**: p. 3421-3429.

30. Bornstein N.S., D., M.A., *The Role of Sodium in the Accelerated Oxidation Phenomenon Termed Sulfidation.* Met. Trans., 1971. **2**: p. 2875-2883.

31. Goebel, J.A., Pettit, F.S., Goward, G.W., *Mechanisms for the Hot Corrosion of Nickel-Base Alloys.* Met. Trans., 1973. **4**: p. 261-278.

32. Meier, G.H., *A Review of Advances in High-Temperature Corrosion.* Mater. Sci. Eng., 1989. **A120**: p. 1-11.

33. Ross, E.W., Sims, C.T., ed. *Nickel-Base Alloys*. Superalloys II, ed. C.T. Sims, Stoloff, N.S., Hagel, W.C. 1987, John Wiley & Sons: New York.

34. Bornstein, N.S., DeCrescente, M.A., Roth, H.A. *Accelerated Corrosion in Gas Turbine Engines*. in *Gas Turbine Materials Conference*. 1972. Washington, D.C.

35. Conde, J.F.G., Wareham, G.C. *Aspects of the Mechanisms of Hot Corrosion in Marine Gas Turbines*. in *The 2nd Conference on Gas Turbine Materials in a Marine Environment*. 1974.

36. Wortman, D.J., Fryxell, R.E., Luthra, K.L., Bergman, P.A., *Mechanism of Low-Temperature Hot Corrosion: Burner Rig Studies.* Thin Solid Films, 1979. **64**: p. 281-288.

37. Luthra, K.L., Shores, D.A., *Mechanism of Na_2SO_4 Induced Corrosion at 600°-900°C.* J. Electrochem. Soc., 1980. **127**: p. 2202-2210.

38. Wortman, D.J., Fryxell, R.E., Bessen, I.I. *A Theory for Accelerated Turbine Corrosion at Intermediate Temperatures*. in *The 3rd Conference on Gas Turbine Materials in a Marine Environment*. 1976.

39. Luthra, K.L., *Low Temperature Hot Corrosion of Cobalt-Base Alloys: Part1. Morphology of the Reaction Product.* Met. Trans. A, 1982. **13A**: p. 1843-1852.

40. Barkalow, R.H., Goward, G.W., *Microstructural Features of Low Temperature Hot Corrosion in Nickel and Cobalt Base MCrAlY Coatings Alloys*, in *High Temperature Corrosion*, R.A. Rapp, Editor. 1983, National Society of Corrosion Engineers: Houston. p. 502-506.

41. Chiang, K.T., Pettit, F.S., Meier, G.H., *Low Temperature Hot Corrosion*, in *High Temperature Corrosion*, R.A. Rapp, Editor. 1983, National Society of Corrosion Engineers: Houston. p. 519-530.

42. Jones, R.L., *Cobalt Oxide-SO_2/SO_3 Reactions in Cobalt-Sodium Mixed Sulfate Formation and Low Temperature Hot Corrosion,* in *High Temperature Corrosion,* R.A. Rapp, Editor. 1983, National Society of Corrosion Engineers: Houston. p. 513-518.

43. Luthra, K.L., Shores, D.A. *Morphology of Na_2SO_4 Induced Hot Corrosion at 600-750°C.* in *The 4th Conference on Gas Turbine Materials in a Marine Environment*. 1979.

44. Luthra, K.L., *Low Temperature Hot Corrosion of Cobalt-Base Alloys: Part 2. Reaction Mechanism.* Met. Trans. A, 1982. **13A**: p. 1853-1864.

45. Deodeshmukh, V., Mu, N., Gleeson, B., *Hot Corrosion and Oxidation Behavior of a Novel Pt + Hf-Modified γ'-Ni3Al + γ-Ni Based Coating.* Surf. Coat. and Tech., 2006. **201**: p. 3836-3840.

46. Meier-Jackson, E.M., Yanar, N.M., Maris-Jakubowski, M.C., Onal-Hance, K., Meier, G.H., Pettit, F.S., *Effect of Surface Preparation on the Durability of NiCoCrAlY Coatings for Oxidation Protection and Bond Coats for Thermal Barrier Coatings.* Materials and Corrosion, 2008. **59**: p. 494-500.

47. Munoz-Arroyo, R., Clemens, D., Tietz, F., Anton, R., Quadakkers, W. J., Singheiser, L., *Influence of Composition and Phase Distribution on the Oxidation Behaviour of NiCoCrAlY Alloys.* Materials Science Forum, 2001. **369-372**: p. 165-172.

48. Nijdam, T.J., Kwakernaak, C., Sloof, W. G., *The Effects of Alloy Microstructure Refinement on the Short-Term Thermal Oxidation of NiCoCrAlY Alloys.* Met. and Mater. Trans. A, 2006. **37A**: p. 683-693.

49. Li, M.H., Sun, X.F., Jin, T., Guan, H.R., Hu, Z.Q., *Oxidation Behavior of a Single-Crystal Ni-base Superalloy in Air-II: At 1000, 1100, and 1150°C* Oxid. Metals, 2003. **60**: p. 195-210.

50. Nychka, J.A., Clarke, D. R., Meier, G. H., *Spallation and Transient Oxide Growth on PWA 1484 Superalloy.* Materials Science and Engineering A, 2008. **490**: p. 359-368.

51. Hou, P.Y., *Segregation Behavior at TGO/Bondcoat Interfaces.* J. Mater. Sci., 2009. **44**: p. 1711-1725.

52. Jung, K., Pettit, F.S., Meier, G.H., *The Effect of Ca-rich Deposits on the High Tempearture Degradation of Coated and Uncoated Superalloys.* Materials Science Forum, 2008. **595-598**: p. 805-812.

53. Rapp, R.A., *Kinetics, Microstructures and Mechanism of Internal Oxidation- Its Effect and Prevention in High Temperature Alloy Oxidation.* Corrosion, 1965. **21**: p. 382-401.

54. Park, J.W., Altstetter, C.J., *The Diffusion and Solubility of Oxygen in Solid Nickel.* Met. Trans. A, 1987. **18A**: p. 43-50.

55. Mrowec, S., Grzesik, Z., *Oxidation of Nickel and Transport Properties of Nickel Oxide.* J. Phys. and Chem. of Solids, 2004. **65**: p. 1651-1657.

56. Dupin, N., Ansara, I., Sundman, B., *Thermodynamic Re-Assessment of the Ternary System Al-Cr-Ni.* Calphad-Comput. Coupling Ph. Diagrams Thermochem. , 2001. **25**: p. 279-298.

57. Underwood, E.E., *ASM Handbook.* Vol. 9. 1985.

58. Toscano, J., Gil, A., Hüttel, T., Wessel, E., Naumenko, D., Singheiser, L., Quadakkers, W.J., *Temperature Dependence of Phase Relationships in Different Types of MCrAlY-Coatings.* Surf. Coat. Technol., 2007. **202**: p. 603-607.

59. Rhines, F.N., *Phase Diagrams in Metallurgy: Their Development and Application*. 1956, New York: McGraw-Hill Book Company.

60. Merchant, S.M., Notis, M.R., *A Review: Constitution of the Al-Cr-Ni System.* Mater. Sci. Engr., 1984. **66**: p. 47-60.

61. Tu, D.C. 1982, State University of New York at Stony Brook.

62. Taylor, T.A., Walsh, P.N., *Thermal Expansion of MCrAlY Alloys.* Surf. Coat. Technol., 2004. **177-178**: p. 24-31.

63. Birks, N., Meier, G.H., Pettit, F.S., *Forming Continuous Alumina Scales to Protect Superalloys.* JOM, 1994. **46**: p. 42-46.

64. Lowell, C.E., Garlick, R.G., Henry, B., *Thermal Expansion in the Ni-Cr-Al and Co-Cr-Al Systems to 1200°C Determined by High-Temperature X-Ray Diffraction.* Met. Trans. A, 1976. **7A**: p. 655-660.